Title
Synthesis, Structure, and Optoelectronic Properties of Hybrid Metal Iodides

Permalink
https://escholarship.org/uc/item/4s79b8w4

Author
Evans, Hayden Aled

Publication Date
2018

Peer reviewed|Thesis/dissertation

UNIVERSITY of CALIFORNIA
Santa Barbara

Synthesis, Structure, and Optoelectronic Properties of Hybrid Metal Iodides

A Dissertation submitted in partial satisfaction of the
requirements for the degree
Doctor of Philosophy
in
Chemistry

by

Hayden Aled Evans

Committee in charge:

- Professor Ram Seshadri, Chair
- Professor Michael L. Chabinyc
- Professor Craig J. Hawker
- Professor Fred Wudl

December 2018

The dissertation of Hayden Aled Evans is approved.

Professor Michael L. Chabinyc

Professor Craig J. Hawker

Professor Fred Wudl

Professor Ram Seshadri, Committee Chair

December 2018

Synthesis, Structure, and Optoelectronic Properties of Hybrid Metal Iodides

by

Hayden Aled Evans

To my family, friends, and teachers

Acknowledgments

I will first thank my primary advisor, Ram. Without his limitless generosity and support these past five years, I would not have come as far as I have. He gave me the space to grow and develop my scientific intuition on my own terms, but when I needed him most, he was there. There are many things I could list that Ram has done, or taught me, but I will summarize by saying that Ram did everything in his power to facilitate my success. Thank you for accepting me into your group, nurturing me, and molding me into a scientist that I am proud to be.

I would next like to thank my co-advisor, and bonafide chemical muse, Fred. Fred provided the heart of my education; the synthesis. Outside of his unrivaled synthetic insight, Fred constantly tried to guide me about how to take my synthetic work to the next level, and instilled in me that everything is worth trying — as sometimes the unexpected is more exciting than what is planned. On a personal note, Fred shared his love of food, art, and woodworking with me, which let us foster a friendship outside of science. Thank you Fred, for working me at the tail end of your academic career, even when my Freshman chemistry escaped me.

To the other members of my committee, I am also incredibly grateful. I am thankful to Professor Michael Chabinyc for his advice of how to make my work more impactful, and his willingness to take the time to explain why an experiment was worth doing. Consistently, Michael knew exactly what was needed to answer any of my materials science questions, and for that I am incredibly appreciative. I would also like to thank Professor Craig Hawker for teaching me how to think deeply about what makes a good presentation, as learning how to do this effectively is essential for any scientist. I also thank him for being a bottom-less well of holiday cheer during the the MRL Holiday parties.

I would like to thank Professor Tony Cheetham, an unofficial advisor who I have had the privilege of working with during the last year of my PhD. Tony constantly demonstrated the power of positive thinking, and how certain problems deserve long meetings to wrangle with the details of them. I thank him for taking the time to work with me, and his generosity whilst hosting me in Singapore. Those experiences, in addition to all of our conversations, have been some of my favorites in graduate school.

Professor Tina Salguero gave me the opportunity to return to the University of Georgia to do research in her lab after I finished my undergraduate degree, which proved to be one of the most important periods of my life. There were many directions I could of chosen to go during that time, but Tina was willing to give me the opportunity to do science, and guided me through my transition into graduate school. Tina also read all of my application essays, which I can assure people was a tough gig. Most importantly though, Tina set the foundation of how to be a good scientist. I know that without her support (both in and outside the lab) I would not have made it to/at UCSB. I try to emulate her positive and nurturing attitude, because I know it had such a big impact on my life. I am forever grateful to her.

I would like to say a big thank you to Guang Wu, the Chemistry Department's staff crystallographer. Guang, except for a couple others at UCSB, is the one person I have talked to the most over the past five years. Guang spent countless hours hovering over my work and taught me many things that could go awry in a crystal structure refinement. He taught me so much about crystallography, but also science in general, especially the importance of being skeptical of ones own work. I now believe that, as he says, I can see "when something has some truth to it." Lastly, I know that Guang and I formed a lifelong friendship with our countless discussions about our differing politics. We always did it in the most respectful way possible, which in these polarizing times, was a breath of fresh air. Thank you Guang, for your help, and your friendship.

Day to day life in the MRL was truly amazing, and made possible by the phenomenal MRL staff. I thank them for their help over the years, especially Amanda Strom, for her indispensable guidance in the lab, and friendship outside of it. The cast of MRL people to thank includes, but is not limited to, Jaya Nolt, Shaman Walker, Jerry Hu, Youli Li, Fuzzy Rogers, Rachel Behrens, Sylvia Vogel, and Mary McGuan. I would also like to thank Dotti Pak for allowing me to assist with outreach and the CISEI program these past 3 years. It was always rewarding to work with burgeoning scientists from around the world, as well as a chance to work with her; a person who has such a big heart and is always going out of her way for others.

The Seshadri Group, past and present, has been a constant source of support. I count myself very lucky to be a part of this scientific family. I would particularly like to than Dr. Anna Lehner, for her help during the start of graduate school, Prof. Geneva Laurita for supporting me throughout, and Dr. Douglas Fabini, for his help with many of my projects. I would like to thank Clayton Cozzan (and Bretton Fletcher though hes not in the Seshadri group) for being hilarious office mates, and for being people who appreciated the finer things in life like good coffee. I would also like to say a special thank you to a past Seshadri group member, Professor Brent Melot, for his commitment to facilitating engaged social gatherings of our scientific family at conferences.

I would like to thank my everyday support system at UCSB that made being here such a pleasure. This includes my housemate of the past five years, Austin Barnes, who has made living in Santa Barbara so easy. I will miss him and our conversations at the bookends of our days. I would like to make a special thank you to the many lifelong friends I made performing improv at UCSB. For three years, they provided me with so many chances to laugh and be (deservedly) heckled when I probably should of been working. Graduate school can be tough, but knowing that I had people in my life who just wanted to tell jokes, and be happy, made it all manageable.

I will end by thanking the most important people in my life — my parents. They raised me to be a decent and honest person (even if I do talk a lot of trash) and I think my success is rooted in that. Though they never pushed me to do science, they taught me that if something in life was worth having that it was worth pursuing with gusto. I like to think that their support of my life choices means they know I'm trying to do just that. So, Rose and Malcolm, thank you.

Curriculum Vitae

Hayden Aled Evans

Education

Oct. 2014–Dec. 2018 PhD Candidate, Department of Chemistry and Biochemistry, University of California, Santa Barbara

Advisor: Professor Ram Seshadri and Fred Wudl

Aug. 2008–May 2012 B.S. Chemistry, University of Georgia

Graduation: Cum Laude, May 2012

Publications

14. Evans, H. A.; Andrews, J. L.; Fabini, D. H.; Preefer, M. B.; Wu, G.; Wudl, F.; Cheetham, A. K.; Seshadri, R. The capricious nature of iodine catenation in I_2 excess, perovskite-derived hybrid Pt(IV) compounds, *Chem. Commun.* **2018**, (*invited article*)

13. Evans, H. A.; Fabini, D. H.; Andrews, J. L.; Koerner, M.; Preefer, M. B.; Wu, G.; Wudl, F.; Cheetham, A. K.; Seshadri, R. Hydrogen bonding controls structural evolution in perovskite-related hybrid platinum (IV) iodides, *Inorg. Chem.* **2018**, *57*, 10375–10382

12. Brook, G.; Franco, N.; Cherkinsky, A.; Acevedo, A.; Fiore, D.; Pope, T.;

Weimar, R.; Neher, G.; Evans, H. A.; Salguero, T. Pigments, binders, and ages of rock art at Viuda Quenzana, Santa Cruz, Patagonia (Argentina), *J. Archaeol. Sci. Rep.* **2018**, *21*, 47–63.

11. Lewi T.; Evans, H. A.; Butakov, N. A.; Schuller, J. A. Thermo-optically reconfigurable PbTe mie resonator meta-atoms, *Nano Lett.* **2017**, *17*, 3940–3945.

10. Labram, J.*; Venkatesan, N.*; Takacs, C.; Evans, H. A.; Perry, E.; Wudl, F.; Chabinyc, M. Charge transport in a two-dimensional hybrid metal halide thiocyanate compound, *J. Phys. Chem. Lett.* **2017**, *5*, 5930–5938. (**equal contribution*) (*equal contribution)

9. Evans, H. A.; Schueller, E. C.; Smock, S. R.; Wu, G.; Seshadri, R.; Wudl, F. Perovskite-related hybrid noble metal iodides: Formamidinium platinum iodide $[(FA)_2Pt^{IV}I_6]$ and mixed-valence methylammonium gold iodide $[(MA)_2Au^{I}Au^{III}I_6$, *Inorg. Chim. Acta.*, **2017**, *468*, 280–284. (*invited article*)

8. Evans, H. A.; Labram, J. G.; Smock, S. R.; Wu, G.; Chabinyc, M. L.; Seshadri, R.; Wudl, F. Mono and mixed-valence tetrathiafulvalene semiconductors $(TTF)BiI_4$ and $(TTF)_4BiI_6$ with 1D and 0D bismuth-iodide networks, *Inorg. Chem.*, **2016**, *56*, 395–401.

7. Fabini, D. H.; Labram, J. G.; Lehner, A. J.; Bechtel, J. S.; Evans, H. A.; Van der Ven, A.; Wudl, F.; Chabinyc, M. L.; Seshadri, R. Main-group halide semiconductors derived from perovskite: Distinguishing chemical, structural, and electronic aspects, *Inorg. Chem.* **2016**, *56*, 11–25. *(invited Forum)*

6. Fabini, D. H.(*); Laurita, G.(*); Bechtel, J. S.; Stoumpos, C. C.; Evans, H. A.; Van der Ven, A.; Kanatzidis, M. G.; Seshadri, R. Dynamic stereochemical activity of the Sn^{2+} lone pair in perovskite $CsSnBr_3$, *J. Am. Chem. Soc.* **2016**, *138*, 11820–11832. *(*equal contribution)*

5. Evans, H. A.; Lehner, A. J.; Labram, J. G.; Fabini, D. H.; Barreda, O.; Smock, S. R.; Wu, G.; Chabinyc, M. L.; Seshadri, R.; Wudl, F. $(TTF)Pb_2I_5$: a radical cation-stabilized hybrid lead iodide with synergistic optoelectronic signatures, *Chem. Mater.* **2016**, *28,* 3607 – 3611.

4. Sheri, M.; Evans, H. A.; Doan-Nguyen, V. T.; Labram, J. G.; Wu, G.; Chabinyc, M. L.; Seshadri, R.; Wudl, F. Infinite polyiodide I_∞^- chains in the pyrroloperylene-iodine complex: Insights into the starch-iodine and perylene-iodine complexes, *Angew. Chem. Int. Ed.* **2016**, *55*, 8032 – 8035.

3. Fabini, D. H.; Hogan, T.; Evans, H. A.; Stoumpos, C. C.; Kanatzidis, M. G.; Seshadri, R. Dielectric and thermodynamic signatures of low temperature

glassy dynamics in the hybrid perovskites $CH_3NH_3PbI_3$ and $HC(NH_2)_2PbI_3$, *J. Phys. Chem. Lett.* **2016**, *7*, 376 – 381.

2. Lehner, A. J.; Fabini, D. H.; Evans, H. A.; Hébert, C.-A.; Smock, S. R.; Hu, J.; Wang, H.; Zwanziger, J. W.; Chabinyc, M. L.; Seshadri, R. Crystal and electronic structures of complex bismuth iodides $A_3Bi_2I_9$ (A= K, Rb, Cs) related to perovskite: Aiding the rational design of photovoltaics, *Chem. Mater.* **2015**, *27*, 7137 – 7148.

1. Labram, J. G.; Fabini, D. H.; Perry, E. E.; Lehner, A. J.; Wang, H.; Glaudell, A. M.; Wu, G.; Evans, H.; Buck, D.; Cotta, R.; Echegoyen, L.; Wudl, F.; Seshadri, R.; Chabinyc, M. L. Temperature-dependent polarization in field-effect transport and photovoltaic measurements of methylammonium lead iodide, *J. Phys. Chem. Lett.* **2015**, *6*, 3565 – 3571.

Abstract

Synthesis, Structure, and Optoelectronic Properties of Hybrid Metal Iodides

by

Hayden Aled Evans

The focus of this dissertation was on the preparation and analysis of new materials related to hybrid halide perovskites, AMX_3, where A = a small organic cation, M = a divalent heavy metal, and X = a halogen. It sought to understand the fundamental reasons for why the hybrid perovskites work as excellent optoelectronic materials, and to use this information to design new, stable, and less toxic materials.

This dissertation first sought to understand whether disparate slabs of metal-iodide octahedra could be electronically coupled using electronically functional organic molecules, as this could create more stable and potentially more functional materials. A well-known organic compound made famous during the advent of organic metals, tetrathiafulvalene, was used to prepare three new hybrid materials [(TTF)Pb_2I_5, (TTF)BiI_4, and $(TTF)_4BiI_6$] with some found to behave like semiconductors with 3D electronic connectivity, even though they

were structurally 1D or 2D materials. This discovery supported our original hypothesis that a more stable, layered, hybrid perovskite material could potentially exist using functional organic molecules as both structural and electronic components.

This work then extended its focus to study platinum based hybrid perovskites, A_2PtI_6 (A = small organic cation), and examined the effect of increasing cation size in Pt based vacancy ordered hybrid perovskite materials (VOHPs). This study was pertinent to our fundamental understanding of VOHPs, as by establishing structural trends caused by the small organic cations, and how different metals (Pt) behaved in these systems, future avenues for material design could be opened. It was found that the hydrogen bonding of the small organic cation to the iodides of the $[PtI_6]^{2-}$ octahedra were quite significant as cation size increased, as these interactions dictated final structure and subsequent optical properties of these materials.

In the process of understanding iodide containing hybrid perovskites, serendipitous discoveries of polyiodides were made along the way. These works include understanding the effect of hydrogen bonding in the formation of hybrid platinum oligo- and polyiodides, as well as resolving the 200 years old mystery as to what happens when starch combines with iodine.

In summary, the work presented herein is reflective of the many diverse preparation and characterization techniques needed to complete these projects: solution and solid state synthesis, and single crystal and bulk material characterization techniques ranging from crystallography, calorimetry, and optical spectroscopy. It is also a testament to the social aspect of science, as to complete this work, many collaborations needed to be formed.

Contents

List of Figures

List of Tables

Chapter 1

Development of new optoelectronic hybrid metal halide materials

1.1 The case for higher performing optoelectronic materials

Global energy consumption in 2012 was 549 quadrillion British thermal units (quad BTU, where 1 quad BTU is equal to 293 TWh) and has been steadily increasing by a few percent each year. It is projected that by 2020, global use will be 630 quad BTU's, and 810 quad BTU's by 2040.[1, 2] Currently, 85% of this energy is sourced from fossil fuels, which when burned, contribute CO_2 and other greenhouse gases to the atmosphere. These gasses over the past hundred years have had drastic effects on global climate, including an on average increase in temperature. With worldwide energy demand only set to increase the outlook looks dire. It is now understood that unless the world makes considerable adjustments to its energy production and use, the earth will soon move past a tipping-point, and enter into the age of the ”Hothouse Earth.”[1–3]

Reducing green house gas emissions, as quickly as possible, is the target goal in order to lessen the impact of global climate change. This can be achieved by replacing fossil fuel use with energy sources that are more *green*, as well as by reducing energy demand in as many ways as feasible. Current models do predict global fossil fuel use will decrease over the next 50 years,[4] but with our current trajectory, widespread demand will persist deep into the 21st century.

Fortunately, our fossil fuel dependence is slowly being replaced with one for green energy technologies, which have grown more economically viable in recent years. Furthermore, there continues to be a scientific commitment to creating more energy efficient materials and devices, such as light emitters, which we dedicate a sizable portion of the earths electricity towards operating. If these positive changes can be made on a global scale sooner than is predicted, there is still hope that the world can avoid the temperature tipping point without catastrophic cost to global economies and human livelihood.

Described below are examples of how the greater material class of hybrid metal halides, centering around the hybrid perovskites, are being examined as future advanced materials for low-cost, high efficiency, optoelectronic applications. The following sections describe current understanding of potential new photovoltaic and light emitting hybrid halide materials, as well as other considerations for the chemist searching to create new functional materials.

1.2 The advent of hybrid perovskites for solar energy applications

Solar technology, made possible by certain semiconducting materials, is an essential part of the future green energy transition. Over the past decade, solar technology has rapidly become cost competitive, owing to better manufacturing of higher efficiency materials, predominantly multi or single crystalline silicon. In 2008, solar power modules cost 3 US\$ W^{-1}, and as of 2016, this had dropped to 0.50 US\$ W^{-1}[2]. The 2020 DOE SunShot goals were for solar energy to be priced at 0.06 US\$ kWh^{-1} and 0.09 US\$ kWh^{-1} for utility and residential solar power, respectively, which are likely to be met. Certain areas of the world already opperate with this type of low-cost solar energy where it is a major portion of consumer electricity prices.[5]

At the time of this disserations writing, the most cost prohibitive aspect of photovoltaic technlogy are the installation costs of the modules.[6] This means that in order to lower the cost of PV technologies outside of the expected capital and manufacturing cost reductions that will happen over time, higher efficiency and longer lifetime (>35 years) modules are needed. To achieve this goal, current technologies should be improved (either with monumental manufacturing improvements or integration with new materials as tandem devices) or new materials/devices should be developed to replace current technologies. Based on the infrastructure already in place, the former solution is the more pragmatic option.

1.2.1 Active materials for solar technology

Fundamentally, solar cells are comprised of semiconducting materials that absorb photons and convert them into electrical energy. The maximum efficiency of a solar cell is determined by multiple factors, including how much of the solar spectrum is absorbed, how well photons are converted into electrical energy (avoiding thermalization of charge carriers), and how current density and operating voltage (fill-factor) is optimized, in the PV device. The theoretical best-case efficiency for a single-junction solar cell, based on all these limitations, is 33.7%, and will have a semiconductor material with a band gap of 1.34 eV. This is defined as the Shockley-Queisser limit.[7]

Single-junction solar cell materials can be broken down into three categories: ultrahigh efficient materials, (75% or above of the theoretical SQ efficiency limit), high efficiency materials (50% - 75%), or low efficiency materials (less than 50%).[6] Ultrahigh efficiency solar cell materials include crystalline silicon (c-Si), gallium arsenide (GaAs), or gallium indium phosphide (GaInP). These materials commercial efficiencies are close to 21% for c-Si, or as high as 28.8% for GaAs, and have device lifetimes greater than thirty years. To improve these technologies, better processing is needed to limit charge carrier recombination rates (c-Si,), and better band-gap engineering is needed for optimal light management (GaAs based materials). High efficiency materials include multicrystalline silicon (mc-Si), indium phosphide (InP), cadmiun telluride (CdTe), or hybrid perovskite solar cells (i.e. $A\mathrm{PbI}_3$, where A is some small organic cation). These, as well as the low efficiency materials, are in need of improvement to both light and carrier management, as well as a multitude of other concerns.

1.2.2 Hybrid perovskites

The hybrid perovskites mentioned in the previous section are a particularly exciting class of photovoltaic materials. Within the past decade, solar cell devices made with these materials have had efficiencies increase from 3.8%,[8] to just above 22%.[9] For crystalline silicon to reach similar efficiencies, it took close to fifty years of active research. The dramatic success of these materials is partly in thanks to serendipity, as these materials were easily solution processed with inexpensive reagents, and the first devices tested worked with the hole and electron transport layers from dye-sensitized cells.[8] These attributes opened the field to almost any device-focused research group in the world, and allowed for fast performance gains to be made.

Though these materials have impressive performance, the excitement around them has always been dampened by their poor stability. For example, if the lead hybrid perovskite materials are left exposed to air for just a few hours (in particular the iodide containing ones), the materials will rapidly degrade into the precursor reagents, lead iodide (PbI_2) and the respective alkylammonium iodide (AI). PV technologies are expected to perform for close to 30 years for the cost/benefit ratio to be commercially feasible, meaning that for successful hybrid perovskite device implementation, resources would need to be spent on encapsulating the material. In that vein, designing new materials with structural and photophysical properties similar to the hybrid perovskites, but which are more resilient, are of great interest.

In general, it is known that reducing the dimensionality of metal-iodide bonding in one or more dimensions of a hybrid perovskite crystal structure creates a compound which is distinct from the 3D parent. This has been demonstrated with various hybrid halide Ruddlesden-Popper (RP) materials which have the general formula $A_{n+1}M_n\mathrm{X}_{3n+1}$. In these $A_{n+1}M_n\mathrm{X}_{3n+1}$ materials, A is some combination of alkyl ammonium cations, M is some combination of metals, and X is some combination of halide anions.[10–12] These RP compounds are a type of layered perovskite[13] and form when additional cations of choice "break up" the anionic M-X network.

However, in the terms of hybrid iodide RP materials (the materials with the best suited band gap for PV absorption), increased stability coincides with increased charge carrier recombination rates inherent to the reduced dimensionality of the metal-iodide networks (quantum confinement effects).[14] Depending on the thickness of the metal-iodide network, and considering best case scenarios, PV device efficiencies made with these materials are only just above half of $A\mathrm{PbI}_3$ devices.[15] This increase in radiative recombination rates are why the RP materials were first examined as light emitters.[16–18]

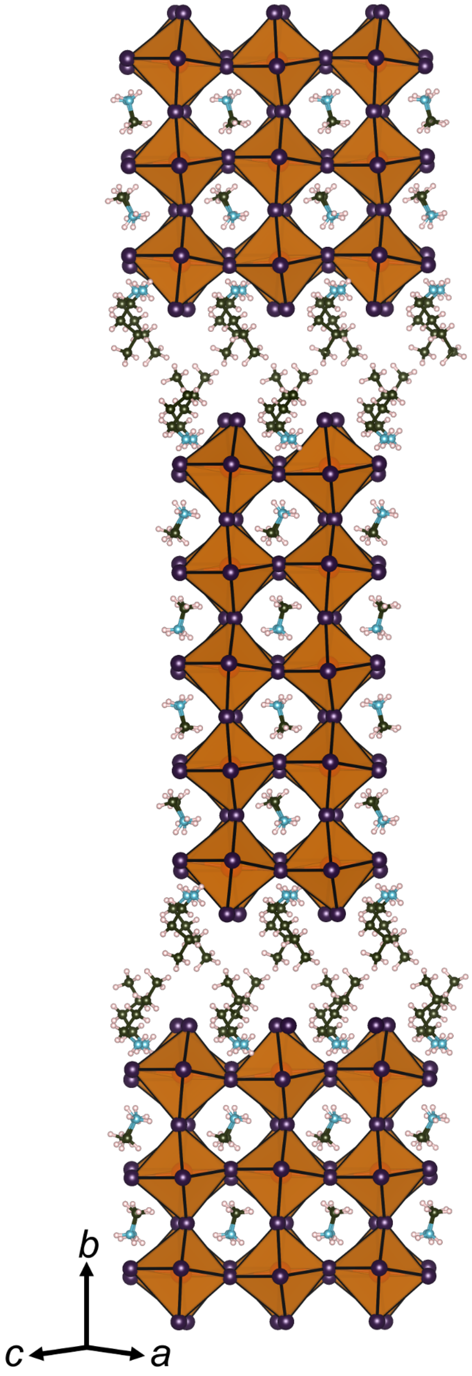

Figure 1.1: Ruddlesden-Popper $(BA)_2(MA)_4Pb_5X_{16}$,[11] a compound which illustrates the reduced dimensionality of the metal-iodide network.

The most well studied series of PV active hybrid halide RP perovskites are the butylammonium (BA) methylammonium (MA) lead iodide varieties, with the general formula $(BA)_2(MA)_{n-1}Pb_nI_{3n+1}$. As can be seen in Figure 1.1, an electronically inert layer of BA cations is used to seperate "slabs" of MA-Pb-I perovskite. Each iteration of the RP series is denoted with the variable n, where n refers to the number of lead atom layers that define the thickness of the perovskite layer. It was found by Tsai *et al.* that $(BA)_2(MA)_{n-1}Pb_nI_{3n+1}$ films, where $n = 3$ and 4, could be processed in such a way that the MA-Pb-I slabs aligned perpendicular to the contact electrodes, allowing for effective charge carrier extraction and enhanced device performance. If the films are instead cast with MA-Pb-I layers parallel to the electrodes, charge-carrier extraction must occur across the electronically insulating BA cations, which is understandably less ideal. This report produced device efficiencies of close to 12 % and stability for at least one year. Building upon that work, Venkatesan *et al.* demonstrated via diffraction and time-resolved microwave conductivity (TRMC) experiments that, in general, as n approaches infinity that there is a greater propensity for the MA-Pb-I slabs in spin-cast films to naturally align perpendicular to the electrodes.[19] Future layered RP materials for PV devices will have to strike a balance between larger MA-Pb-I slab thickness and reduced stability. The best case scenario will be to find ways to increase stability and electronically bridge the MA-Pb-I slabs so as to increase efficiency.

1.3 Past and future directions for light emitting hybrid metal halide technologies

As early as the 1990's, hybrid metal halides were studied for their potential use as light emitting materials. This work was pioneered by David Mitzi and colleagues,[16–18, 20] who as of this dissertations writing, still contribute to this field. These compounds were described to have many attractive qualities for these applications, namely that they were solution processable, displayed high charge transport through the metal-halide matrices, and could be synthetically tuned to the desired optical response. The tuning was achieved by varying the constituent metal-halide elements, as well as with the organic cation used to create *space* between the metal-halide network. Chromophores, as well as functionally innocent organic cations (butyl ammonium or other long chain aliphatic ammonium cations) could be used to create a material that elicits an optoelectronic response from either the organic or inorganic layers, depending on what is desired.[20]

Furthermore, certain members of these layered hybrid perovskite materials display broadband white light emission. This has been covered by those from the Karunadasa group,[21, 22] where they described how both (001) and (110) layered perovskites luminesce when excited with UV light. The origin of this luminescence is speculated to be caused by the self-trapped excitonic states which cause lattice deformations of the metal-halide network. These self-trapped states radiatively recombine with varying energy, to produce white light.

There is now greater understanding of how the organic layers can be used to template the type of metal-iodide connectivity in these layered hybrid metal-halide materials,[23] which in the case of white light emitters, tune the type of emission. This kind of synthetic control is at the heart of future material design in this area.

1.4 Favorable properties of iodine containing vacancy ordered double perovskites

It has been shown that 3D I-M-I connectivity of the metal iodide layers, as is seen in the parent AMI_3 perovskites, is not *exactly* necessary for favorable charge transport properties. This is due to the large and diffuse orbitals of the iodide anions which display some appreciable amount of orbital dispersion, even

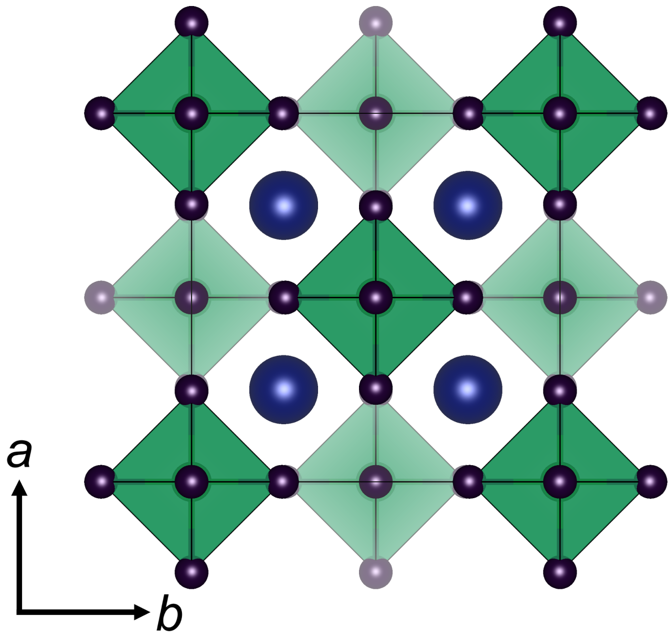

Figure 1.2: Vacancy-ordered double perovskite, Cs_2SnI_6. Depth fading is used to indicate that the lighter colored $[SnI_6]^{2-}$ octahedra are located further back in the structure.

at Van der Waals distances. For example, in the case of the material Cs_2SnI_6, DFT calclatuions predictated that the conduction and valence frontier bands are made of predominantly of iodine p states and are generally quite disperse, leading to such things as favorable hole transport.[24, 25] This is quite exciting, as these vacancy ordered double perovskites (VODPs) are quite stable. However, the I-I proximity is not the only attribute that matters as it has been established that the nature of the metal electronegativity VODPs is significant [metals of greater electronegativity than Sn (i.e. Te) will create deep trap states.][26]

If one is to decrease the dimensionality of a metal-halide material in the name of increasing stability, finding ways to increase I-I proximity in other ways could mitigate unintended negative effects. Work by Shestimerova *et al.* has demonstrated that both I_2 and the oligoiodide anion, I_3^-, increases band dispersion in hybrid halide materials.[27, 28] In all cases, there is limited covalency between the I_3^- or I_2 molecule with any of the metal-iodide octahedral iodides, indicating that mere proximity between I atoms is enough to induce favorable optoelectronic properties.

1.5 Dissertation perspective

Designing new materials which eliminate unwanted properties (i.e. poor stability) of the perovskites whilst not inadvertently eliminating others (i.e. PV activity or light emission) is complex. For this dissertation, we thought it more informative to try and understand a small subspace of change — the effects of reducing the dimensionality of hybrid metal iodide materials with both functional, and small non-functional, organic cations. Two main questions covered in this dissertation are: “How do complex functional cations behave in reduced dimensionality metal-iodide materials?” and “what are there overarching structural effects of small, commonly used, organic cations in vacancy-ordered hybrid perovskites?” The following chapters in this dissertation address these questions, as well as others, and provide general thoughts on synthetic approaches to future optoelectronic metal-halide material design.

Chapter 2

(TTF)Pb_2I_5: a radical cation-stabilized hybrid lead iodide with synergistic optoelectronic signatures

The compound described in this chapter, (TTF)Pb_2I_5, was the first prepared of the tetrathiafulvalene metal halide compounds characterized in this dissertation. A description of the properties of the other two, (TTF)BiI_4 and (TTF)$_4BiI_6$,

---

[1] Anna J. Lehner, John G. Labram, Douglas H. Fabini, Omar Barreda, Sara R. Smock, Guang Wu, Michael L. Chabinyc, Ram Seshadri, and Fred Wudl have contributed to the contents of this chapter.

as well as a comparison between all three tetrathiafulvalene compounds, can be found in Chapter 3. In this chapter, preparation, property analysis, and DFT calculations are reported for (TTF)Pb_2I_5, verifying that (TTF)Pb_2I_5 is a narrow gap semiconductor with optical properties synergistically influenced by the $TTF^{+\bullet}$ cations. The $TTF^{+\bullet}$ cations contribute to states in the electronic gap which are formed by orbitals in the inorganic framework.

Previous publication of this data can be found in *Chemistry of Materials*,

> Evans, H. A.; Lehner, A. J.; Labram, J. G.; Fabini, D. H.; Barreda, O.; Smock, S. R.; Wu, G.; Chabinyc, M. L.; Seshadri, R.; Wudl, F. (TTF)Pb_2I_5: a radical cation-stabilized hybrid lead iodide with synergistic optoelectronic signatures, *Chem. Mater.* **2016**, *28*, 3607 – 3611.

2.1 Introduction

Hybrid organic-inorganic materials can potentially combine the properties of highly tunable functional organics with those of complementary inorganic networks in a single material. Distinct control over what is desired from each component becomes possible in such materials, allowing the functions of the organic and inorganic components to work synergistically. Tetrathiafulvalene (TTF), the organic component used to examine this potential benefit is a precursor to some of the early organic metals, and was a clear choice when choosing a functional organic. It was first reported by Wudl *et al.* in the early 1970's,[29, 30] and has been studied for its impressive electron donating abilities,[31, 32] including derivatives displaying superconductivity.[33]

Hybrid compounds containing TTF have also shown novel magnetic and electronic properties. Devic *et al.*[34, 35] reported a ethylenedithio-1,2-diiodotetrathiafulvalene (EDT-TTF-$I_2^{+\bullet}$) hybrid with metallic character, and showed its metal-insulator transition to be preserved within a hybrid compound with PbI_2. Kondo *et al.*[36] similarly reported $TTF^{+\bullet}$ hybrids containing Sn and Cl/Br, all which display semiconducting behavior due to interactions through the extended TTF networks. Magnetic compounds with TTF derivatives have also been made with transition metal halides, and found to be composed of two kinds of donor columns which magnetically couple with the anions through close contact between metal halide interactions.[37] Metal-organic-frameworks (MOFs), a related class of hybrid materials, generally possess poor electronic functionality, but attempts to prepare electrically conductive MOFs have recently been made. Examples include incorporating a conjugated molecule within the framework directly,[38] as a guest that electronically couples metal atoms in the framework using (TCNQ),[39] or modification of an insulating MOF.[40, 41] Stavila *et al.*[42] have recently reviewed this topic.

Layered lead halides, in their own right, are an attractive set of materials with rich optoelectronic and semiconducting behavior. The extensive work of Mitzi and coworkers[16, 17] in the late 1990's first highlighted how amines and diammines combine with main group halides to form unique layered perovskite structures, which motivated the chemistry of organic ammonium cation "spacers" to flourish. Following the work of Kojima *et al.*[8] demonstrating the use of perovskite $CH_3NH_3PbI_3$ materials as solution deposited photovoltaics, there has been a huge flurry of research in this space to enhance the stability of the air unstable compound. This has included the use of ammonium "spacer" chemistry by Smith *et al.*[10] which improved stability of a layered perovskite incorporating phenylethylammonium ions into the structure. Cao *et al.*[43] also explored this idea with butylammonium instead of phenylethylammonium, and reported that the extent of ammonium spacer incorporation as well as growth direction of subsequent films had significant impact on functionality of their light absorbing devices. Maughan *et al.*[44] recently highlighted how the unusual aromatic cation tropylium$^+$ can stabilize and electronically couple with tin and lead halide networks, helping to defining the position of either the conduction band maximum or valence band minimum.

In this chapter, preparation, property analysis, and DFT calculations are reported for (TTF)Pb_2I_5, verifying that (TTF)Pb_2I_5 is a narrow gap semiconductor with optical properties synergistically influenced by the $TTF^{+\bullet}$ cations. The $TTF^{+\bullet}$ cations contribute to states in the electronic gap which are formed by orbitals in the inorganic framework.

2.2 Experimental methods

(TTF)Pb_2I_5 crystals were grown under argon atmosphere by dissolving PbI_2 (110 mg, 0.239 mmol) and tetrabutylammonium iodide (168.2 mg, 0.455 mmol) in dimethylformamide (DMF, 1 cm^3) at ambient temperature. Following complete dissolution, a separate solution of $(TTF)_3(BF_4)_2$ (20 mg, 0.0254 mmol) prepared following the reported procedure,[45] in DMF (3 cm^3) was added drop-wise. The resulting mixture is transparent and red hue when dilute, but is brown as carried out here. This mixture was layered with of acetonitrile (MeCN, 6 cm^3) as a non-solvent and left at room temperature for two days. Small dark bundles of crystals were formed beneath an unreacted PbI_2 layer. These bundles were isolated by washing with cold DMF, air dried, and finally dried in vacuum. The dark crystal bundles, when broken up, yield red rectangular single crystals. The material was observed stable in air for a month, but longer time study is needed.

Single Crystal X-ray diffraction data for (TTF)Pb_2I_5 was collected on a Bruker KAPPA APEX II diffractometer equipped with an APEX II CCD detector using a TRIUMPH monochromator with a Mo Kα X-ray source (α = 0.71073 Å). The crystals were mounted on a cryoloop under Paratone-N oil and the data reported here was collected at room temperature. Absorption correction of the data was carried out using the multiscan method SADABS.[46] Subsequent calculations were carried out using SHELXTL.[47] Structure determinations were done using direct methods. All hydrogen atom positions were omitted. Structure solution, refinement, and creation of publication materials were performed using SHELXTL. The graphical depiction used in the main paper was done with the program VESTA.[48]

Product purity of (TTF)Pb_2I_5 was established via Powder X-ray diffraction (PXRD), acquired with a Pananalytical Empyrean Powder XRD machine. Experimental PXRD was compared with a simulated PXRD pattern that was generated from single crystal X-ray diffraction data using the GSAS software suite.[49, 50]

Thermogravimetric measurements were preformed using a TA Instruments Discovery TGA, with a rate of 25 cm^3/min dry nitrogen purge and a temperature ramp rate of 10°C/min. The maximum temperature of the experiment was

800°C.

The electron spin resonance (ESR) simulation was performed using the pepper function, which is a standard part of Easy Spin.[51] The three g tensors reported were utilized as individual values with equal weighting. The crystal space group was included in the calculation as well as the possible angles of position. These angles helped to account for the random orientation of the powder solid-state ESR sample. The angles used were [0 0 0; 0 $\pi/4$ 0; 0$\pi/8$ 0; 0 $\pi/16$ 0; 0 $\pi/32$ 0; 0 $\pi/64$ 0]. A Gaussian broadening was also applied at a value of 0.3 to all g tensors.

Band structure calculations of (TTF)Pb_2I_5 based on density functional theory (DFT) were carried out using the Vienna ab initio Simulation Package (VASP)[52–55] which implements the Kohn-Sham formulation using a plane wave basis and the projector-augmented wave formalism (PAW).[56, 57] The input structure was generated from the single crystal diffraction data by adding the aromatic H atoms to the $TTF^{+\bullet}$ radical cation and constraining them within the normal riding model of the HFIX function of the crystallographic refinement software SHELXL-2014.[58, 59] We decided to use this input model without any DFT structure optimization as the relaxed structure exhibited an increased volume (9 %) and considerable deviations in polyhedral volumes for the complex Pb-I anions compared to the crystallographic results, potentially as a result of van der Waals interactions not being appropriately captured. The energy cut-off of the plane wave basis set was 500 eV and a γ-centered k-mesh grid with 24 k-points was employed, with the convergence criteria set at 0.01 meV. The Perdew-Burke-Ernzerhof (PBE)[60] version of the Generalized Gradient Approximation for employed for the exchange-correlation energy. The high-symmetry points were selected for the conventional Brillouin zone of the space group $P2_1/c$ using the Bilbao Crystallographic Server.[61] For more accurate band gap values and density of states (DOS), a screened hybrid functional (HSE06)[62, 63] was employed. Spin-orbit coupling (SOC), which we found to be necessary to accurately describe the band structures of related lead[64] and bismuth[65] halides were not employed in the results presented here: SOC affects only the band dispersion of the Pb states which do not contribute significantly to the states around the band gap in (TTF)Pb_2I_5. For comparison, the electronic structure of $TTFI_3$[66] ($P2_1/n$) was calculated using the same computational scheme, and is provided in the Supporting Information. The calculated band gap (HSE-level) of 1.02 eV is indirect between the valence band maximum (VBM, C) and the conduction band minimum (CBM, D) and corresponds to a transition between filled and empty sulfur p and carbon p states. Its magnitude is only marginally smaller than the smallest direct transition (1.03 eV) which is located at the special k point C.

Four-probe transport measurements were conducted using the setup shown in Figure 2.1. Measurements were done courtesy of John Labram.

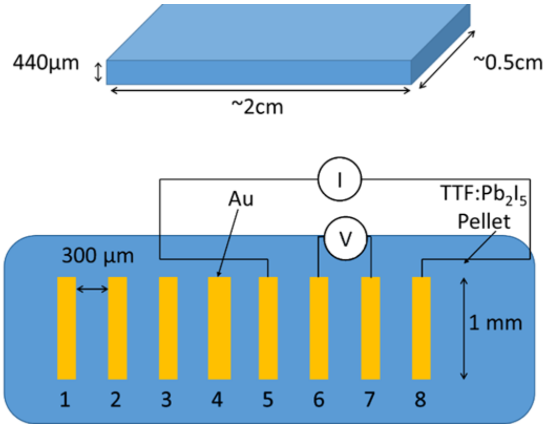

Figure 2.1: Cartoon depiction of the 4-probe setup employed for the IV measurements. Gold contacts were evaporated onto a pressed pellet of (TTF)Pb_2I_5, and contacts 5 through 8 proved most reliable for measurements. These were wired, and utilized in the reported measurements according to the above schematic.

2.3 Results and discussion

Single crystal X-ray diffraction carried out on multiple crystals of (TTF)Pb_2I_5 confirmed the structure depicted in Figure 2.2, with pertinent crystrallographic data from the structure solution listed in Table 2.1. Figure 2.2(a) illustrates different views of the (TTF)Pb_2I_5 structure, with some structural details in the caption. The structure comprises sheets of corner and edge sharing lead iodide

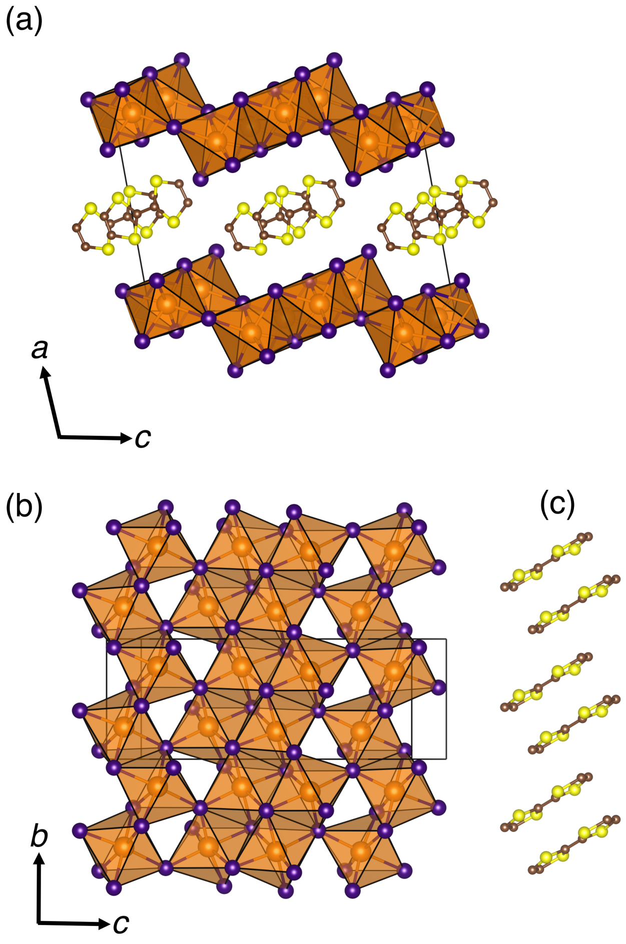

Figure 2.2: The crystal structure of the title compound (TTF)Pb_2I_5. (a) View down the b-axis showing the corrugated $Pb_2I_5^-$ layers. (b) A top view of the lead iodide layers, showing both edge and corner sharing of the octahedra. (c) $TTF^{+\bullet}$ radical cations extend infinitely in stacks, with complete overlap as dimers, and partial overlap with the next nearest neighbor dimer pair. Space group $P2_1/c$, $a = 12.90(3)$ Å, $b = 7.97(1)$ Å, $c = 20.23(2)$ Å, $\beta = 100.25(7)^\circ$, Z = 4, $R_1 = 0.0643\,\%$, $wR_r = 0.0872\,\%$.

Table 2.1: Crystallographic information for (TTF)Pb_2I_5 single crystal analysis performed at room temperature

Empirical Formula	$(C_6H_4S_4)Pb_2I_5$
Crystal habit, color	Block, red
Crystal system	Monoclinic
Space group	$P2_1/c$
Volume (Å^3)	2048(6)
a (Å)	12.90(3)
b (Å)	7.97(1)
c (Å)	20.23(2)
α (°)	90
β (°)	100.25
γ (°)	90
Z	4
ρ (g mol^{-1})	1249.18
Dens. (g cm^{-3})	4.051
Abs. (mm^{-1})	24.344
F_{000}	2116
Reflections (unique)	13229 (4124)
R_{int}	0.2030
R_1	0.0643
wR_R	0.0872
∂F ($e\mathring{A}^{-3}$)	1.685 and -1.591
GOF	0.945

octahedra, separated by $TTF^{+\bullet}$ cations that form infinite "stacks". The $TTF^{+\bullet}$ stacks are eclipsed in dimers, and maintain a consistent intra-dimer distance of 3.32 Å. The stacks extend through the crystal with an incomplete overlap with the next nearest TTF pairs, with an inter-dimer distance of 3.52 Å, as shown in 2.2(c). It is interesting to note that this stacking structure of the TTF radical cations is commensurate with the corrugated sheet structure of the Pb-I sheets. In contrast to the previous work on EDT-TTF-I_2 iodoplumbates reported by Devic *et al.*,[34] there is no disorder of the radical cation, which were reliably located over the temperature range of 300 K to 100 K. There is a slight contraction of the unit cell at 100 K, but no structural transition was observed in this temperature range.

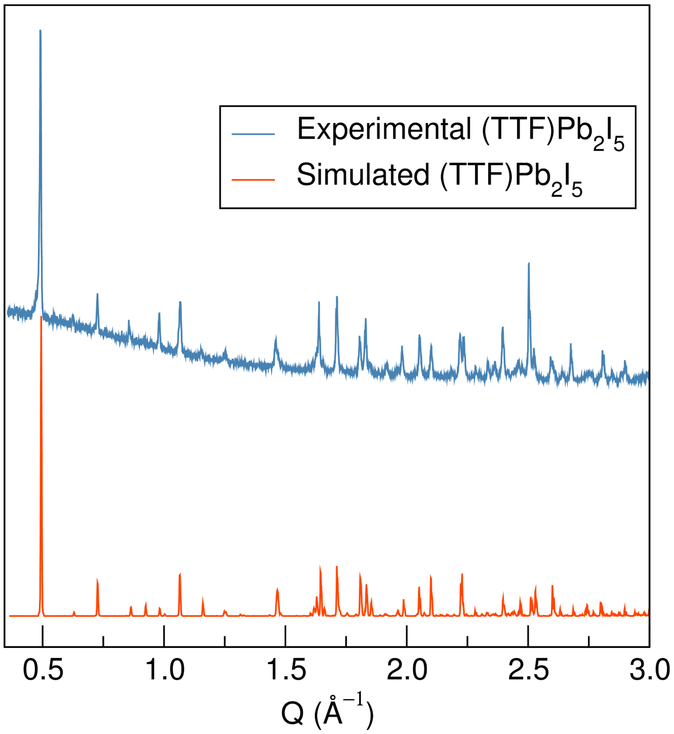

Figure 2.3: Experimental PXRD pattern of bulk (TTF)Pb$_2$I$_5$ and the simulated PXRD for comparison.

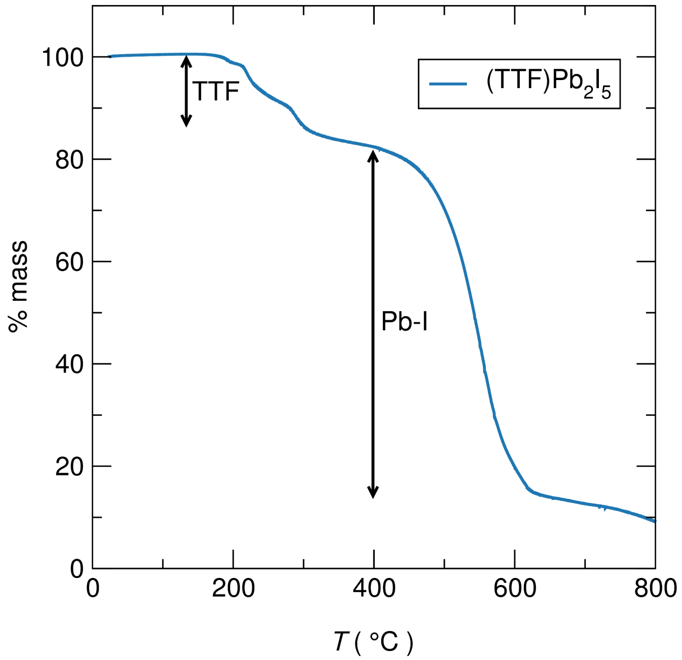

Figure 2.4: TGA data for the compound (TTF)Pb_2I_5. The organic component (tetrathiafulvalene, TTF) is the first weight loss near 200°C, as the mass loss matches the percent weight of TTF in (TTF)Pb_2I_5 ($\sim$19%)

Bulk purity of (TTF)Pb_2I_5 was established via PXRD, with the data presented in Figure 2.3. Thermogravimetric analysis of (TTF)Pb_2I_5 is shown in Figure 2.4, and depicts a decomposition with mass losses proportional to the constituent components.

Figure 2.5(a) displays UV-Vis spectra obtained for (TTF)Pb_2I_5, as well as the starting material, $(TTF)_3(BF_4)_2$. The spectra were obtained using a Shimadzu UV3600 UV-NIR Spectrometer in diffuse reflectance mode using an integrating

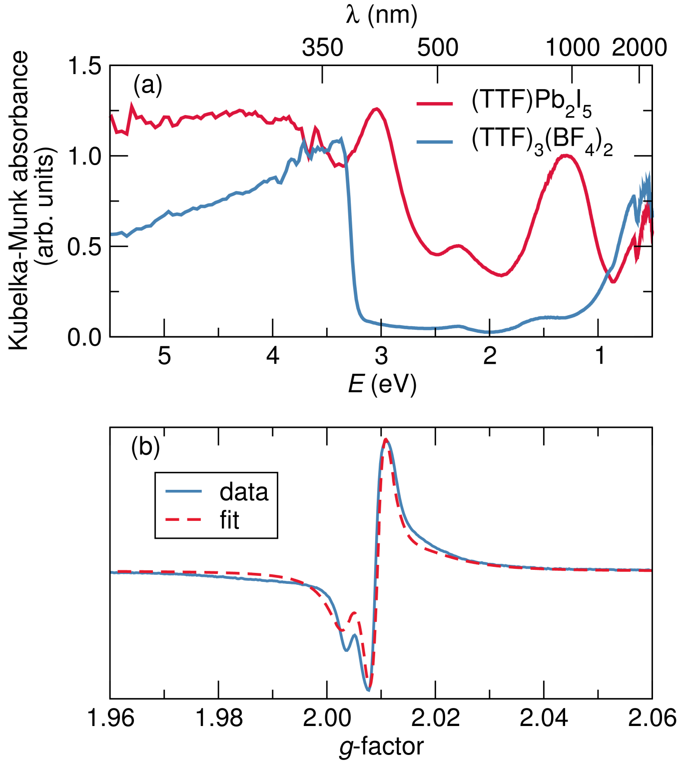

Figure 2.5: (a) Kubelka-Munk absorbance obtained from transformation of the diffuse reflectance of (TTF)Pb$_2$I$_5$, as well as the precursor salt (TTF)$_3$(BF$_4$)$_2$ and TTFI$_3$ for comparison. (b) Room temperature ESR signal for polycrystalline (TTF)Pb$_2$I$_5$ sample, 9.2898 GHz, with simulation g values of 2.0110, 2.0083, 2.053.

sphere, where samples were diluted with $BaSO_4$ prior to measurement. Relative absorbance was obtained from Kubelka-Munk transformation of the reflectance spectra. Prior work from Sugano et. al[67] and Torrance *et. al*[68, 69] were the main sources used for interpreting the presented spectra. The insulating TTF salt, $(TTF)_3(BF_4)_2$, has a structure comprising dimers and neutral TTF that are staggered with distances varying between 3.4 Å and 3.48 Å.[70] We observe noticeable absorptions for this salt near 0.6 eV which are attributed to intermolecular charge transfer from TTF^0 to $TTF^{+\bullet}$, as well as an absorption attributed to an intramolecular transition for a lone $TTF^{+\bullet}$ within a dimer at 3.18 eV.[67, 69] The weak peaks at 1.5 eV and 2.3 eV are an intradimer transition and an intramolecular $TTF^{+\bullet}$ transition, respectively.[69]

Considering what is already known for monovalent and mixed valence $TTF^{+\bullet}$ salts the absorption spectra of the title compound is not surprising. The broad band that peaks near 1.3 eV is from intradimer charge transfer, and the absorptions that peak at 2.3 eV and 3.0 eV are intramolecular transitions of the $TTF^{+\bullet}$. What is unexpected however, is the low energy absorption at 0.6 eV which is attributed to intermolecular charge transfer from TTF^0 to $TTF^{+\bullet}$. Although no crystallographically observed TTF^0 is present in our sample, we believe the cause of this absorption is back charge transfer from the Pb-I network to $TTF^{+\bullet}$, in a manner similar to how $TCNQ^{-\bullet}$ back charge transfers to NMP^+

in NMP-TCNQ.[68] Furthermore, the sustained absorption over the 3.0 eV to 5.5 eV range is not usually seen for $TTF^{+\bullet}$ salts, which we attribute to absorption from the Pb-I network. As seen in Figure 3.5, the absorptions for the compound $(TTF)BiI_4$ indicate similar behavior.

Figure 2.5(b) displays Electron spin resonance (ESR) spectra of powder samples of $(TTF)Pb_2I_5$, providing evidence of the radical cation state of $TTF^{+\bullet}$ at room temperature. The signal is centered close to the value for a free electron with an asymmetrical signal shape suggestive of some itinerant electron character, consistent with the observed free-carrier behavior.[71] The simulation of the EPR spectrum, which is depicted in Figure 2(b) as a dashed line, was carried out using Easy Spin,[51] described in the Experimental Methods section of this chapter.

For the DOS and band structure of $(TTF)Pb_2I_5$, which were calculated by Dr. Anna Lehner, we find the states of the $TTF^{+\bullet}$ radical cation to be energetically surrounded by filled states of the anti-bonding interaction between the lone-pair Pb s^2 states with the halogen p states in the valence band and by empty Pb p states in the conduction band. In other hybrid lead halides with simple aliphatic carbon hydrate counter cations, such as $CH_3NH_3PbI_3$, the filled counter-cation states are energetically far below the Fermi energy and the surrounding Pb-I states constitute the VBM and CBM. The band dispersion of the $TTF^{+\bullet}$ states

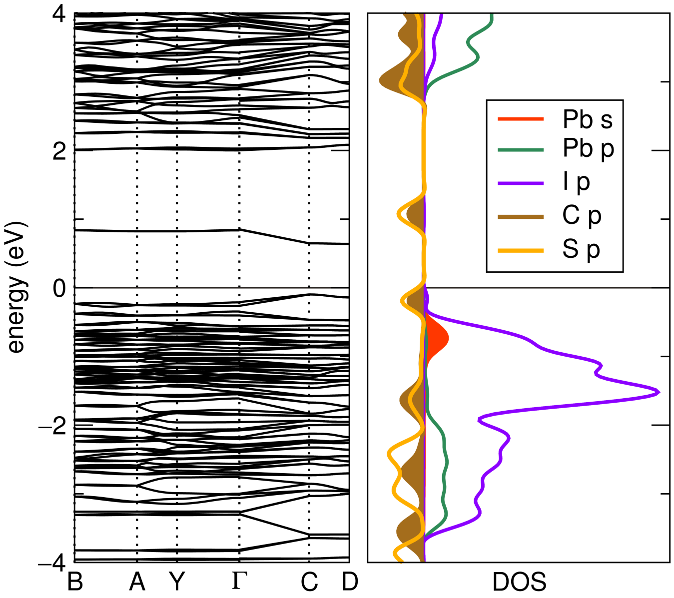

Figure 2.6: Band structure (PBE) and DOS (HSE06) for (TTF)Pb_2I_5. The DOS contributions of the C and S p states from $TTF^{+\bullet}$ and the Pb and I contributions have been separated for added clarity. Credit: Anna Lehner for calculations

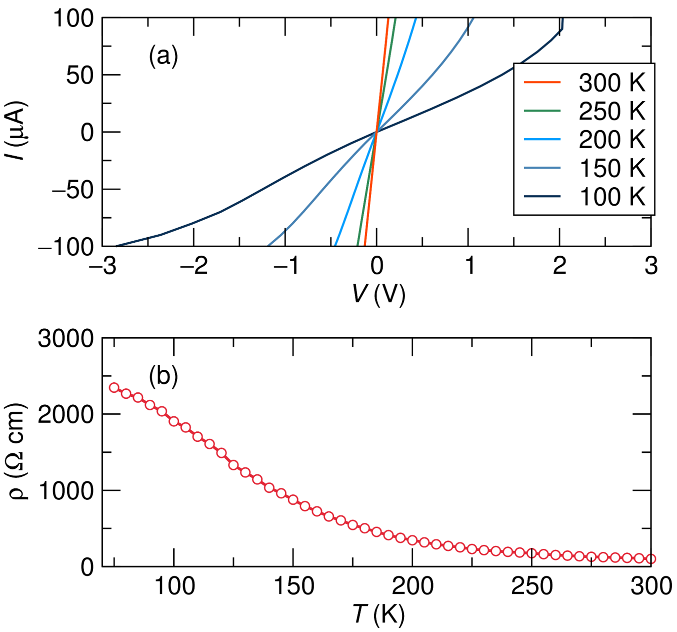

Figure 2.7: Four probe current-voltage (IV) measurements for (TTF)Pb_2I_5. (a) IV characteristics over the 100 K to 300 K range. (b) ρ vs. T between 75 K and 300 K. The room temperature resistivity of the pressed pellet is close to 100 Ω cm.

around the band gap is relatively moderate, as would be expected of the 1D stacks.

Four-probe electrical resistivity measurements were carried out on a pressed pellet of polycrystalline (TTF)Pb_2I_5 with evaporated gold contacts (schematic shown in the SI), by Dr. John Labram. Figure 4(a) shows I-V curves from 100 K to 300 K, suggesting nearly Ohmic behavior near the origin. As can be seen from Figure 4(b), as temperature is increased from 75 K to 300 K the resistivity of (TTF)Pb_2I_5 decreases by two orders of magnitude. The conductivity of the pressed pellet of the title compound is considerably higher than related monocation salts [(TTF)$Br_{1.0}$ and (TTF)$Cl_{1.0}$] which have conductivities close to 10^{-6} S cm^{-1} when measured similarly.[72] We believe the increased conductivity can be attributed to the synergistic effect of the inorganic network.

In summary, (TTF)Pb_2I_5 is a TTF radical cation stabilized semiconductor with electronic and optical properties of the compound greatly influenced by the $TTF^{+\bullet}$ radical cation. The material shows optical signatures indicative of a back-charge transfer between the $TTF^{+\bullet}$ radical cations, and a room-temperature resistivity close to 100 Ω cm (conductivity greater than 0.01 S cm^{-1}. We believe these types of synergistic hybrid systems to be potentially promising materials as next generation photovoltaic materials and other optoelectronic applications, that encourages further exploration.

Chapter 3

Mono and mixed-valence tetrathiafulvalene semiconductors (TTF)BiI$_4$ and (TTF)$_4$BiI$_6$ with 1D and 0D bismuth-iodide networks

Two compounds containing tetrathiafulvalene (TTF) cations with extended and discrete anions based on Bi and I are discussed in this Chapter. The compound (TTF)BiI$_4$ comprises [BiI$_2$I$_{4/2}$]$^-$ chains of edge-shared octahedra that are

---

[1] John G. Labram, Sara R. Smock, Guang Wu, Michael L. Chabinyc, Ram Seshadri, and Fred Wudl have contributed to the contents of this chapter. Tomer Levi and Jon Schuller provided guidance regarding the FTIR polarized light experiments/instrumentation.

interspersed with stacks of $TTF^{+\bullet}$. The compound $(TTF)_4BiI_6$ has mixed-valence stacks of TTF and $TTF^{+\bullet}$ and discrete molecules of $TTF^{+\bullet}$ separated by discrete $[BiI_6]^{-3}$ anions. The optical and electrical transport properties of these compounds are reported, and compared with $(TTF)Pb_2I_5$ from Chapter 2. Due to the mixed-valence stacks of TTF, $(TTF)_4BiI_6$ is the significantly better electrical conductor than $(TTF)BiI_4$, despite the discrete nature of the inorganic moiety.

Previous publication of this data can be found in *Inorganic Chemistry*,

> Evans, H. A.; Labram, J. G.; Smock, S. R.; Wu, G.; Chabinyc, M. L.; Seshadri, R.; Wudl, F. Mono and mixed-valence tetrathiafulvalene semiconductors $(TTF)BiI_4$ and $(TTF)_4BiI_6$ with 1D and 0D bismuth-iodide networks, *Inorg. Chem.*, **2016**, *56*, 395–401.

3.1 Introduction

Hybrid organic-inorganic materials combine the easily tuned properties of designer organic compounds with functionally and chemically diverse inorganic networks. A high degree of control is possible in such systems, enabling design of materials which can exploit the benefits of the organic and inorganic components. Tetrathiafulvalene, the functional organic cation found in the two compounds of focus in this chapter, is a precursor to some of the earliest organic metals and was chosen here for its propensity to form extended $\pi - \pi$ stacks in the solid state. TTF was first reported by Wudl *et al.* in the early 1970's[29, 30] and further studies have exploited the ability of TTF and its derivatives to donate electrons[31, 32], superconduct,[33] and aid magnetic communication.[37] Prior examples of TTF and TTF derivatives containing metal-halide compounds include the superconducting hybrid of bis(ethylenedithio)-tetrathiafulvalene (BEDT-TTF) with tetracyanometallates,[73] ethylenedithio-tetrathiafulvalene (EDT-TTF) compounds of Ag and Pb iodides that are metallic,[34, 35] the insulating (BEDT-TTF)BiI_4,[74] and semiconducting compounds (BEDT-TTF)$BiBr_4$,[75] $(BEDT\text{-}TTF)_2[Au(i\text{-}mnt)_2$[75], $TTF_3(SnCl_6)$[36], and BEDT-TTF and EDT-TTF salts with Te and I.[76] All aforementioned compounds had electrical and optical properties heavily influenced by the packing of the TTF related moiety.

Interestingly, TTF based molecular-organic frameworks (MOFs) also show structure dependent electrical properties related to how the TTF $\pi - \pi$ systems interact along the framework. Recent work by Dincă and coworkers found a direct correlation between S–S atomic distances between neighboring TTF molecules on the overall conductivity of transition metal containing MOFs.[38, 77] Alternatively, there are also MOFs which incorporate electronically active organic molecules into the porous voids (rather than in the framework) to promote charge transport by coupling to the metal centers.[39–41] Recent reviews describe the general design challenges surrounding conductive MOFs,[42, 78, 79] and summarize current state-of-the-art material performance. To date, the most conducting MOF ($Cu_3(BHT)_2$)[80] has a conductivity of $1.58 \times 10^3\,S\,cm^{-1}$ which is comparable to two of the most studied organic metals, $NMP^{+}TCNQ^{-\bullet}$ and $TTF^{+\bullet}$-$TCNQ^{-\bullet}$. [68, 81, 82]

The high conductivity of $NMP^{+}TCNQ^{-\bullet}$ and $TTF^{+\bullet}$-$TCNQ^{-\bullet}$ is attributed to a back charge-transfer wherein no well-defined neutral species are seen in the crystallography of these compounds, but the properties displayed suggest the presence of some small fraction of such neutral species (due to back charge-transfer), facilitating high measured conductivities. In Chapter 2 we discussed a monovalent TTF hybrid, similarly containing no neutral TTF (TTF^0), but only radical cations $TTF^{+\bullet}$: $(TTF)Pb_2I_5$,[83] displaying synergistic optical and electronic properties associated with back charge-transfer between the $TTF^{+\bullet}$ stacks and the extended Pb–I network. Low energy (sub 1.0 eV) optical signatures were observed in the powder optical absorption spectrum of $(TTF)Pb_2I_5$, which are usually only seen in spectra of mixed-valence TTF halide salts, and attributed to an efficient hopping charge-transfer along the mixed-valence TTF stacks.

[67, 69] Furthermore, (TTF)Pb_2I_5 also displayed conductivity much higher than related monovalent $TTF^{+\bullet}$ salts.[72]

In this Chapter, we dsicuss two tetrathiafulvalene-containing hybrid compounds with Bi and I anion networks. All the TTF are monovalent in (TTF)BiI_4, while $(TTF)_4BiI_6$, with TTF and $TTF^{+\bullet}$, displays mixed-valence which appears to have profound implications for electrical transport; $(TTF)_4BiI_6$ is significantly the better electrical conductor. The compounds contain varying degrees of metal-iodide and $TTF^{+\bullet}$ connectivity, providing a good comparison between hybrid monovalent and mixed-valence TTF bismuth-iodide salts. Additionally, one of the bismuth containing systems, $(TTF)_4BiI_6$, crystallizes in a unique structure type where monovalent $TTF^{+\bullet}$ is isolated from an extended network of neutral TTF and $TTF^{+\bullet}$. To our knowledge this is seldom seen in TTF-derivative compounds and has yet to be documented for $TTF^{+\bullet}$ compounds. We also pay close attention to the potential nature of electronic interactions between the inorganic framework and the TTF stacks in (TTF)BiI_4.

3.2 Experimental methods

(TTF)BiI_4 and $(TTF)_4BiI_6$ were prepared in solution, similar to what was used for (TTF)Pb_2I_5.[83] For the preparation of (TTF)BiI_4 a solution of 240 mg

(0.407 mmol) bismuth iodide (BiI_3, Strem 99.999%) and 75.8 mg (0.206 mmol) tetrabutylammonium iodide (TBAI, Sigma-Aldirch, 98%) was made in 2 cm^3 dimethylformamide (DMF anhydrous, Sigma-Aldirch) at room temperature. Once this solution was dissolved, a 3 cm^3 DMF solution of 60 mg (0.0762 mmol) tetrathiafulvalene fluoroborate $[(TTF)_3(BF_4)_2]$[45, 70] was added drop-wise over five minutes, and allowed to stir for 15 minutes. This reaction mixture was then opened to air, layered with 5 cm^3 acetonitrile (MeCN) as a non-solvent, and covered. $(TTF)BiI_4$ crystallized over the course of three days and was separated from the mother liquor, washed with MeCN, and air dried. It crystallizes as black plates 0.5 mm to 1.0 mm on edge. $(TTF)_4BiI_6$ is made following the same procedure, except that 120 mg (0.203 mmol) BiI_3 is used instead. $(TTF)_4BiI_6$ crystallizes as much smaller black blocks. Both crystals appear red under a microscope when made sufficiently thin.

Single crystal x-ray diffraction data for $(TTF)BiI_4$ and $(TTF)_4BiI_6$ were collected on a Bruker KAPPA APEX II diffractometer equipped with an APEX II CCD detector using a TRIUMPH monochromator with a Mo Kα X-ray source (α = 0.71073 Å). The crystals were mounted on a cryoloop under Paratone-N oil. Absorption correction of the data was carried out using the multiscan method SADABS.[46] Subsequent calculations were carried out using SHELXTL.[47] Structure determinations were done using direct methods. All hydrogen atom positions were omitted. Structure solution, refinement, and creation of publication materials were performed using SHELXTL. The graphical depictions used in the main paper was created with the software suite VESTA.[48]

The growth orientation of (TTF)BiI_4 single crystals was established on the aforementioned Bruker KAPPA APEX II diffractometer equipped with an APEX II CCD detector using a TRIUMPH monochromator with a Mo Kα X-ray source ($\alpha = 0.71073\,\text{Å}$). The crystals were mounted on a cryoloop under Paratone-N oil. The unit cell was indexed, and using the APEX2 software suite, plane orientations established.

PXRD data was acquired on a Pananalytical Empyrean Powder XRD machine, and was utilized to establish bulk sample purity of isolated (TTF)BiI_4 and $(TTF)_4BiI_6$ over the course of our experiments. We compared experimental PXRD with simulated patterns generated from single crystal x-ray diffraction data using the software suite GSAS.[49, 50] The data was performed open to air.

A TA Instruments Discovery TGA was utilized for TGA of (TTF)BiI_4 and $(TTF)_4BiI_6$. A rate of 25 cm^3/min dry nitrogen purge was employed with a temperature ramp rate of 10°C/min. The maximum temperature of the experiment was 650°C.

Solid state electron spin resonance (ESR, also known as electron paramagnetic resonance, EPR) spectra were taken at room temperature, using a X-band Bruker EMXplus EPR Spectrometer. The electron spin resonance (ESR) simulation was performed using the pepper function, using Easy Spin.[51]

The powder UV-Vis spectra were gathered with a Shimadzu UV3600 UV-NIR Spectrometer in diffuse reflectance mode with an integrating sphere, after suspending the title compounds in $BaSO_4$ medium. These reflectance spectra were then Kubelka-Munk transformed for relative absorbance spectra. Single crystal optical experiments were conducted on multiple (TTF)BiI_4 crystals with a developed (010) face. The single crystals were measured on a gold substrate. The experiments were conducted using an FTIR (Vertex 70, Bruker) coupled to an infrared microscope (Hyperion 3000, Bruker). Data were collected averaging over 1,000 scans with $4\,\mathrm{cm}^{-1}$ resolution. The microscope was operated in either spectroscopy or imaging modes (used to identify the desired single crystals). In spectroscopy mode, we performed reflection measurements where the infrared radiation was focused on the sample by a 15× Cassegrain objective. The reflected light was collected by the same 15× objective. A variable knife-edge aperture located in the image plane was used to define the signal collection area and only that portion of the signal was directed to the MCT detector. Typical aperture sizes were $144\,\mu\mathrm{m}^2$ to $400\,\mu\mathrm{m}^2$. All NIR spectra were gathered as

$P_{sample}/P_{background}$, where P_{sample} is collected from an area with a single crystal was present, and $P_{background}$ was collected from an reflective adjacent area (the gold substrate) with no single crystal present.

Four-probe conductivity measurements were carried out on both compounds as a function of temperature. Pellets of (TTF)BiI_4 and $(TTF)_4BiI_6$ were pressed in a Carver press in a 10 mm×3 mm rectangular pellet die under 1.2 metric ton force. The dimensions of the pellets were roughly 10 mm×3 mm×1 mm. 60 nm gold contacts were deposited directly onto the surface of the pellets by thermal evaporation under high vacuum (10^{-7} mbar). The pellets were then loaded into a LakeShore cryogenic probe station and evacuated to a pressure of 10^{-4} mbar. Standard two-probe conductivity measurements were carried out at 300 K between the relevant four contacts, to access sample uniformity (details in the supporting information). The measured current was observed to be linearly proportional to the applied voltage and the average conductivity across the three regions was extracted to be $1.6(4)\times10^{-8}$ S cm^{-1} for (TTF)BiI_4 and and $1.05(3)\times10^{-4}$ S cm^{-1} for $(TTF)_4BiI_6$.

The conductivity was extracted by measuring the average differential resistance of the samples, between ±1 V using a Keithley 2400 SourceMeter. The devices all had a length of 150 μm and a width of 1.25 mm. The thickness of the (TTF)BiI_4 and $(TTF)_4BiI_6$ samples were 1.00 mm and 1.20 mm respectively.

Four-probe conductivity was then carried out between 300 K and 75 K using a Keithley 2400 SourceMeter and a Keithley 6220 Precision Current Source. Due to the substantial dependence of conductivity on temperature, the current range measured was varied as a function of temperature: ± 10 nA for (TTF)BiI$_4$ and $\pm 1\,\mu$A from 300 K to 105 K, and ± 100 nA from 100 K to 75 K for (TTF)$_4$BiI$_6$. The measured voltage was observed to be linearly proportional to the driving current for all measurements (data not shown). Below 185 K the conductivity of (TTF)BiI$_4$ was below measurable limits of the instrumentation.

3.3 Results and discussion

The panels of Figure 3.1 depict the structures of the TTF–Bi–I compounds solved from single crystal X-ray diffraction (crystallographic details in Table 3.1). All crystallographic representations were created using the VESTA software suite.[48] Figure 3.1(a) and (b) depict (TTF)BiI$_4$ projected down two different axes that allow the relative disposition of the TTF$^{+\bullet}$ dimer stacks and edge-shared [BiI$_2$I$_{4/2}$]$^-$ chains to be clearly distinguished. Such chains of [BiI$_2$I$_{4/2}$]$^-$ have been previously noted in the crystal structure of [BEDT-TTF]BiI$_4$.[74] It is interesting to note that the staggered TTF$^{+\bullet}$ dimer stacks are commensurate with the anionic Bi–I lattice. (TTF)BiI$_4$ is similar to the aforementioned

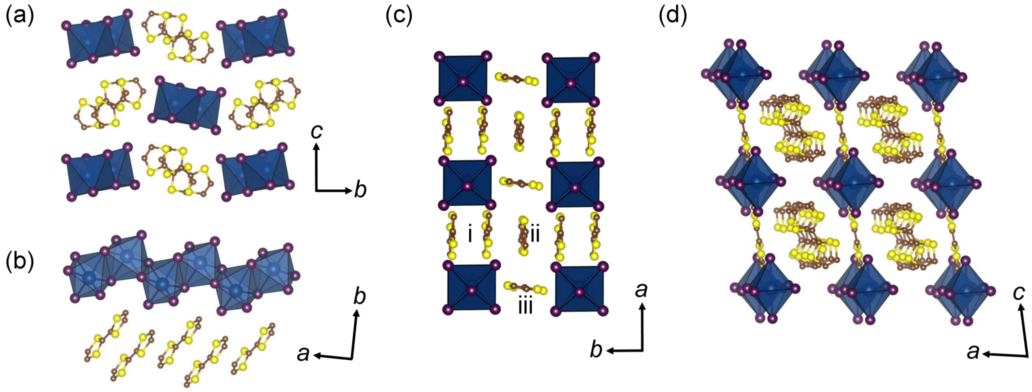

Figure 3.1: (a) The full structure of (TTF)BiI$_4$ looking down the a-axis, emphasizing the staggered stacks of TTF$^{+\bullet}$ dimers. (b) Alternate perspective of (TTF)BiI$_4$ looking down the c-axis, illustrating the commensurate stacking of TTF$^{+\bullet}$ dimers with edge sharing [BiI$_2$I$_{4/2}$]$^-$ chains. (c) Full crystal structure of (TTF)$_4$BiI$_6$ looking down the c-axis. This view emphasizes the mixed-valence TTF comprising alternating TTF$^{+\bullet}$ dimers (i) and neutral TTF (ii) stacked along the b-axis, as well as the alternating, isolated TTF$^{+\bullet}$ (iii) disposed normally to the a-axis. (d) Full Crystal structure of (TTF)$_4$BiI$_6$ looking down the b-axis, emphasizing the BiI$_6^{-3}$ octahedra and eclipsed nature of the mixed-valence TTF stack.

Table 3.1: Crystallographic Data for (TTF)BiI_4 and $(TTF)_4BiI_6$, 296 K

Empirical Formula	$C_6S_4H_4BiI_4$	$C_{24}S_{16}H_{16}BiI_6$
Crystal habit, color	Plate, red	Block, red
Crystal system	Monoclinic	Triclinic
Space group	Cc	$P\bar{1}$
Volume (Å^3)	3348.3(7)	1171.4(1)
a (Å)	7.6774(9)	10.237(8)
b (Å)	31.819(4)	10.460(5)
c (Å)	14.159(2)	11.166(8)
α (°)	90	84.28(1)
β (°)	104.535(2)	80.45(2)
γ (°)	90	85.85(3)
Z	8	1
ρ (g mol^{-1})	920.91	1787.71
Dens. (g cm^{-3})	3.654	2.534
Abs. (mm^{-1})	18.40	8.449
F_{000}	3192	817
Reflections (unique)	22352 (7334)	10557 (4839)
R_{int}	0.0365	0.1048
R_1	0.0357	0.0591
wR_R	0.0898	0.1347
∂F ($e\mathring{A}^{-3}$)	1.530 and -1.142	2.396 and -1.126
GOF	1.012	1.019

$(TTF)Pb_2I_5$[83] in that both are monovalent $TTF^{+\bullet}$ salts with staggered infinite dimer stacks. However, of these two compounds, $(TTF)BiI_4$ has decreased metal-iodide connectivity (1D rather than 2D). Additionally, we note that the structure was solved in the space group Cc, and not in the higher symmetry space group $C2c$ because the two fold symmetry of the latter was not compatible with the orientation of the $TTF^{+\bullet}$ packing motif.

Figure 3.1(c) and (d) display different views of the structure of $(TTF)_4BiI_6$ and illustrate the isolated BiI_6^{-3} octahedra and the unique TTF moieties: charged $TTF^{+\bullet}$ cations and neutral TTF [indicated in Figure 3.1(c)]. Crystallographically, neutral TTF is distinguished from $TTF^{+\bullet}$ by the shorter bond distances within and between the rings.[70] The ordered, mixed-valence TTF stacking in $(TTF)_4BiI_6$ is different to most other mixed-valence halide salts, where the TTF stacks are more disordered,[67, 69] and furthermore, the structure type of $(TTF)_4BiI_6$ is quite unique due to the isolated $TTF^{+\bullet}$ seen. It is uncommon to find discrete $TTF^{+\bullet}$, and to our knowledge is the only example of this type of $TTF^{+\bullet}$ packing. There are some similar structure types with TTF derivatives, such as $(BDT\text{-}TTP)_3I$[84] and $\alpha-(TTM\text{-}TTP)_2I_3$,[85] but these TTF derivatives pack in herringbone fashion, whereas in $(TTF)_4BiI_6$, the isolated $TTF^{+\bullet}$ stack perpendicular to neutral TTF, forming $TTF^{+\bullet}-TTF^0$ columns throughout the structure.

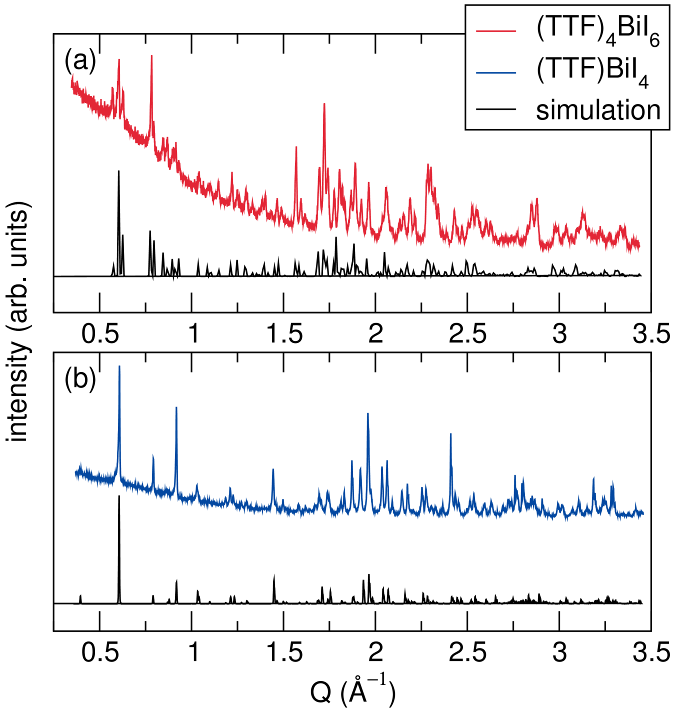

Figure 3.2: PXRD and simulated powder patterns of the compounds (a) $(TTF)_4BiI_6$ and (b) $(TTF)BiI_4$.

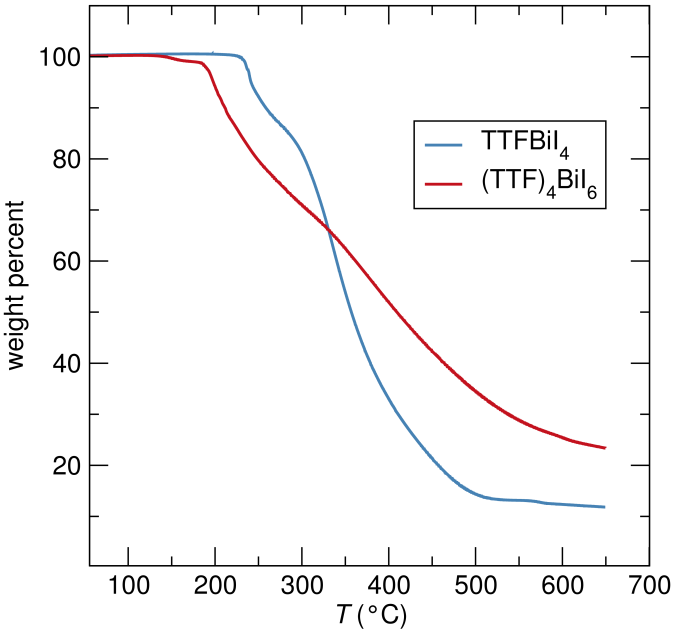

Figure 3.3: TGA data for the title compounds (TTF)BiI$_4$ and (TTF)$_4$BiI$_6$. The organic component (tetrathiafulvalene, TTF) is presumed to be the first part to degrade from (TTF)BiI$_4$ near 225°C and 141°C for (TTF)$_4$BiI$_6$.

Bulk purity of (TTF)BiI$_4$ and (TTF)$_4$BiI$_6$ was established via PXRD, with representative powder patterns displayed in Figure 3.2. Thermogravimetric analysis was conducted on these powders, and is displayed in Figure 3.3. The decomposition profiles of the two compounds are quite different, with (TTF)$_4$BiI$_6$ degrading close to 100 degrees before (TTF)BiI$_4$.

Figure 3.4 presents experimental and simulated electron spin resonance (ESR) spectra for polycrystalline solid state samples of (TTF)BiI$_4$ and (TTF)$_4$BiI$_6$,

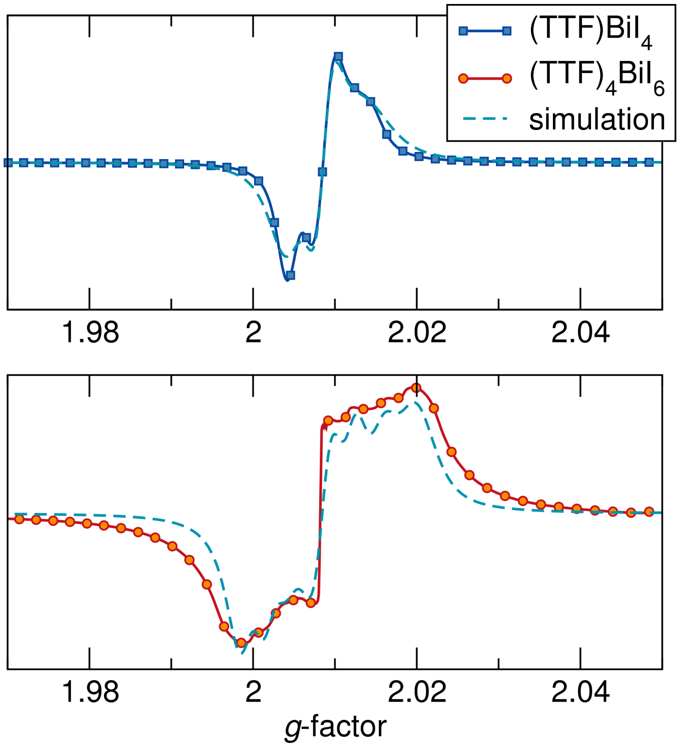

Figure 3.4: Solid-state room temperature ESR spectra of (a) (TTF)BiI$_4$ and (b) (TTF)$_4$BiI$_6$. Simulations for each are displayed as well. The g-values employed for the simulation of the spectrum for (TTF)BiI$_4$ were 2.0054, 2.0086, and 2.0111. Eight different g values: 2.0184, 2.0150, 2.0118, 2.00870, 2.0051, 2.047, 2.0010, and 1.9990 were required to simulate the spectrum of (TTF)$_4$BiI$_6$.

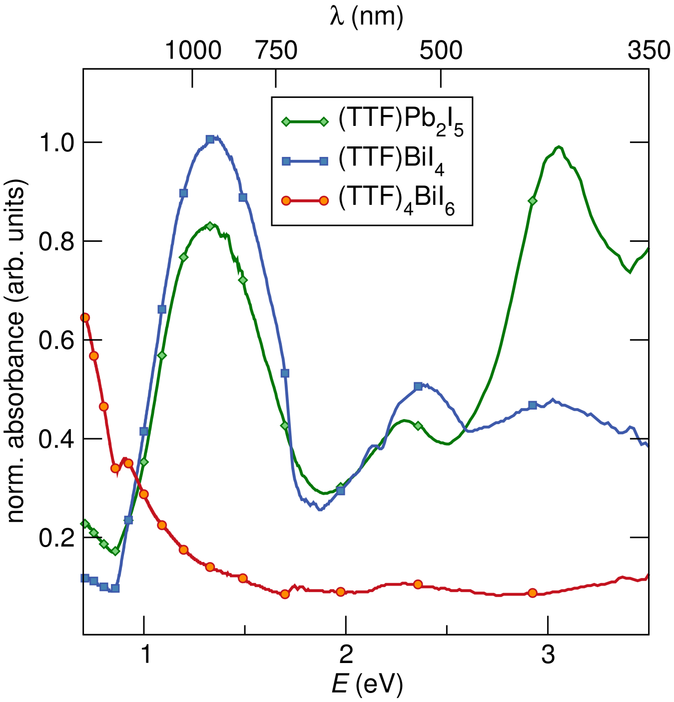

Figure 3.5: Normalized Kubelka-Munk transformed UV-Vis diffuse reflectance powder spectra of the compounds (TTF)BiI$_4$and (TTF)$_4$BiI$_6$. Data for (TTF)Pb$_2$I$_5$ are displayed for comparison.

confirming the presence of the radical cation speacies TTF$^{+\bullet}$ in both compounds. Simulations were carried out using the EasySpin[51] code. Figure 3.4(a) shows the relatively easily described (TTF)BiI$_4$ spectra, simulated with three g values centered at 2.0086. The simulated spectra of (TTF)$_4$BiI$_6$ on the other hand, required eight different g tensors, potentially corresponding to the three crystallographically distinct TTF$^{+\bullet}$ moieties found in the crystal structure.

Figure 3.5 displays the diffuse reflectance absorption spectra of the title com-

Table 3.2: Assignment of diffuse reflectance optical absorption data for $(TTF)BiI_4$ and $(TTF)_4BiI_6$, 296 K

E (eV)	Suggested transition	$(TTF)BiI_4$	$(TTF)_4BiI_6$
0.70	$TTF^{+\bullet} + TTF^0 \rightarrow TTF^0 + TTF^{+\bullet}$	medium	strong
1.50	$2\ TTF^{+\bullet} \rightarrow TTF^0 + TTF^{2+}$	strong	weak
2.30	$TTF^{+\bullet}$(dimer) → excited $TTF^{+\bullet}$(dimer)	medium	weak
3.10	$TTF^{+\bullet}$(dimer) → excited $TTF^{+\bullet}$(dimer)	medium	weak

pounds, as well as of the related material $(TTF)Pb_2I_5$, for comparison. Table 3.2 lists the observed peaks and previously attributed transitions.[69] The diffuse reflectance spectra show features seen in most $TTF^{+\bullet}$ salts, including absorptions peaking near 1.5 eV that has been attributed to intra-dimer charge transfer, ($2TTF^{+\bullet} \rightarrow TTF^{+2}$ + neutral TTF), as well as absorptions near 2.3 eV and 3.1 eV which correspond to molecular transitions of the $TTF^{+\bullet}$.[67, 69] The spectrum of $(TTF)BiI_4$ shows the strongest absorption at 1.5 eV and displays weaker absorptions at 2.3 eV, 3.0 eV, and 0.70 eV. When compared to the similarly structured $(TTF)Pb_2I_5$, this increased 1.5 eV absorption in $(TTF)BiI_4$ could be due to the decreased dimer-dimer eclipsing, which prevents long range charge transfer through the stack. The powder absorption spectra of both $(TTF)BiI_4$ and $(TTF)Pb_2I_5$ also show absorptions below an energy of 1.0 eV. Absorptions below an energy of 1.0 eV can be attributed to charge transfer between neutral TTF and $TTF^{+\bullet}$, and are primarily seen in spectra of mixed-valence TTF salts [*eg.* $(TTF)Br_{0.71}$, $(TTF)I_{0.71}$, $(TTF)SCN_{0.57}$] [67, 69] and not in the spectra of monovalent salts. For the $(TTF)Pb_2I_5$ material, these absorptions were attributed to back charge-transfer between the $TTF^{+\bullet}$ stacks and the inorganic networks. However, one explanation for these signatures is that in most monovalent salts the dimer pairs do not pack favorably for charge transfer (herringbone fashion). In $(TTF)Pb_2I_5$ and $(TTF)BiI_4$ dimers are packed parallel and close enough to $\pi - \pi$ stack, which should facilitate this sub 1 eV hopping transition throughout respective $TTF^{+\bullet}$ stacks. We believe this to be part of the story for why these absorptions are seen in diffuse reflectance spectra, but as we will show, other behavior in these monovalent salts suggests back-charge transfer between the metal iodide network and $TTF^{+\bullet}$ stacks. The powder optical absorbance spectrum of $(TTF)_4BiI_6$ is primarily absorption in the NIR due to the presence of free carriers in the material. These NIR absorptions dwarf the interdimer and molecular $TTF^{+\bullet}$ absorptions above 1.0 eV. Absorptions below an energy of 2.1 eV in the spectra displayed here are not associated with the inorganic network. This is because most bismuth iodide systems maintain a constant band gap near or greater than 2.1 eV, regardless of metal-iodide connectivity and structure. [65]

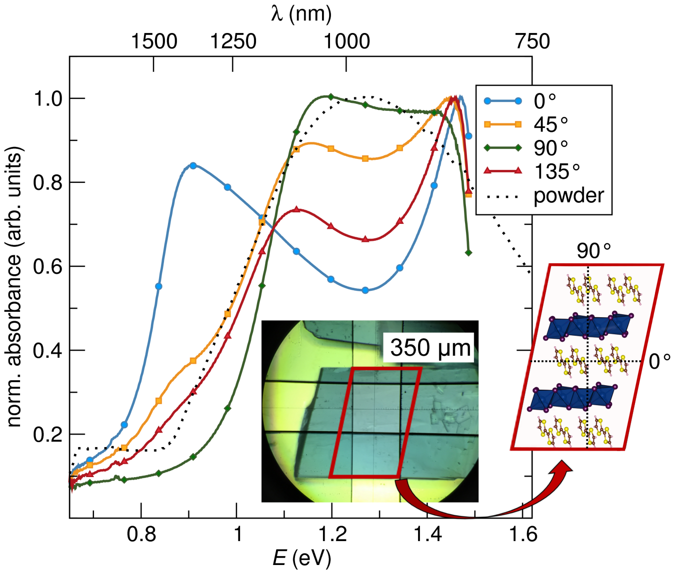

Figure 3.6: Kubelka-Munk transformed NIR reflectance spectra of $(\mathrm{TTF})\mathrm{BiI}_4$ single crystals as well as the powder diffuse reflectance UV-Vis spectrum of $(\mathrm{TTF})\mathrm{BiI}_4$ from Figure 3. Polarization at zero degrees is parallel to the horizontal axis (and $\mathrm{TTF}^{+\bullet}$ stacks), and ninety degrees is perpendicular to the horizontal axis (and $\mathrm{TTF}^{+\bullet}$ stacks). It is interesting to note that regardless of polarization the absorption at 1.5 eV remains constant, and that the absorptions at 1.15 eV and 0.85 eV vary in intensity based on polarization. The inset displays a microscope photograph of a representative $(\mathrm{TTF})\mathrm{BiI}_4$ single crystal, showing the well-developed (010) face, as well as a carton crystallographic depiction of the (010) face.

Table 3.3: Single crystal NIR optical data for (TTF)BiI$_4$, 296 K

E (eV)	Suggested transition	0°	90°
0.73	$\mathrm{TTF}^{+\bullet} + \mathrm{TTF}^0 \rightarrow \mathrm{TTF}^0 + \mathrm{TTF}^{+\bullet}$	weak	weak
0.85	$\mathrm{Bi\text{-}I}_m + \mathrm{TTF}^{+\bullet} \rightarrow \mathrm{Bi\text{-}I}_m + \mathrm{TTF}^0$	strong	absent
1.15	$\mathrm{Bi\text{-}I}_m + \mathrm{TTF}^{+\bullet} \rightarrow \mathrm{Bi\text{-}I}_m + \mathrm{TTF}^0$	strong	medium
1.50	$2\ \mathrm{TTF}^{+\bullet} \rightarrow \mathrm{TTF}^0 + \mathrm{TTF}^{2+}$	strong	strong

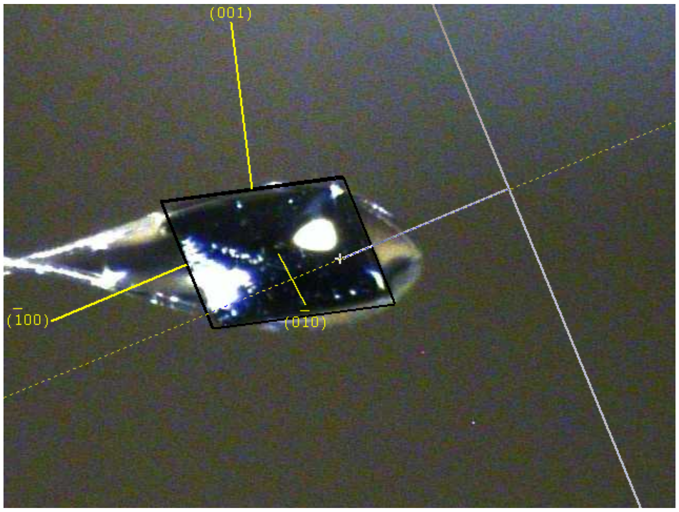

Figure 3.7: Photograph of a (TTF)BiI$_4$ single crystal. Growth planes were determined using APEX2 software.

Single crystal polarized light experiments have been performed prior with other TTF$^{+\bullet}$ containing salts as a way to isolate charge transfer absorptions parallel and perpendicular to TTF$^{+\bullet}$ containing stacks.[67, 69] It was our hope that this type of experiment could provide further information on potential charge transfer occurring between the inorganic and organic networks in (TTF)BiI_4. Figure 3.6 displays room temperature single crystal NIR reflectance spectra, transformed to absorbance, as well as the powder UV-Vis data for (TTF)BiI_4 over the same energy range. The spectra were taken at varying polarization angles between the energies 0.70 eV and 1.65 eV. Included is an inset photograph of a representative single crystal with the developed (010) face (looking down b-axis) that was used for the NIR experiment, and a crystallographic depiction of the (010) face. The 0° data is oriented parallel to the $\text{TTF}^{+\bullet}$ stacks and 90° is perpendicular to the $\text{TTF}^{+\bullet}$ stacks. The growth orientation was established with a single crystal x-ray diffractometer. Figure 3.7 displays a picture of a representative single crystal of (TTF)BiI_4, taken with the APEXII software.

Considering each polarized (TTF)BiI_4 NIR spectrum in Figure 3.6, it is noted that all spectra have absorptions that are dependent on the angle of incident light. This is expected (due to the anisotropic nature of the $\text{TTF}^{+\bullet}$ stacking), but the location and behavior of these absorptions is nontraditional for monovalent $\text{TTF}^{+\bullet}$ materials. In total, four absorption peaks are seen in all spectra with varying intensity, listed with proposed transitions in Table 3.3. The intensity of the peak at 1.5 eV is independent of polarization angle. In contrast, the intensity of the 1.15 eV and 0.85 eV peaks are angle dependent. The weak peak at 0.73 eV is seen with similar intensity regardless of polarization angle.

In NIR spectra of other monovalent $TTF^{+\bullet}$ salts, the intensity of the 1.5 eV peak can be reduced as light is made perpendicular to $TTF^{+\bullet}$ stacks.[69] As such, because the 1.5 eV absorption appears angle independent in the single crystal absorption spectra suggests two potential explainations. One, that different charge transfer processes are present between the $TTF^{+\bullet}$dimers in $(TTF)BiI_4$, leading us to believe that the inorganic-network is maintaining localized charge-transfer between dimers regardless of incident light polarization, or two, that there is partial overlap of the spectra at 1.5 eV. Aside from the absorptions at 1.5 eV however, the peaks at 1.15 eV and 0.85 eV, as well as the peak at 0.73 eV, are quite interesting because they are usually unseen in other monovalent salt spectra. $(TTF)BiI_4$ is a monovalent $TTF^{+\bullet}$ salt, and would be expected to show similar optical properties to salts like $(TTF)ClO_4$ or $(TTF)Br_{1.0}$, but because of these sub 1.0 eV absorptions, $(TTF)BiI_4$ has optical signatures similar to a mixed-valence salt like $(TTF)I_{0.71}$.[67] Specifically, the 90° polarization spectrum shows that when light is polarized perpendicular to the $TTF^{+\bullet}$ stacks and the $[BiI_2I_{4/2}]^-$ chains, that the absorptions are primarily at 1.5 eV and 1.15 eV. In the 0° spectrum, when light is polarized parallel to the $TTF^{+\bullet}$ stacks and the $[BiI_2I_{4/2}]^-$ chains, there are absorptions primarily at 1.5 eV and 0.85 eV. The absorptions seen at 1.15 eV and 0.85 eV are hard to definitively attribute to specific transitions as they are not seen in other monovalent TTF$^{+\bullet}$ salts, but it is our assumption that they are related to two different pathways for a synergistic back charge-transfer transition related to the Bi-I network.

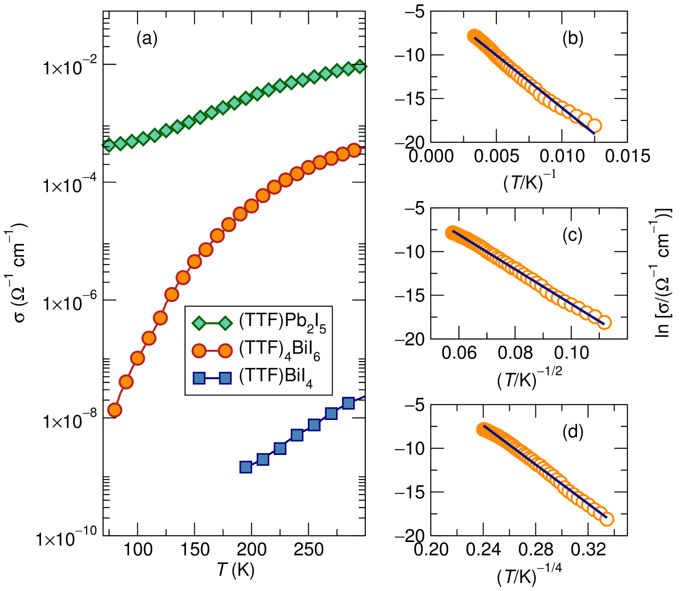

Figure 3.8: (a) Four probe conductivity measurements on pressed pellet samples of (TTF)BiI$_4$, (TTF)$_4$BiI$_6$, and (TTF)Pb$_2$I$_5$ (for comparison) plotted as conductivity (Ω^{-1} cm^{-1}) versus temperature. There was no detectable conductivity of (TTF)BiI$_4$ below $T = 185$ K. Activation energy fits for the conductivity data of (TTF)$_4$BiI$_6$ are shown in (b),(c), and (d) using Arrhenius, 1-dimensional, and 3-dimensional variable-range hopping fits, respectively. A description of the measurement as well as plots of the conductivity versus inverse temperature are included in the Supporting Information.

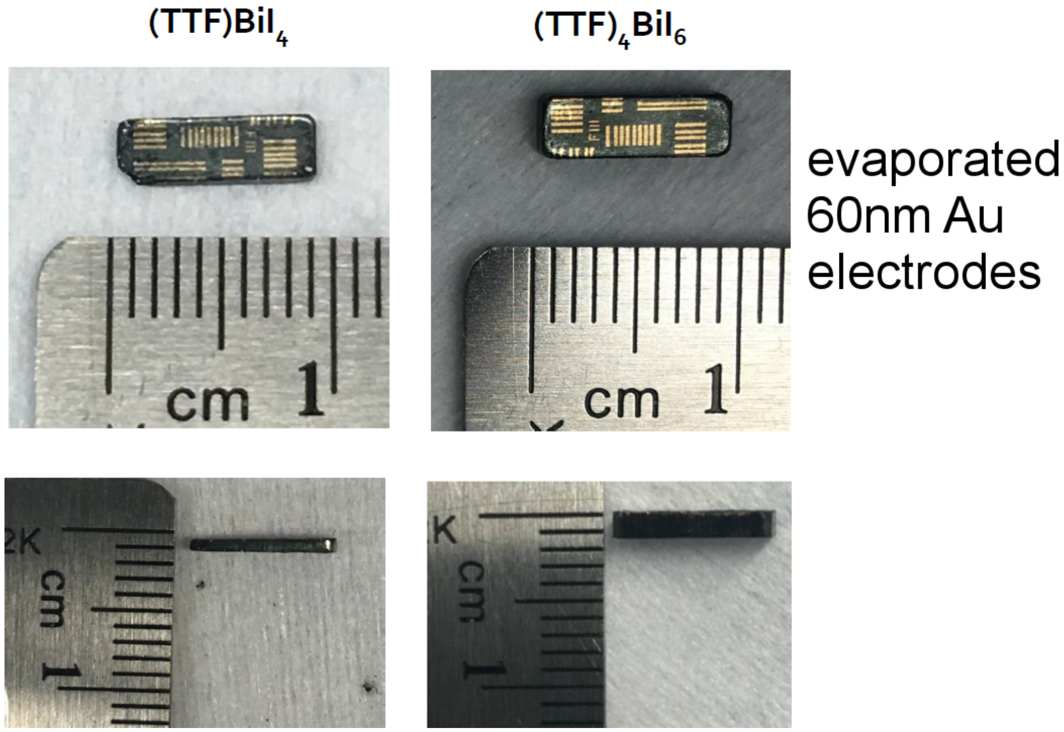

Figure 3.9: Pictures of the pressed pellets of (TTF)BiI_4 and $(TTF)_4BiI_6$ used in the 4-probe conductivity measurements.

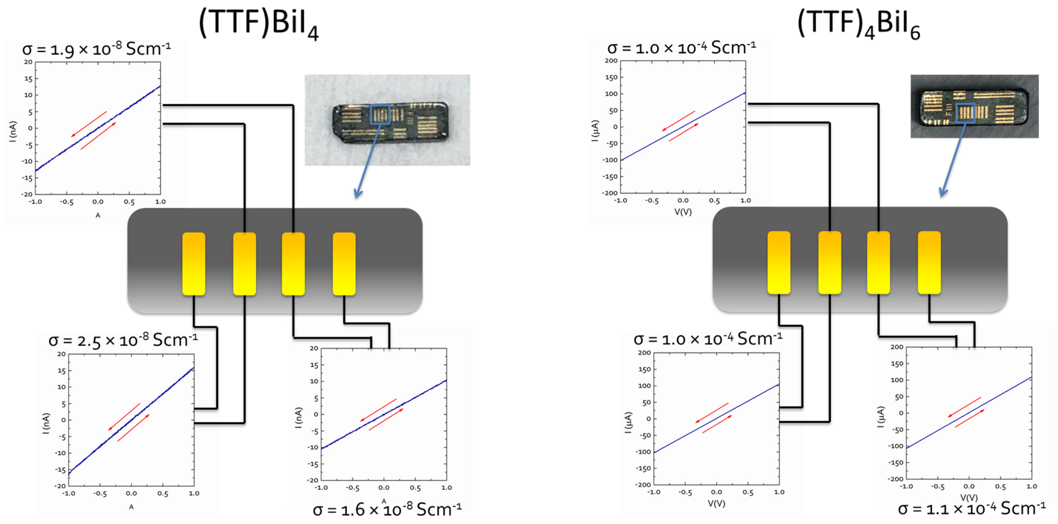

Figure 3.10: Photo of the pressed pellets of (TTF)BiI$_4$ and (TTF)$_4$BiI$_6$ that were tested, in addition to cartoon depictions of the four evaporated gold contacts used. Two probe measurements between the three near neighbor pair gold contacts are also included, verifying the consistency of four probe measurements.

Figure 3.8(a) displays the temperature-dependence of the four-probe electrical conductivity σ on pressed pellets of (TTF)BiI$_4$ and (TTF)$_4$BiI$_6$ as a function of temperature. For reference, data for the previously reported compound (TTF)Pb$_2$I$_5$[83] are also displayed. Figures 3.9 and 3.10 display pictures of the measured pellets, and 2-probe conductivity experiments done to verify the consistency of the four-probe data, respectively. Neither of the samples from this study are as conductive as (TTF)Pb$_2$I$_5$. (TTF)BiI$_4$ is a significantly poorer electrical conductor than (TTF)$_4$BiI$_6$; by about 185 K, the DC conductivity of (TTF)BiI$_4$

is too low to be measured reliably. $(TTF)_4BiI_6$ in contrast, has an electrical conductivity that is close to $10^{-4}\,\Omega^{-1}\,\mathrm{cm}^{-1}$ at 300 K. By 80 K, the value of the conductivity of $(TTF)_4BiI_6$ has decreased by four orders of magnitude. Attempts to fit the temperature-dependence to activated behavior [Figure 3.8(b)] throughout the measured temperature range proved unsatisfactory. Attempts were also made to fit the data to models of variable range hopping (VRH) following the formulation of Mott[86]: $\sigma = \sigma_0 \exp[-(T_0/T)^{\nu}]$. As seen from Figures 3.8(c) and (d), the choice of $\nu = 1/2$ appears to best fit the data, in contrast to $\nu = 1/4$, which is the more typical expectation for 3D VRH.[87] The exponent $\nu = 1/2$ could be indicative of VRH in 1D, *ie.* along the mixed-valence stack of TTF along the b crystallographic direction. An alternate explanation would involve Coulomb correlations, which are also consistent with the nature of the radical species in the TTF stacks.[86]

In the compounds described above, there are several contributors to the electrical conductivity, including the connectivity of the inorganic moieties and the nature (radical cation or neutral) and stacking of the TTF species. For the two Bi-based compounds reported here, we would expect from considerations of mixed-valence of the TTF, that $(TTF)_4BiI_6$ would have the high conductivity[88] as is indeed seen. From considerations of extended connectivity of the inorganic Bi–I framework, $(TTF)BiI_4$ could potentially be a good conductor, or at least, a good semiconductor, but that is not borne out by the measurements. Perhaps the most surprising aspect is that the previously studied (TTF)Pb_2I_5 is so much the better conductor of all three materials considered. While (TTF)Pb_2I_5 has extended inorganic connectivity (like (TTF)BiI_4), it does not have mixed-valence stacks displayed in the structure of $(TTF)_4BiI_6$. From an electronic standpoint, (TTF)Pb_2I_5 most resembles (TTF)BiI_4, so the large differences in the electrical transport behavior are at first sight somewhat puzzling. A potential explanation, made originally to describe the properties of (TTF)Pb_2I_5, is that the inorganic and organic components function synergistically to give rise to the observed properties, and perhaps that is not as much the case for these Bi–I compounds.

In conclusion, we have prepared and characterized two tetrathiafulvalene hybrid compounds with bismuth-iodide anion networks: (TTF)BiI_4 and $(TTF)_4BiI_6$. Both compounds are semiconductors with properties that appear to be influenced by the degree of bismuth-iodide connectivity, and by the packing and valence state of the TTF species. The optical properties of (TTF)BiI_4 suggest synergistic back charge-transfer similar to (TTF)Pb_2I_5,[83] but due to the decreased metal-iodide connectivity and the nature of the eclipsing dimers, the long range effect of the back charge-transfer is greatly reduced. This explains why the electrical conductivity is significantly decreased; (TTF)BiI_4 has bulk material conductivity comparable to related monovalent salts. The compound $(TTF)_4BiI_6$ has a unique mixed-valence crystal structure comprising an isolated $TTF^{+\bullet}$ as well as mixed-valence TTF stacks, interspersed with discrete BiI_6^{-3} anions. Because of the mixed-valence TTF stacks, and despite the isolated BiI_6^{-3} anions, this compound is the significantly better electrical conductor.

Chapter 4

Hydrogen bonding controls structural evolution in perovskite-related hybrid platinum (IV) iodides

In this chapter we describe a solid-state structural evolution in four hybrid hexaiodoplatinate(IV) compounds, demonstrating the increasingly important role that extended hydrogen bonding plays in directing the structure

---

[1] Doug H. Fabini, Jessie L. Andrews, Molleigh B. Preefer, Mitchel Koerner, Guang Wu, Fred Wudl, Anthony K. Cheetham, and Ram Seshadri have contributed to the contents of this chapter.

across the series. The compounds are A_2PtI_6, where A is one of the following amines: ammonium, NH_4^+; methylammonium MA, $CH_3NH_3^+$; formamidinium FA, $CH(NH_2)_2^+$; and guanidinium GUA, $C(NH_2)_3^+$, and are closely related in structure and properties to the hybrid halide perovskites of Pb(II). The first three of these compounds crystallize in the vacancy-ordered double perovskite $A_2Pt\square I_6$ ($\square$ indicates a vacant site) structure in the K_2PtCl_6 archetype, despite the relatively large perovskite tolerance factors involved. The last compound, $(GUA)_2PtI_6$ crystallizes in a vacancy-ordered variant of the hexagonal $CsNiCl_3$ structure: the K_2MnF_6 structure. A combination of ^{195}Pt and ^1H solid-state NMR spectroscopy and detailed density functional theory calculations help to reveal structural trends and establish the hydrogen-bonding tendencies. The calculations and measured optical properties support the surprising observation in these iodosalt compounds that for smaller A cations, the conduction bands are considerably disperse, despite lacking extended I–Pt–I connectivity.

Previous publication of this data can be found in *Inorganic Chemistry*, © 2018 American Chemical Society, reprinted with permission.

Evans, H. A.; Fabini, D. H.; Andrews, J. L.; Koerner, M.; Preefer, M. B.; Wu, G.; Wudl, F.; Cheetham, A. K.; Seshadri, R. Hydrogen bonding controls structural evolution in perovskite-related hybrid platinum (IV) iodides, *In-*

org. Chem. **2018**, *57*, 10375–10382

4.1 Introduction

The *AMX*$_3$ perovskite crystal structure is unique in that it is the simplest and only ternary structure type that has near-180° extended *M*–*X*–*M* interactions in all three dimensions. The extended interactions result in the disperse bands that can enable a host of interesting functional properties in perovskites. Halide perovskites with the formula *AMX*$_3$, where *A* is an alkali metal or small organic cation, *M* is a divalent main group metal, and *X* are halides are one such materials family combining impressive optoelectronic properties with remarkable ease of preparation.[8, 89–91] Thin film, single junction photovoltaic devices of these perovskite materials have exhibited upwards of 22 % power conversion efficiency (PCE), owing to a direct band gap electronic structure, inherently long lived charge carriers, and high defect tolerance of the perovskite active material.[9]

Halide perovskites, like their oxide counterparts, are a diverse class of materials that can tolerate many different kinds of chemical substitutions.[92, 93] This includes *A*-site substitution by different ions to obtain layered variants.[94, 95] The substitution of divalent *M* by a trivalent ion such as Bi(III) can result in a vacancy-ordered perovskite such as $K_3Bi_2\square I_9$ where every third *M* is missing, indicated by a vacancy $\square$.[65] Forking the charge on the divalent *M*-site through substitution with mono- and trivalent cations results in double-perovskites or elpasolites[96–100]. Finally, substitution on the *M* site with a tetravalent ion creates vacancy-ordered perovskites where *M* atoms and vacancies $\square$ (usually) display 3D rock-salt like ordering. The aristotype for this structure type is K_2PtCl_6 in the $Fm\bar{3}m$ space group.[101] It is interesting to note that *M*-site vacancy-ordered perovskites are rare or non-existent in the oxide perovskite world, even when permitted by the perovskite tolerance factor (for example, the hypothetical compound $La_2W\square O_6$), as a consequence of the cost of oxide-oxide repulsions and of stabilizing high cation charge states in isolated species.

Halide compounds with the K_2PtCl_6 composition have been known for a long time. They have been examined as diamagnetic hosts (A_2PtI_6) of paramagnetic ions (Ir^{4+}, Re^{4+}, Os^{4+}),[102] and have been studied for their interesting lattice dynamics associated with free rotation of isolated MX_6 octahedra.[103] A comprehensive review by Armstrong on A_2MX_6 materials (A = NH_4, K, Rb, Cs, M= Pt, Ir, Os, Re, W, and X = Cl, Br, I) provides an overview.[102] The structure type is also associated with charge disproportionation of the *M* site metal, as seen for Cs_2SbCl_6, which displays mixed-valence Sb(III) and Sb(V) atoms instead of what would appear to be Sb(IV).[104] Hybrid $A_2M\mathrm{Cl}_6$ and $A_2M\mathrm{Br}_6$ compounds were previously studied for how organic cations, predominantly methylammonium in $(\mathrm{MA})_2MX_6$ compounds (M= Sn, Pt, Te and X = Cl, Br, I)[105–109] or dimethylammonium in $(\mathrm{DMA})_2MX_6$ compounds (M= Sn, Pt, Te, Se and X = Cl, Br),[110–112] impact structural phase transitions through molecular reorientation.

The 2014 demonstration that the molecular iodostannate salt $\mathrm{Cs_2SnI_6}$ is an effective hole conductor — despite not possessing extended I–Sn–I connectivity — that can be employed as the hole-transport layer in dye-sensitized solar cells has been an important landmark in the way in which these materials are viewed.[24] Related work that has appeared includes a study of the role of defects in determining the properties of $\mathrm{Cs_2SnI_6}$ and $\mathrm{Cs_2TeI_6}$[26] and of the role of anharmonicity in dictating the properties of $A_2\mathrm{SnI}_6$ when A = $\mathrm{CH_3NH_3}$ or $\mathrm{CH(NH_2)_2}$.[113]

In this chapter, we discuss a series of compounds $A_2\mathrm{PtI}_6$ series [A = ammonium ($\mathrm{NH_4^+}$), methylammonium [$\mathrm{CH_3NH_3^+}$ abbreviated MA], formamidinium [$\mathrm{CH(NH_2)_2^+}$ abbreviated FA], and guanidinium [$\mathrm{C(NH_2)_3^+}$ abbreviated (GUA)]. The synthesis and composition of several $A_2\mathrm{PtI}_6$ compounds were already reported by Datta in 1913,[114] albeit with no descriptions of the structure. Furthermore, Datta refers back to some literature on these from the first half of the 19th century. The crystal structures of A_2PtI_6 at room temperature for A = NH_4[115, 116] and MA[105] have been previously reported. We demonstrate that hydrogen bonding becomes especially important in retaining the vacancy-ordered perovskite in the compounds with the larger *A* cations. Specifically, if the organic cation is small, I–I van der Waals interactions guide atomic packing, and if the organic cation is large, hydrogen bonding forces (N–H$\cdots$I) guide the structure. Consequences of the hydrogen bonding tendencies manifest in solid-state ^{1}H NMR experiments and in density functional theory (DFT) based electronic structure calculations. Just as in the case of Cs_2SnI_6,[24] we find that for the smaller *A* cations, the conduction bands of A_2PtI_6 display surprisingly disperse electronic bands. The measured optical properties are compared with the results of DFT calculations.

4.2 Experimental methods

The starting material CH_3NH_3I (MAI) was prepared by adding a solution of CH_3NH_2 (1.00 eq. 33% wt/wt in absolute ethanol, Spectrum) solution of HI (1.05 eq., 57% wt/wt in aqueous solution, Spectrum) held at 0 °C. After stirring for 2 h at 0 °C, excess solvent was removed using a rotary evaporator. The precipitate was recrystallized twice from a hot ethanol/water mixture, washed with ether, and dried under vacuum overnight to give white crystals with a plate-like habit.

$CH(NH_2)_2I$, FAI was prepared by metathesis, by adding solid formamidinium acetate (1.00 eq, 99%, Sigma-Aldrich) to room temperature HI (2.0 eq., 57% wt/wt in aqueous solution, Spectrum.) After stirring for 2 h, excess solvent was removed using a rotary evaporator. The residue was washed with boiling toluene to remove any potential triazine contaminant, recrystallized from ethanol, vacuum filtered, and dried to give white crystals with a needle-like habit.

$(NH_4)_2PtI_6$ was prepared by combining 46.0 mg NH_4I (0.300 mmol, Sigma Aldrich, 99.5%) and 40.0 mg (0.150 mmol) $PtCl_2$ (Strem, 99.9%) in 6.0 g 57% wt/wt HI, which was brought to gentle reflux for 15 min. The solution was slowly cooled to room temperature and placed in a refrigerator overnight. The solution was vacuum filtered cold and washed with diethyl ether. The isolated crystals were vacuum-dried overnight. Small, dark-bronze cubic habit crystals were isolated. The hydroiodic acid used for this and all other iodoplatinate reactions did not contain the reducing stabilizer hypophosphorous acid. The iodine contained in solution (due to not using the reducing stabilizer) is thought to be responsible for the oxidation of Pt^{2+} to Pt^{4+}.

$(MA)_2PtI_6$ was prepared by combining 71.7 mg MAI (0.451 mmol) to 58.9 mg (0.225 mmol) $PtCl_2$ (Strem, 99.9%,) in 15.5 g 57% wt/wt hydroiodic acid. This solution was brought to gentle reflux for 25 min., slowly cooled to room temperature, and placed in freezer overnight. This solution was vacuum filtered cold and washed with diethyl ether. Isolated crystals were vacuum-dried overnight. Dark-bronze colored, hexagonal plate habit crystals were isolated.

$(FA)_2PtI_6$ was prepared by combining 130 mg (0.760 mmol) $CH(NH_2)_2I$ with 100 mg (0.375 mmol) of $PtCl_2$ (Strem, 99.9%) in 15.5 g of 57% wt/wt hydroiodic acid. This solution was brought to a temperature no greater than 70°C, and stirred for 25 min. The solution was slowly cooled to room temperature (no precipitate forms at this point) and placed in a freezer overnight. Bronze, metallic-looking needles of $(FA)_2PtI_6$ were vacuum filtered cold, washed with diethyl ether, and vacuum dried overnight. Exceeding 70°C results in degradation of the FA cation, producing free ammonium.

$(GUA)_2PtI_6$ was prepared by combining 282 mg $C(NH_2)_3I$ (1.5 mmol (Sigma Aldrich) and 200 mg (0.75 mmol) $PtCl_2$ (Strem, 99.9%,) in 15.5 g 57% wt/wt hydroiodic acid. The solution temperature was raised to gentle reflux for 25 min., slowly cooled to room temperature, and placed overnight in a freezer. This solution was vacuum-filtered cold and washed with diethyl ether. The isolated crystals were vacuum-dried overnight. Large, dark grey, block habit crystals were isolated. We note that if a more concentrated reaction mixture is employed, an unidentified Pt-containing contaminant co-forms with the desired compound. Careful control of concentration allows the pure compound to be obtained.

Single crystal X-ray diffraction data was collected on a Bruker KAPPA APEX II diffractometer equipped with an APEX II CCD detector using a TRIUMPH monochromator with a Mo Kα X-ray source (λ = 0.71073 Å). The crystals were mounted on a cryoloop under Paratone-N oil and kept under nitrogen. Absorption correction of the data was carried out using the multiscan method as implemented in SADABS.[46] Subsequent calculations were carried out using SHELXTL.[47] Structure determination was done using intrinsic methods. All hydrogen atom positions were omitted. Structure solution, refinement, and creation of publication data was performed using SHELXTL. Crystal structures were visualized using the VESTA software suite.[48]

Powder X-ray diffraction was performed on a Panalytical Empyrean Powder Diffractometer (Bragg-Brentano HD module, no monochromator) equipped with a Cu source λ = 1.5418 Å. Rietveld refinements were performed in the TOPAS software suite.[117]

Solid state NMR: ^{1}H and ^{195}Pt single-pulse experiments, ^{1}H inversion recovery experiments, and ^{14}N spin echo experiments were conducted on a 500 MHz (11.7 T) Bruker Avance NMR spectrometer with a Bruker 4 mm H/X/Y triple resonance MAS probe. Powdered samples were packed into a 4 mm zirconia MAS rotor and capped with a Kel-F drive cap. ^{1}H chemical shift was referenced to adamantane (1.71 ppm relative to TMS at 0 ppm). ^{195}Pt chemical shift was referenced to a 1 M solution of Na_2PtCl_6 in D_2O (0 ppm). Longitudinal relaxation (T_1) experiments utilized the inversion recovery method. CSA parameters for ^{195}Pt were extracted using the SOLA line shape analysis module within Bruker Topspin.

Solid state UV-Vis spectra were obtained using an integrating sphere equipped Shimadzu UV3600 UV-NIR Spectrometer in diffuse reflectance mode. The A_2PtI_6 compounds tested were suspended in $BaSO_4$ medium (*via* grinding). The reflectance spectra were Kubelka-Munk transformed for relative absorbance spectra.

Thermogravimetric analysis (TGA) on all compounds was conducted using a TA Instruments Discovery instrument. A rate of 25 cm^3/min dry nitrogen purge was employed with a temperature ramp rate of 10°C/min. The maximum temperature of the experiment was 900°C.

Differential scanning calorimetry (DSC) measurements were performed using a TA Q2000 calorimeter. Samples (2 mg to 10 mg each) were hermetically sealed inside TZero aluminum pans. Samples were first cooled to -150°C, then heated to most 180°C at 10 °C/min. This was repeated for three cycles.

Ab initio calculations of the crystal structures, electronic structures, and optical properties were performed with the Vienna *Ab initio* Simulation Package (VASP)[52–55] which implements the Kohn-Sham formulation of density functional theory (DFT) using a plane wave basis set in conjunction with projector augmented waves.[56, 57] The generalized gradient approximation was employed using the exchange and correlation functional of Perdew, Burke, and Ernzerhof (GGA-PBE).[60] The plane wave basis set cutoff energy (800 eV) and k-point mesh density (≈1500 k-points per reciprocal atom for convergence of the charge density, ≈40,000 k-points *per* reciprocal atom for computing the density of states and dielectric function, all Γ-centered Monkhorst-Pack sampling[118] were chosen based on convergence of the total energy.) Structure relaxations were performed, including van der Waals corrections (DFT-D3 method of Grimme),[119] to a force tolerance of 4 meV Å^{-1}. All relaxed structures preserved the original space group symmetry, with the exception of $(\text{MA})_2\text{PtI}_6$, which appeared to drift slightly from the original $R\bar{3}m$ high symmetry space group symmetry, but that was found within a 0.001 Å lattice parameter tolerance using the FINDSYM program[120] to actually retain $R\bar{3}m$. This symmetrized cell was used for subsequent calculations to minimize computational expense. Brillouin zone paths for band structure calculations were taken from Setyawan and Curtarolo.[121] Frequency-dependent dielectric functions were calculated using the method described by Gajdoš *et al.*, as implemented in VASP.[122] The dielectric tensors were converted to isotropic equivalents, and subsequently to isotropic absorption coefficients via custom python code. Band structures and densities of states, including orbital projections, were visualized using custom python code.

4.3 Results and discussion

All the samples were prepared by standard methods (precipitation from acid) and their structures solved by single crystal X-ray diffraction; details of the methods employed are provided in the Experimental section above, with pertinent crystallographic data provided in Tables 4.1 and 4.2.

Figure 4.1(a) displays the 300 K structure of $(NH_4)_2PtI_6$ which crystallizes in the space group $Fm\bar{3}m$ and is isostructural to the VDHP K_2PtCl_6. In this structure, Pt and I are found on face-centered cubic lattices with ammonium cations in tetrahedral cavities.[123, 124] Figure 1(b) presents the 100 K structure, space group $P4/mnc$. At low temperature $(NH_4)_2PtI_6$ distorts similar to other per-

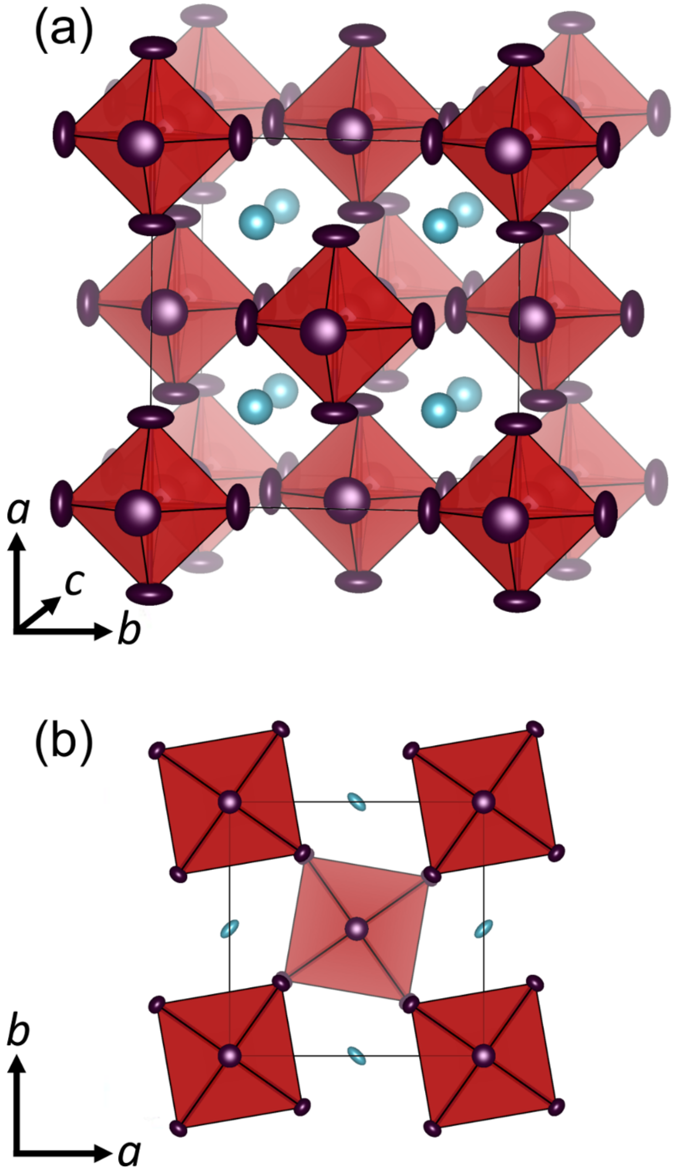

Figure 4.1: Crystal structure of $(NH_4)_2PtI_6$ with displacement ellipsoids (95% probability). (a) 300 K structure, viewed along c-axis, (b) 100 K structure, viewed along the c-axis to emphasize octahedral titling.

ovskites with an in phase octahedral rotation parallel to the c-axis, described by Glazer tilting nomenclature as a $a^0a^0c^+$ distortion.[125]

Figure 4.2 illustrates the 300 K structure of $(MA)_2PtI_6$, space group $R\bar{3}m$. We observe no first-order phase transition between 100 K and 480 K, though a second-order phase transition has previously been suggested at 134 K.[105, 109] The platinum ions in $(MA)_2PtI_6$ are found on Wyckoff site $3a$ with site symmetry $\bar{3}m$, and iodide ions are found on Wyckoff site $18h$ with site symmetry $.m$. The methylammonium cations are modeled here as static molecules aligned parallel to the *c*-axis.

Figure 4.3 depicts the high temperature (340 K and warmer) and low temperature (340 K to 100 K) structures of $(FA)_2PtI_6$. Some of the authors previously reported a compound of this empirical formula as isostructural to K_2PtI_6, but upon NMR analysis concluded this was incorrect. It was found that formamidinium ions degraded in solution (if the reaction temperature was brought above 70°C), yielding free NH_4^+ cations, which precipitate from solution in the form of $(NH_4)_2PtI_6$. If the solution is kept above 70°C for 20 minutes, $(NH_4)_2PtI_6$ is produced essentially pure. An erratum was submitted for the previous report.[126]

Figure 4.3(a) illustrates the high temperature phase of formamidinium plat-

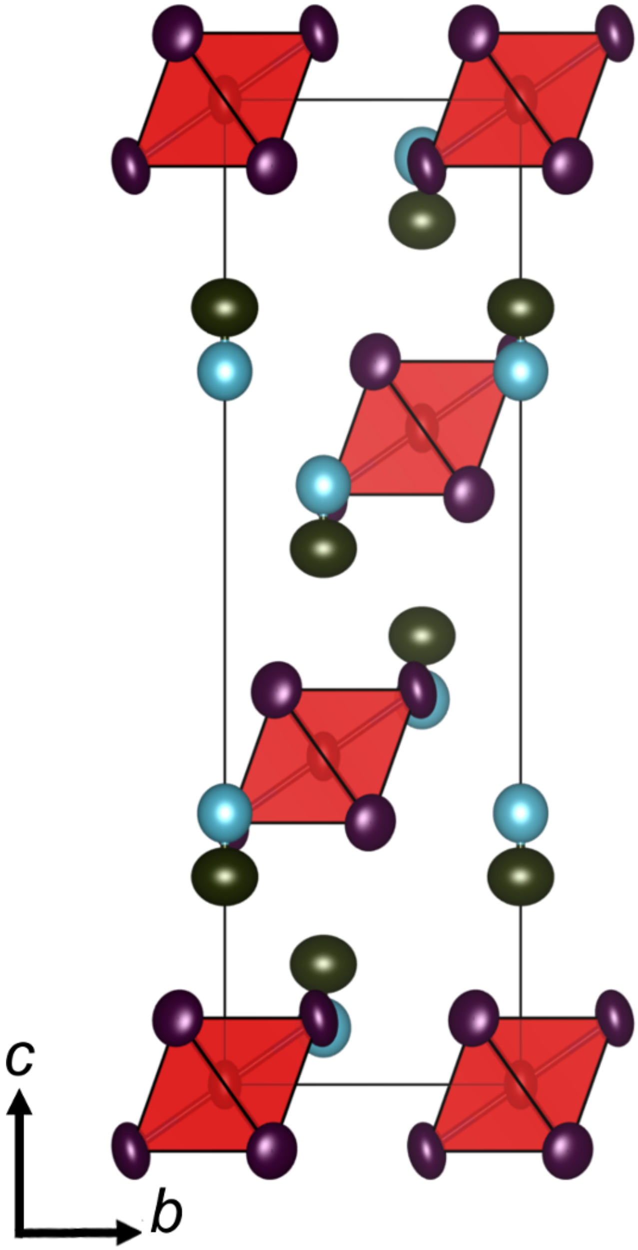

Figure 4.2: Crystal structure of $(MA)_2PtI_6$ at 300 K, with displacement ellipsoids (95% probability), viewed down along a-axis.

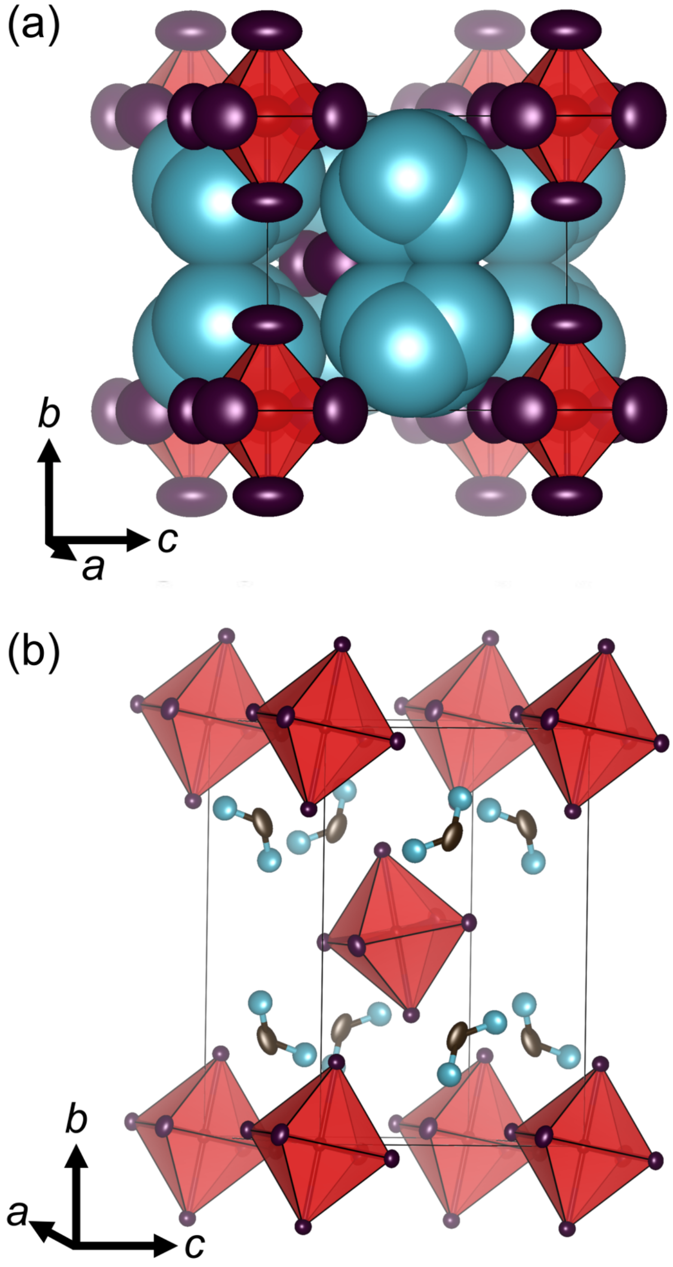

Figure 4.3: Crystal structure of $(\mathrm{FA})_2\mathrm{PtI}_6$ with displacement ellipsoids (95% probability). (a) 340 K, viewed along a-axis. (b) 100 K and below, viewed down a-axis.

inium iodide, space group $I4/m$, viewed along the a-axis, depicting $[PtI_6]^{2-}$ octahedra and disordered formamidiniums. Platinum ions are found on Wyckoff site $2a$ with site symmetry $4/m..$, with two independent iodides residing on the $8h$ and $4e$ Wyckoff sites, site symmetry $m..$ and $4..$, respectively. Formamidinium cations are modeled as distorted tetrahedra. Figure 4.3(b) displays the low temperature structure of formamidinium platinum iodide, space group $P2_1/n$, illustrating canted octahedra and ordered formamidinium cations. The structure contains platinum ions on Wyckoff position $2a$ with site symmetry $\bar{1}$, and 3 independent iodide ions as well as formamidinium C and N atoms located on general positions $4e$. There are currently few reported formamidinium-containing VHDPs, but there are compounds that contain organic cations such as dimethylammonium which crystallize with similar structural motifs.[127, 128]

Figure 4.4 displays the stable structure (between 100 K and 423 K) of $(GUA)_2PtI_6$, space group $P6_3mc$, viewed along the a-axis. Platinum ions are found on Wyckoff position $2b$ with site symmetry $3m.$ and iodide ions and carbon atoms are found on $6c$ positions, site symmetry $.m.$. There are two crystallographically distinct guanidinium cations within the unit cell of the compound, both of which are modeled here without disorder. The inorganic lattice is comprised of planes of similarly tilted $[PtI_6]^{2-}$ octahedra which alternate along the c-axis. $(GUA)_2PtI_6$ is similar to past reported guanidinium chloro- and

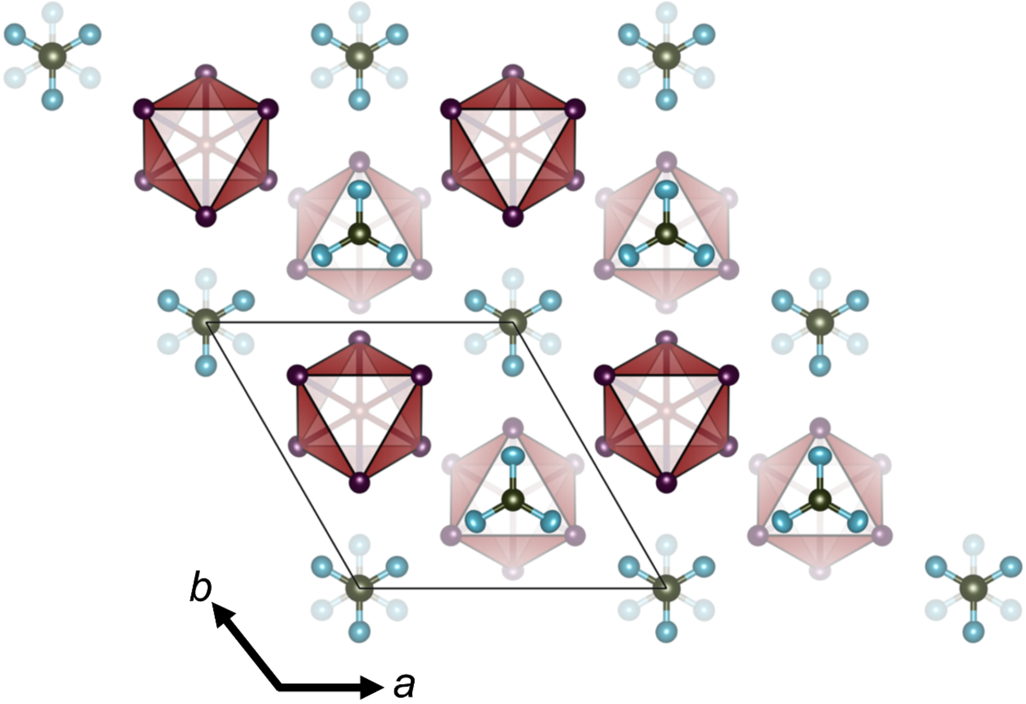

Figure 4.4: Crystal structure of $(GUA)_2PtI_6$ at 100 K, viewed along the c-axis, with displacement ellipsoids (95% probability).

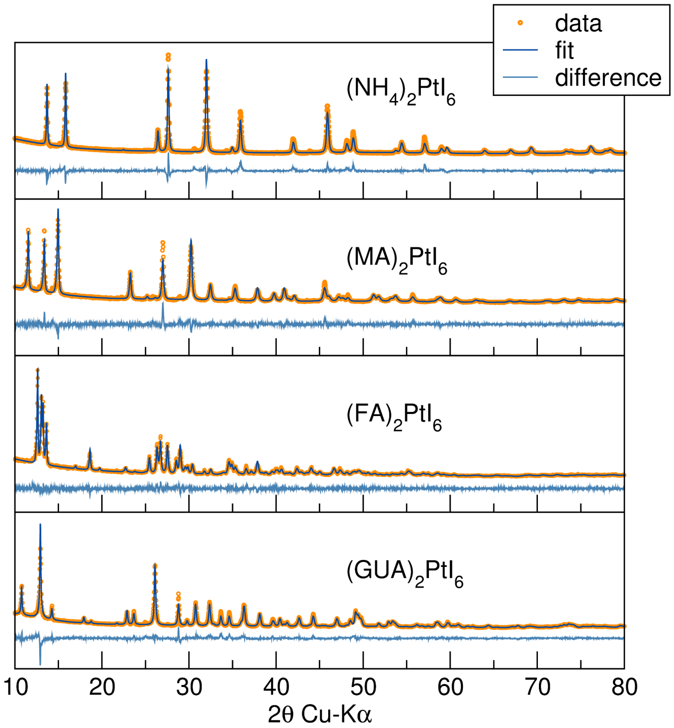

Figure 4.5: Rietveld refinements of the A_2PtI_6 compounds.

bromometallate structures, though those reported consistently crystallize in the centrosymmetric space group, $C2/m$.[129].

All compounds could be prepared as pure powders as confirmed by Rietveld refinement of powder X-ray diffraction data (without atomic occupancy) using room temperature single crystal diffraction as the structural comparison (Figure 4.5). The refinements indicate that the each bulk sample has unit cell parameters close to single crystal diffraction dimensions (Table 4.3 refined data, Tables 4.1 and 4.2 for single crystal data).

Table 4.1: Crystallographic Data for $(NH_4)_2PtI_6$ and $(MA)_2PtI_6$

Empirical Formula	$(NH_4)_2PtI_6$		$(CH_3NH_3)_2PtI_6$
Crystal habit, color	cubic, bronze		hexagonal, bronze
Crystal system	cubic	tetragonal	trigonal
Space group (#)	$Fm\bar{3}m$ (225)	$P4/mnc$ (128)	$R\bar{3}m$ (136)
Volume (Å^3)	1397(1)	681.6(1)	1250.5(2)
T (K)	290	100	273
a (Å)	11.179(4)	7.6446(5)	7.943(5)
b (Å)	11.179(4)	7.6446(5)	7.943(5)
c (Å)	11.179(4)	11.6625(9)	22.88(2)
α (°)	90	90	90
β (°)	90	90	90
γ (°)	90	90	120
Z	4	2	3
ρ (g mol^{-1})	984.51	985.52	1014.58
Dens. (g cm^{-3})	4.681	4.802	4.042
Abs. (mm^{-1})	23.257	23.834	19.491
F_{000}	1640	822	1284
Reflections (unique)	1167(175)	5177(532)	2643(423)
R_{int}	0.0523	0.0305	0.0443
R_1	0.0518	0.0291	0.0412
wR_R	0.0954	0.0513	0.1137
∂F ($e\mathring{A}^{-3}$)	1.117 & −6.062	1.637 & −3.065	1.132 & −2.843
GOF	1.102	1.388	0.905

Table 4.2: Crystallographic Data for $(FA)_2PtI_6$ and $(GUA)_2PtI_6$.

Empirical Formula	$[CH(NH_2)_2]_2PtI_6$		$[C(NH_2)_3]_2PtI_6$
Crystal habit, color	needle, bronze		block, bronze
Crystal system	monoclinic	tetragonal	hexagonal
Space group (#)	$P2_1/n$ (14)	$I4/m$ (87)	$P63mc$ (186)
Volume (Å^3)	855.0(2)	859(3)	924.8(3)
T (K)	100	350	100
a (Å)	7.679(2)	9.65(2)	9.369(2)
b (Å)	13.360(3)	9.65(2)	9.369(2)
c (Å)	8.572(2)	9.21(2)	12.164(2)
α (°)	90	90	90
β (°)	108.695(9)	90	90
γ (°)	90	90	120
Z	2	2	2
ρ (g mol^{-1})	1046.63	1041.59	1076.67
Dens. (g cm^{-3})	4.173	4.027	3.866
Abs. (mm^{-1})	19.516	18.923	17.588
F_{000}	892	882	924
Reflections (unique)	7379(2049)	956(459)	4907(1083)
R_{int}	0.0316	459	0.0335
R_1	0.0271	0.0736	0.0256
wR_R	0.0577	0.1798	0.0606
∂F ($e\mathring{A}^{-3}$)	1.313 & −2.026	1.775 & −1.275	1.992 & −1.654
GOF	1.235	1.104	1.047

Table 4.3: Refined lattice parameters of $A_2\mathrm{PtI}_6$ phases.

Forumla	$(\mathrm{NH}_4)_2\mathrm{PtI}_6$	$(\mathrm{MA})_2\mathrm{PtI}_6$	$(\mathrm{FA})_2\mathrm{PtI}_6$	$(\mathrm{GUA})_2\mathrm{PtI}_6$
a (Å)	11.175	7.955	7.790	9.424
b (Å)	11.175	7.955	13.512	12.377
c (Å)	11.175	22.918	8.630	9.424
α (°)	90	90	90	90
β (°)	90	90	109.1	90
γ (°)	90	120	90	120

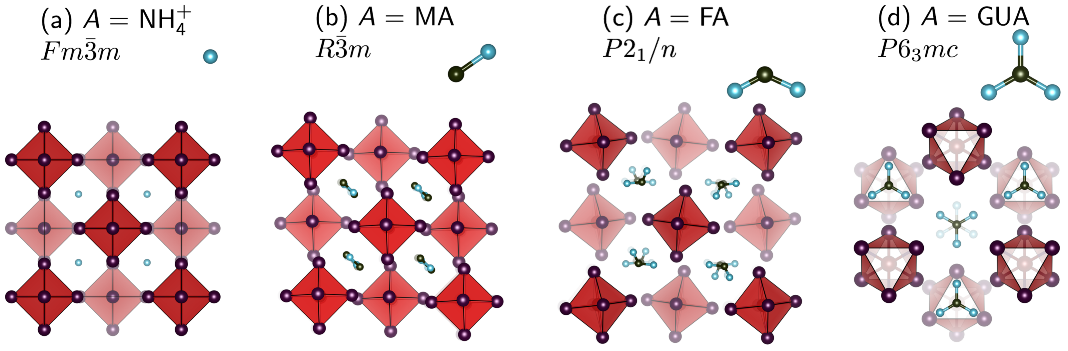
(a) $A = \mathrm{NH}_4^+$ $Fm\bar{3}m$

(b) $A = \mathrm{MA}$ $R\bar{3}m$

(c) $A = \mathrm{FA}$ $P2_1/n$

(d) $A = \mathrm{GUA}$ $P6_3mc$

Figure 4.6: Crystal structure evolution at room temperature of the $A_2\mathrm{PtI}_6$ compounds (a) $(\mathrm{NH}_4)_2\mathrm{PtI}_6$, (b) $(\mathrm{MA})_2\mathrm{PtI}_6$, (c) $(\mathrm{FA})_2\mathrm{PtI}_6$, (d) $(\mathrm{GUA})_2\mathrm{PtI}_6$ displaying the evolution from a cubic to distorted $\mathrm{K}_2\mathrm{PtI}_6$ type to eventually, the hexagonal, polar $\mathrm{K}_2\mathrm{MnF}_6$ structure type. The shading of the $[\mathrm{PtI}_6]^{2-}$ octahedra reflects depth perpendicular to the display plane. The $(\mathrm{NH}_4)_2\mathrm{PtI}_6$, $(\mathrm{MA})_2\mathrm{PtI}_6$, and $(\mathrm{FA})_2\mathrm{PtI}_6$ are viewed as if looking down [001] of the cubic parent.

Figure 4.6 depicts the A_2PtI$_6$ series beginning with the smallest organic cation containing compound, $(NH_4)_2PtI_6$, and ending with the largest, (GUA)$_2$PtI$_6$. The A = NH_4^+ compound crystallizes in undistorted cubic K_2PtCl_6 structure (space group $Fm\bar{3}m$), the MA compound in a rhombohedrally distorted variant structure (space group $R\bar{3}m$), the (FA) compound in a monoclinic variant (space group $P2_1/n$). The A = GUA compound crystallizes in a distinct structure type, of K_2MnF_6 in the polar space group $P6_3mc$.[130]

The panels of Figure 4.7 display the evolution with effective ionic radius of (a) the volume *per* formula unit and (b) the perovskite tolerance factor for the A_2PtI$_6$ compounds reported, and data on all-inorganic Rb_2PtI_6 and Cs_2PtI_6.[116] The effective radii employed for Rb^+ and Cs^+ are the 12-coordinate Shannon values.[132, 133] Values for other A cations are from Kieslich, Sun, and Cheetham.[131] Twelve-coordinate radii were employed because these appear to be consistent with the methods used to estimate the radii of the more complex ions.

Panel (a) of Figure 4.7 shows that all of the compounds except for A = FA and GUA follow a simple trend that suggests the volume *per* formula unit of A_2PtI$_6$ depends solely on the A-cation separating out the molecular $[PtI_6]^{2-}$ octahedra in the solid state. The A = FA and GUA compounds do not follow this trend, pointing to a distinct structural role, which we will presently implicate

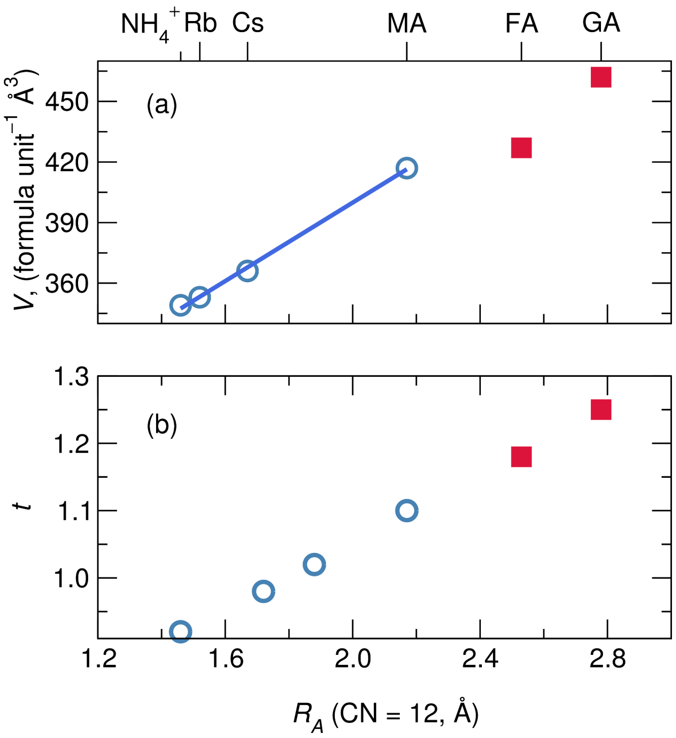

Figure 4.7: Evolution of (a) volumes *per* formula unit and (b) the perovskite tolerance factors, as a function of the *A*-effective ionic radius for octahedral coordination (CN = 12). Radii values employed are from Kieslich, Sun, and Cheetham[131] (for NH_4^+, MA, FA, and GUA) and from Shannon[132, 133] for Rb^+ and Cs^+. The symbols for A = MA and GUA are distinct to indicate they do not follow the same volume/size trend as the other compounds.

with hydrogen bonding tendencies. Panel (b) displays the evolution of the tolerance factors t of these compounds. While the tolerance factor is frequently employed to understand perovskites, including ones with more complex ammonium cations,[131] its utility in vacancy-ordered compounds of the K_2PtCl_6-type has been recently noted.[134]. We observe that the *A* = MA and FA compounds have tolerance factors that are well in excess of the range usually expected for compounds with perovskite-like arrangements of their octahedra. The other surprise is that the $(FA)_2PtI_6$ appears to display tilting and rotation, which is contrary to the expectation for $t > 1$. While t should be interpreted with care because of the absence of extended I–Pt–I connectivity in the structure, it appears to be insightful here. In particular, when t is significantly greater than unity, we see the kind of structural transformation, from $Fm\bar{3}m$ K_2PtCl_6-type, to $P6_3mc$ K_2MnF_6-type that is reminiscent of what happens with perovskites when the tolerance factor becomes large, for example, the transformation from the structure of $SrRuO_3$ to $BaRuO_3$.[135]

To complement the crystallography and to better understand the role of the *A*-cation, we have employed room temperature ^{1}H and ^{195}Pt solid state nuclear magnetic resonance (ssNMR) spectroscopy. This NMR analysis was done predominantly by Dr. Douglas Fabini. ^{1}H ssNMR confirmed the identity of each molecular cation and probed aspects of each cations motion, and ^{195}Pt ssNMR

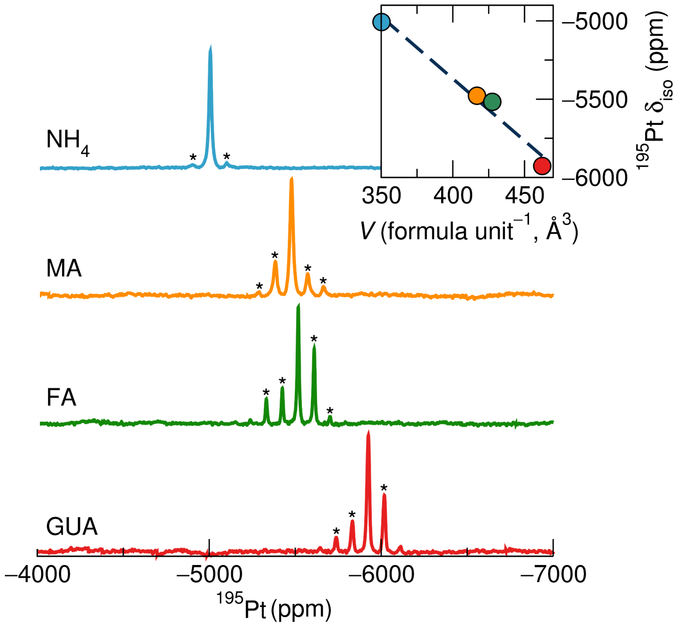

Figure 4.8: Room temperature 10 kHz MAS ^{195}Pt NMR spectra of A_2PtI_6 showing the influence of the countercation on chemical shift and lineshape. Asterisks indicate spinning sidebands, shifts are referenced to a 1 M solution of Na_2PtCl_6 in D_2O (0 ppm), and the field is 11.7 T (500 MHz for ^{1}H). Inset: Isotropic ^{195}Pt chemical shift, δ_{iso}, is correlated with unit cell volume per formula unit, V / F.U. A dashed line is drawn as a visual guide.

Table 4.4: ^{1}H longitudinal relaxation times, T_1, for A_2PtI$_6$ phases, with confidence intervals expressed as $\pm\ 1\sigma$.

A	**^{1}H T_1 (s)**
NH$_4$	6.18 ± 0.07
MA	5.66 ± 0.24
FA	1.35 ± 0.01
GUA	0.598 ± 0.004

examined the local Pt environments to confirm our crystallographic models. ^{195}Pt single-pulse NMR spectra with 10 kHz magic-angle spinning (MAS) are presented in Figure 4.8, as well as the relation between isotropic chemical shift and unit cell volumes. For all members of the A_2PtI$_6$ series only a single Pt site was observed, in agreement with the crystallographic studies. A clear monotonic upfield shift with increasing countercation size is evident, as well as significant differences in chemical shielding anisotropy (CSA) and linewidths. Lineshape and CSA parameters are given in Table 4.5, found in the Results and Discussion section, correlate well with Pt site symmetries from X-ray diffraction.

^{1}H inversion recovery experiments were conducted to assess the degree of molecular motion in the A_2PtI$_6$ phases (Figure 4.21), and resulting longitudinal relaxation times, T_1, are given in Table 4.4. We observe that T_1 is substantially longer in the ammonium and methylammonium phases. The theory of Bloembergen, Purcell, and Pound (BPP)[136] has been applied to establish molecular correlation times in similar compounds,[137–141] because in these plastic crystals, longitudinal relaxation is usually mediated by ^{1}H dipolar interactions that fluctuate due to molecular motion. In the "fast motion" limit ($\omega_0\tau_C \ll 1$, where ω_0 is the nuclear Larmor frequency and τ_C is the autocorrelation time for molecular motion) which is valid for similar plastic crystals at ambient temperature, the expression for longitudinal relaxation time in BPP theory reduces $\tau_C \propto T_1^{-1}$. While there are small differences in the proportionality prefactor related to dipole-dipole separation, the substantially longer T_1 values for the ammonium and methylammonium phases imply more rapid molecular motion (short τ_C) compared to the FA and GUA compounds, which may be expected simply on the basis of molecular size. However, it is well known that strong hydrogen bonding of cations like FA and GUA can produce rigid structures, as seen in formate based perovskites,[142, 143] or in the recently reported high-temperature ferroelectric material (3-ammoniopyrrolidinium)$\mathrm{RbBr_3}$.[144] Furthermore, when compared to MA and FA lead iodide perovskites ($A\mathrm{PbI_3}$) where the molecular cations are known to reorient at room temperature (and below),[141] these two compounds only undergo phase transitions to structures with cation disorder when brought to well above room temperature (Figures 4.15 and 4.16.

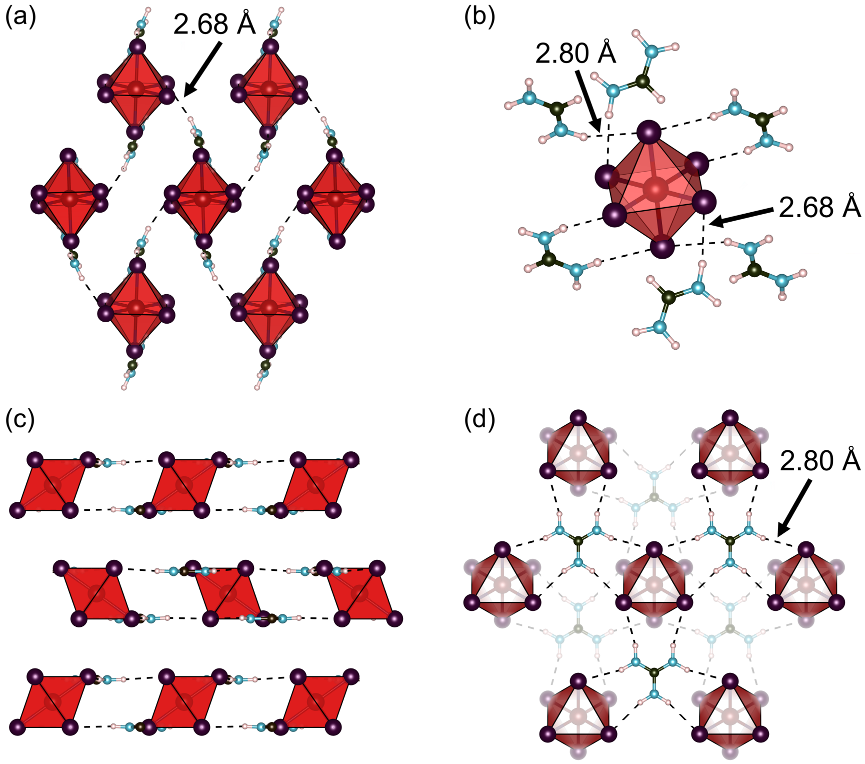

Figure 4.9: Crystallographic depictions of *ab initio* relaxed structures of $(FA)_2PtI_6$ [(a) and (b)] and $(GUA)_2PtI_6$ [(c) and (d)] illustrating their hydrogen bond networks. (a) View of the 3D connected network of hydrogen bonds linking $[PtI_6]^{2-}$ octahedra in $(FA)_2PtI_6$. The hydrogen bond length of all bonds shown in (a) is 2.68 Å . (b) View of a representative $[PtI_6]^{2-}$ octahedron in $(FA)_2PtI_6$ with FA cations that hydrogen bond to it. (c) View of the 2D connected network of hydrogen bonds linking $[PtI_6]^{2-}$ octahedra in $(GUA)_2PtI_6$. (d) View along the layering direction of GUA cations hydrogen bonding to nearby $[PtI_6]^{2-}$. Each GUA cation bonds to a total of six iodides on three separate $[PtI_6]^{2-}$ octahedra.

To better understand if hydrogen bonding can explain the suspected reduced molecular motion of the cations in $(FA)_2PtI_6$ and $(GUA)_2PtI_6$, we examined how hydrogen bonds arrange in *ab initio* relaxed structures. Figure 4.9 shows crystallographic depictions of $(FA)_2PtI_6$ and $(GUA)_2PtI_6$ (including hydrogen bonds). It can be seen in Figure 4.9(a) that FA cations hydrogen bond with iodides on $[PtI_6]^{2-}$ octahedra to form a connected network, and in Figure 4.9(b), how a representative $[PtI_6]^{2-}$ octahedron is surrounded by the FA cations. Each FA cation forms a total of 4 hydrogen bonds ($N–H\cdots I$), two to two iodides on one $[PtI_6]^{2-}$ octahedron (with bond lengths of 2.71 Å and 2.84 Å), and two "bridging bonds" to two other iodides on two separate neighboring $[PtI_6]^{2-}$ octahedra (bond lengths of 2.68 Å and 2.80 Å). These bridging bonds have been labeled in Figures 4.9(a) and (b) where visible, and are responsible for linking the discrete $[PtI_6]^{2-}$ octahedra together. All of these bonds create a 3D connected hydrogen bond network for $(FA)_2PtI_6$, suggesting that hydrogen bonding may contribute substantially to the suspected reduced molecular motion of the formaminidinium cation. Figure 4.9(c) shows the 2D hydrogen bond network formed in $(GUA)_2PtI_6$, and Figure 4.9(d) illustrates a top-down view emphasizing the orientation of the GUA cations in relation to nearby $[PtI_6]^{2-}$ octahedra. Figure 4.9(c) displays a 2D connected network of hydrogen bonded GUA cations and $[PtI_6]^{2-}$ octahedra, where each GUA cation hydrogen bonds to a total of six iodides on three separate $[\mathrm{PtI_6}]^{2-}$ octahedra. In Figure 4.9(d), one can see how there are two guanidiniums layers per one layer of $[\mathrm{PtI_6}]^{2-}$ octahedra. Similar to the hydrogen bonding seen in $(\mathrm{FA})_2\mathrm{PtI_6}$, we find that the location of the bonds in $(\mathrm{GUA})_2\mathrm{PtI_6}$ help explain the suspected reduced molecular motion of the organic cation, as each hydrogen on the guanidinium cations aligns directly with a nearby $[\mathrm{PtI_6}]^{2-}$ iodide. Indeed, we believe it is not a coincidence that the space group symmetry of $(\mathrm{GUA})_2\mathrm{PtI_6}$ is compatible with the shape of the GUA cation. From this examination, we believe that the hydrogen bonds formed by these large organic cations actually dictate the observed structural trends in $(\mathrm{FA})_2\mathrm{PtI_6}$ and $(\mathrm{GUA})_2\mathrm{PtI_6}$.

Furthermore, the hypothesis of reduced motion in the FA and GUA compounds is consistent with the analysis of hydrogen bonding geometries. Steiner has reported average hydrogen bond donor$\cdots$acceptor and H$\cdots$acceptor distances based on a crystallographic database analysis of crystal structures determined by neutron diffraction.[145] The donor$\cdots$acceptor distances reported are very similar for $-\mathrm{N}sp^2\mathrm{H_2}$ and $-\mathrm{N^+H_3}$ donors and iodide acceptors ($\approx$3.7 Å). Donor$\cdots$acceptor distances in the X-ray crystal structures of the $A_2\mathrm{PtI_6}$ phases presented are similar for FA and GUA (3.63 Å and 3.76 Å respectively), while those for ammonium (3.95 Å) fall outside the reported distribution, and the donor–H$\cdots$acceptor bond angles for methylammonium (139°) are outside the range considered by Steiner. This analysis would suggest that molecular motion could be uninhibited in the ammonium phase, while hydrogen bonding to the neighboring anions significantly restricts molecular motion in the FA and GUA phases.

The electronic band structures of the A_2PtI_6 phases, calculated within the framework of density functional theory (DFT), are presented in Figure 4.10 (details are provided in the Experimental Methods section). These calculations were done by Dr. Douglas Fabini. In all cases, the bandgap is between filled I p orbitals and empty Pt e_g orbitals, as expected for a low spin d^6 $[PtI_6]^{2-}$ polyanion. The valence and conduction bands across the series of compounds display diminished dispersion as one traverses across from the smaller $A = NH_4^+$ cation to MA and FA. In the hexagonal structure of $(GUA)_2PtI_6$, the valence and conduction bands are nearly fully localized. For the smaller A cations, the iodine sublattice is essentially close-packed, leading to overlap of the large 5p orbitals between neighboring $[PtI_6]^{2-}$ anions. For the undistorted $(NH_4)_2PtI_6$, despite the extended interactions being non-bonded the conduction bandwidth ($\approx$1 eV) is significant, and despite the central cation being different, it is similar to those reported for isostructural Cs_2SnI_6 and Cs_2TeI_6 where delocalized states similarly emerge due to iodine close-packing.[24–26] In all cases the bandgaps are indirect, but there are direct transitions that are only slightly higher in en-

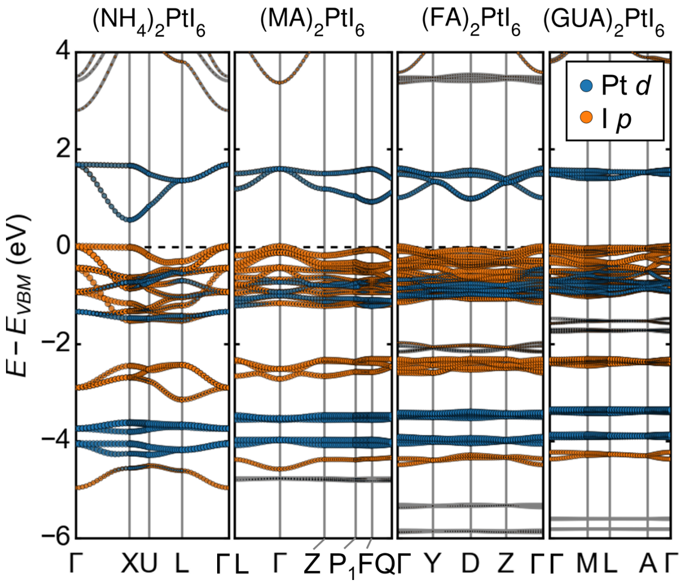

Figure 4.10: Electronic band structures (GGA-PBE) for $A_2\text{PtI}_6$ phases, illustrating decreasing bandwidths (and increasing bandgaps) with increasing countercation size. Orbital projections of Pt d character and I p character are presented as colored markers of variable size. In all cases, the valence bands derive primarily from the 5p orbitals of I, while the conduction bands derive from the unoccupied Pt 5d orbitals with irrep e_g. The effect of spin-orbit coupling is shown to be modest (see Figure S9). Energies are referenced to the valence band maximum for each phase.

ergy (discussed in the Additional Material Characterization section) Additionally, the electronic bandgaps and line-effective masses for electrons and holes are given in Table 4.6, together with cell volumes from ab initio structure relaxation in Table 4.7. The computed band structures also offer an explanation for the downfield ^{195}Pt chemical shift with decreasing countercation size. The increasingly delocalized electronic states from closer intermolecular contact draw some charge density away from the Pt nucleus and into the intermolecular regions, deshielding the Pt nucleus.

Ab initio Optical absorption coefficients for the A_2PtI_6 series are displayed in Figure 4.11. Values for weakly absorbing c-Si and strongly absorbing $CuSbS_2$,[146] calculated similarly, are given for comparison. Additionally, the spectral dependence for solar irradiance (direct+diffuse at global tilt, ASTM G173-03) is included for reference. [http://rredc.nrel.gov/solar/spectra/am1.5/astmg173/astmg173.html (accessed 12/4/2017)] For all of the Pt(IV) iodides, the absorption onset is rather strong despite their indirect bandgaps, reflecting a relatively high joint density of states near the band gap due to the partially localized nature of the electronic structure. The $A = NH_4^+$ compound, with the most disperse bands, displays the lowest-energy absorption edge, as expected from the band structure. The A = MA and FA compounds display very similar calculated absorption edges and the A = GUA compound has the

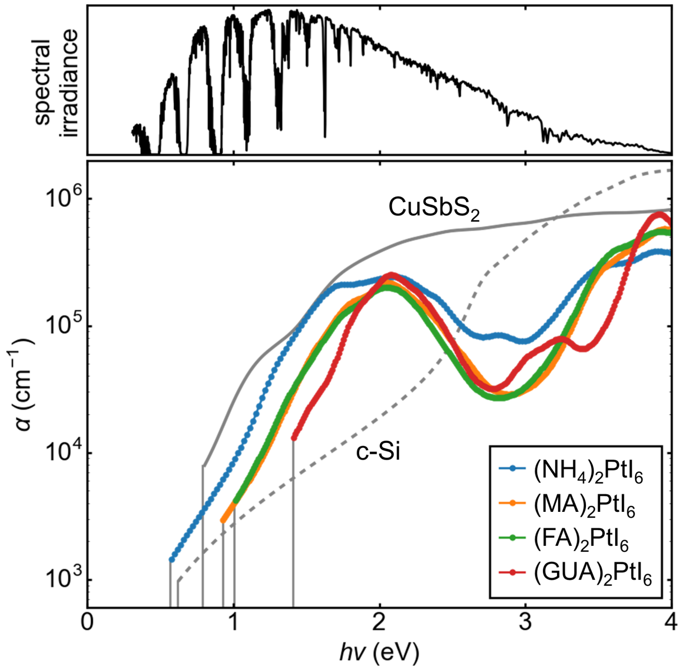

Figure 4.11: Ab initio optical absorption coefficients (GGA-PBE) for A_2PtI$_6$ phases, with bandgaps indicated by vertical gray lines. Indirect gap crystalline silicon (c-Si, dashed gray line) and the strongly absorbing direct gap chalcogenide CuSbS$_2$ (solid gray line) are included for comparison. Absorption in the violet/near-UV is poor for the A_2PtI$_6$ phases due to the paucity of available states immediately above the unoccupied Pt e_g states.

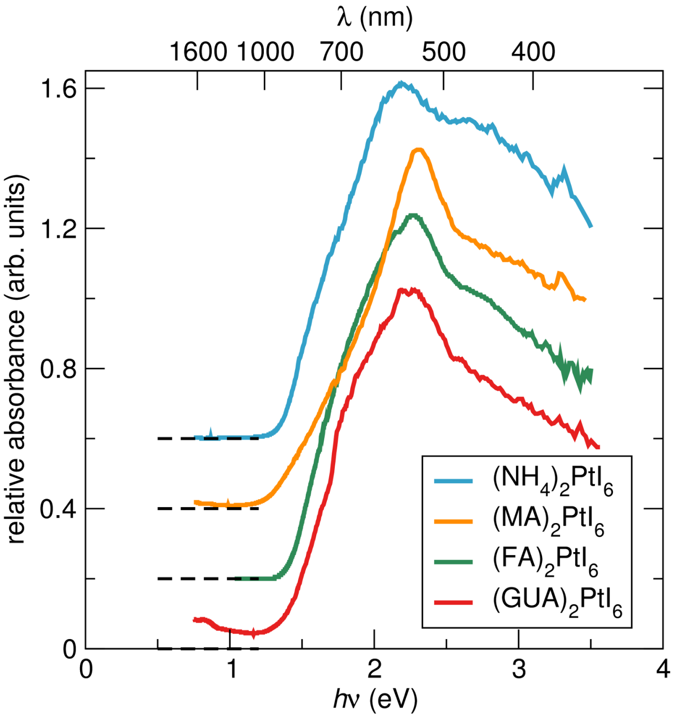

Figure 4.12: Normalized optical absorption spectra of the A_2PtI$_6$ compounds recorded on powders, obtained from Kubelka-Munk transformation of UV-Vis diffuse reflectance powder spectra.

highest-energy absorption edge, in keeping with its more molecular nature. Despite slight differences in the near-IR and red due to the modestly differing bandwidths, the A_2PtI$_6$ phases exhibit very similar absorption around 2 eV, reflecting the similar underlying molecular character. Absorption is weak for these phases in the violet and near-UV, a consequence of the wide gap between the Pt e_g conduction bands and the next higher lying excited states.

Experimental optical absorption spectra are displayed in Figure 4.12. The observed absorption onsets across the different compounds appear to be quite similar, exhibiting a peak in the absorption about 1 eV above the absorption edge, similar to what was calculated for these compounds. The red-shift of the peak in the calculated spectra when compared with experiment is consistent with the functionals employed in the DFT calculation. The more disperse valence and conduction bands calculated for the $A = \mathrm{NH}_4^+$ compound give rise to the slightly sharper absorption edge, at lower energy than seen for the other compounds.

In conclusion, the evolution of the structure and properties of the compound $A_2\mathrm{PtI}_6$ series, where A NH_4^+, MA, FA, and GUA, suggests the importance of hydrogen bonding for stabilizing some of the structures with the larger A cations, and the role of nonbonded I^-–I^- interactions in establishing relatively disperse electronic bands for the compounds with the smaller A-cations. We describe how as cation size increases, the structures undergo progressive distortion from the parent cubic vacancy-ordered double perovskite $\mathrm{K}_2\mathrm{PtCl}_6$-type structure, until converting to the the $\mathrm{K}_2\mathrm{MnF}_6$ structure type with $(\mathrm{GUA})_2\mathrm{PtI}_6$. Analysis of ^{1}H ssNMR T_1 relaxation times and *ab initio* relaxed structures of $(\mathrm{FA})_2\mathrm{PtI}_6$ and $(\mathrm{GUA})_2\mathrm{PtI}_6$ suggest that FA and GUA cations engage in strong hydrogen bonding interactions with nearby iodide atoms on separate $[\mathrm{PtI}_6]^{2-}$ octahedra, causing reduced cation molecular motion and distinct structural signatures at room temperature.

The hydrogen bonds appear to guide the final structure formation for the FA and GUA compounds, with structures that can be best described as hydrogen-bonded networks. From DFT calculations, it is found that the intermolecular contact through close-packed iodide anions leads to dispersive frontier bands for the phases with smaller molecular ions.

4.4 Additional material characterization

4.4.1 Calorimetry

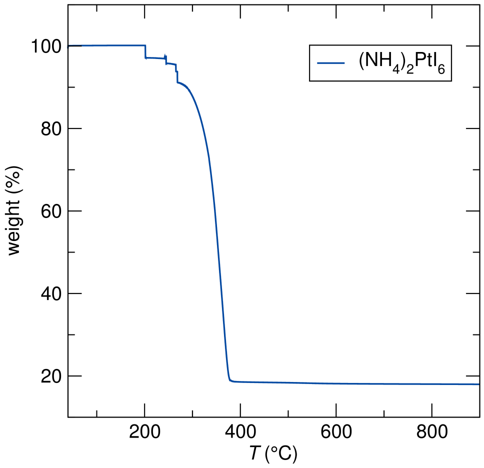

Figure 4.13: TGA data for $(NH_4)_2PtI_6$ from room temperature to 900°C.

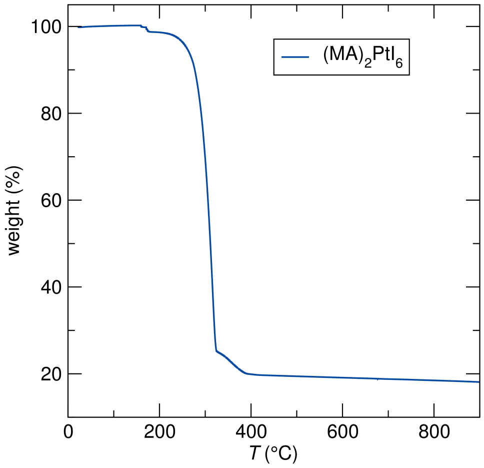

Figure 4.14: TGA data for $(MA)_2PtI_6$ from room temperature to 900°C.

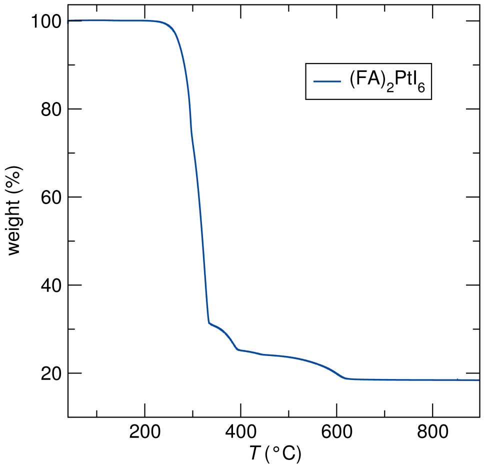

Figure 4.15: TGA data for $(FA)_2PtI_6$ from room temperature to 900°C.

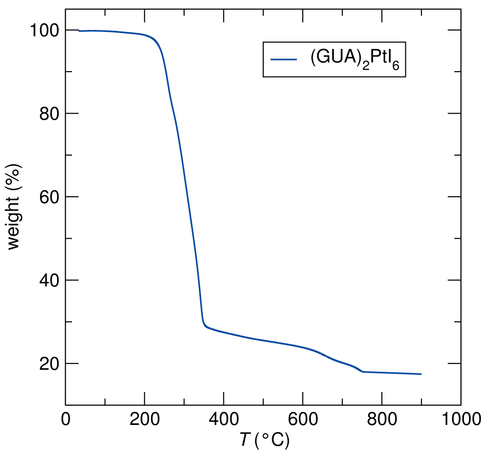

Figure 4.16: TGA data for $(GUA)_2PtI_6$ from room temperature to 900°C.

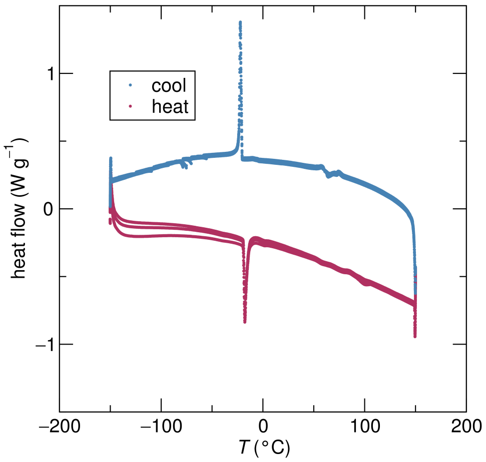

Figure 4.17: DSC data for $(NH_4)_2PtI_6$ between $-150\,^\circ$C and $150\,^\circ$C. A first order phase transition can be seen at -20°C.

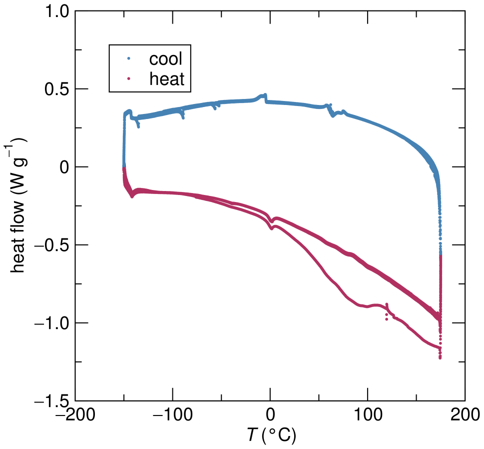

Figure 4.18: DSC data for $(MA)_2PtI_6$ between −150 °C and 175 °C. No first order phase transition is observed.

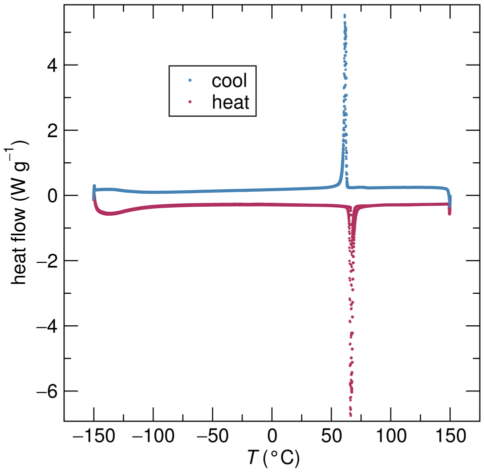

Figure 4.19: DSC data for $(FA)_2PtI_6$ between −150 °C and 150 °C. A first order phase transition is observed near 63°C.

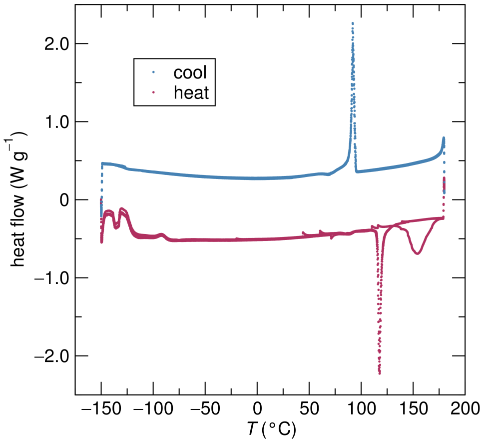

Figure 4.20: DSC data for $(GUA)_2PtI_6$ between $-150\,^{\circ}$C and $175\,^{\circ}$C. There is a second order phase transition near 100°C associated with increased molecular motion of the guanidinium cation.

Thermogravimetric analysis, presented in Figures 4.13 - 4.16, show similar degradation temperatures for each member of the A_2PtI_6 series. Differential scanning calorimetry of the A_2PtI_6 series is presented in Figures 4.17 - 4.20, with details in each respective caption.

4.4.2 Supplementary Nuclear Magnetic Resonance (NMR)

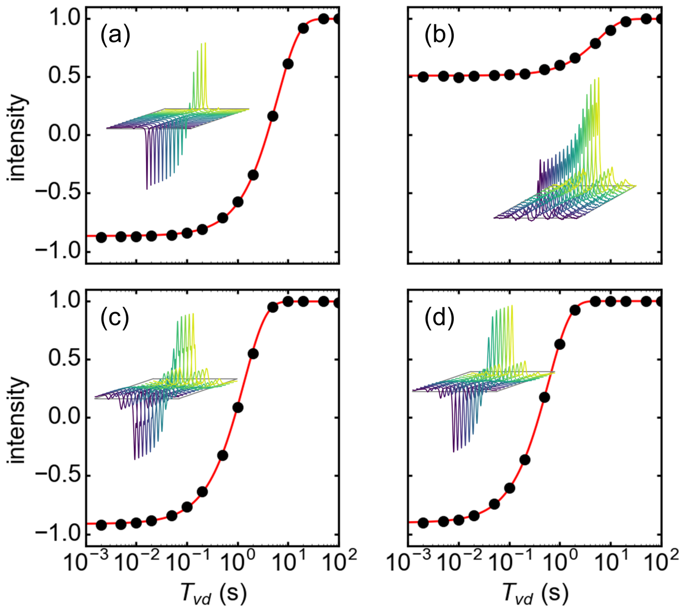

Figure 4.21: ^{1}H inversion recovery experiments of the A_2PtI$_6$ series. (a) $(NH_4)_2PtI_6$, (b) $(MA)_2PtI_6$, (c) $(FA)_2PtI_6$, (d) $(GUA)_2PtI_6$.

^{1}H inversion recovery experiments (Figure 4.21) were conducted to assess the degree of molecular motion in the A_2PtI$_6$ phases, and resulting longitudinal relaxation times, T_1, are given in Table 1 in the main text. We observe that T_1 is substantially longer in the ammonium and methylammonium phases, and reduced in the formamidinium and guanidinium phases.

^{1}H single-pulse NMR spectra under MAS for the A_2PtI$_6$ phases are presented in Figure 4.22. At these modest MAS speeds, ^{1}H dipolar interactions are only

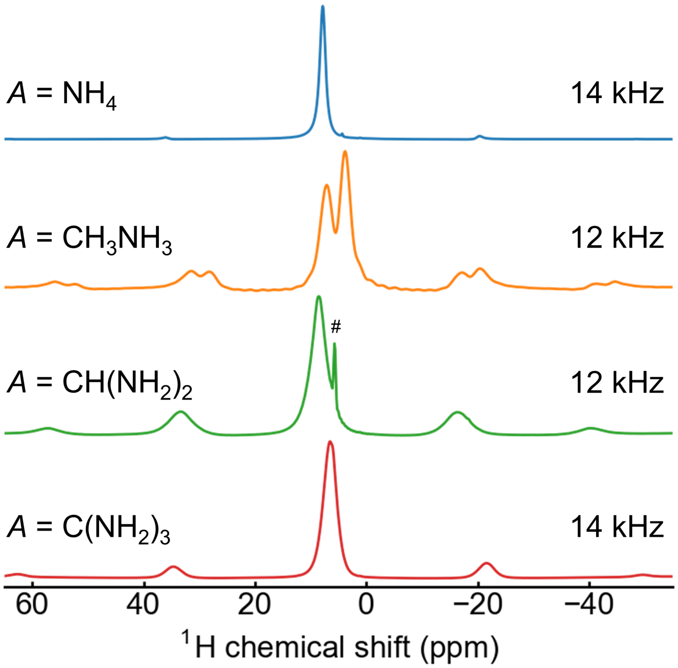

Figure 4.22: MAS ^{1}H NMR spectra of A_2PtI$_6$ phases, with spinning speed indicated. A small (3%), mobile impurity is evident in (FA)$_2$PtI$_6$ at 5.7 ppm, potentially from a NH$_4$ impurity generated through degradation of the formamidinium precursor. At this modest speed, strong ^{1}H dipolar interactions prevent resolution of the three chemically distinct protons on the formamidinium ion which are evident in solution. As [NH$_4$]$^+$ and [GUA]$^+$ each have one distinct proton, the broader signal for guanidinium suggests a reduced state of molecular motion.

Table 4.5: ^{195}Pt NMR lineshape parameters for A_2PtI$_6$ phases, Pt site symmetry from X-ray diffraction, and experimental and ab initio $[\mathrm{PtI}_6]^{2-}$ octahedral volumes, V_{oct}. Ω = Guassian broadening. Ψ = Pt site symmetry

A	δ_{iso} **(ppm)**	δ_{CSA} **(ppm)**	η	Ω **(Hz)**	Ψ	**Expt. *V*$_{oct}$ (Å)**	**Calc. *V*$_{oct}$ (Å)**
NH$_4$	−5006	59	0.001	1963	$m\bar{3}m$	25.32	26.34
MA	−5478	166	0.106	2377	$\bar{3}m$	25.43	26.49
FA	−5518	218	−0.009	1066	$\bar{1}$	25.80	26.60
GA	−5926	196	0.224	1397	$3m.$	25.42	26.51

partially averaged out, and the three chemically distinct protons of the formamidinium ion cannot be resolved.

^{195}Pt lineshape and CSA parameters are given in Table 4.5, together with the Pt site symmetry from X-ray diffraction and the experimental and *ab initio* (vide infra) $[\mathrm{PtI}_6]^{2-}$ octahedral volumes. The CSA parameters correlate well with Pt site symmetry, with the smallest δ_{CSA} for the highest site symmetry ($m\bar{3}m$), and the largest δ_{CSA} for the lowest Pt site symmetry ($\bar{1}$). While no CSA would be expected for Pt in the ammonium phase, due to the octahedral site symmetry, very small sidebands are observed. These likely arise from residual heteronuclear dipolar coupling, spin-orbit coupling, or other sources of broadening. The Gaussian broadening parameters extracted in lineshape fitting indicate broader lines in the ammonium and methylammonium phase. The origin of this behavior is not immediately apparent, as subsequent analysis of motion (*vide infra*) suggests that if anything, molecular motion is faster in these phases. In sum, no features are seen in NMR which suggest that the local environments of Pt deviate significantly from those in the crystallographic models.

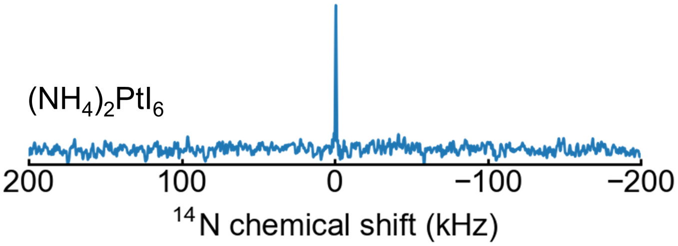

Figure 4.23: Spin-echo ^{14}N (S = 1) experiment for $(NH_4)_2PtI_6$, showing a narrow signal due to the tetrahedral molecular symmetry of the NH_4^+ cation.

Spin-echo ^{14}N (S = 1) experiments were additionally carried out (Figure 4.23) on the A_2PtI_6 phases, leveraging the quadrupole moment as a probe of motion. A narrow signal was easily observed for $A = NH_4$ due to the tetrahedral molecular symmetry, while no signals were detected for the other three phases within one hour of acquisition. This result would be consistent with insufficiently rapid molecular motion to average out strong quadrupolar interactions, which are not already canceled due to the lower symmetry N environments in these molecules, though we cannot postulate more quantitative results without protracted experiments to acquire these (presumably) extremely broad signals.

4.4.3 Electronic Structure

The electronic band structures of the $A_2\text{PtI}_6$ phases, calculated within the framework of density functional theory (DFT), are presented in Figure 4 in the main text. Crystal structures were relaxed including semi-empirical van der Waals corrections, and the exchange-correlation energy was treated with the generalized gradient approximation (GGA; full computational details in the Methods section above).

The electronic bandgaps and line effective masses for electrons and holes (not the density of states effective masses) are given in Table S5, together with cell volumes from *ab initio* structure relaxation in Table 4.7. For the $A_2\text{PtI}_6$ phases, bandgaps and effective masses increase monotonically with countercation size, consistent with our discussion of intermolecular I–I contact. Bandgaps are indirect in all cases, with the valence band maxima occurring at the zone centers. No pattern in the locations of the conduction band minima is readily apparent without detailed analysis of the spatial relationship between the Brillouin zones of the different lattice types. Despite the use of van der Waals corrections, the DFT relaxed structures overestimate unit cell volumes by 9% to 17% (corresponding to 3% to 5% linear), in line with the known underbinding of the GGA.

Table 4.6: Calculated electronic bandgaps (E_g) and line effective masses (m_e^*, m_h^*) for members of the A_2PtI_6 series. For line effective masses, the first Brillouin zone special point labels the band extremum, and the second special point indicates the direction from the extremum along which the dispersion is fitted.

Phase	E_g (eV)	VBM	CBM	m_e^* / m_0	m_h^* / m_0
$(NH_4)_2PtI_6$	0.55	Γ	X	X→Γ: 0.43	Γ→X (light): 0.64
				X→W: 0.39	Γ→X (heavy): 25.3
				X→U: 0.38	Γ→K (light): 0.64
					Γ→K (medium): 0.92
					Γ→K (heavy): 1.90
					Γ→L (light): 0.79
					Γ→K (heavy): 1.47
$(MA)_2PtI_6$	0.94	Γ	F	F→Q: 0.61	Γ→L: 1.29
				F→P_1: 0.74	Γ→Z: 1.29
					Γ→X: 2.30
$(FA)_2PtI_6$	1.00	Γ	D	D→Z: 0.78	Γ→Y: 1.75
				D→M: 0.87	Γ→X: 3.98
				D→Y: 0.61	Γ→Z: 1.74
$(GUA)_2PtI_6$	1.41	Γ	M	M→Γ: 3.46	Γ→M (light): 3.18
				M→K: 11.6	Γ→M (heavy): 6.08
				M→L: 32.2	Γ→K (light): 3.26
				K→M: 8.72	Γ→K (heavy): 5.97
				K→Γ: 3.41	Γ→A: 4.24
				K→H: 2.86	
				L→A: 2.05	
				L→H: 2.62	

Table 4.7: Calculated and experimental volume per formula unit (V / F.U.) for members of the A_2PtI_6 series.

Phase	**V / F.U. (Å ^{3}), calc.**	**V / F.U. (Å ^{3}), expt.**
$(NH_4)_2PtI_6$	382.2	350.25
$(MA)_2PtI_6$	475.1	416.83
$(FA)_2PtI_6$	501.4	427.50
$(GUA)_2PtI_6$	531.3	462.39

For $(NH_4)_2PtI_6$, the valence band is $\sim$19 meV higher at Γ than at X, while the conduction band minimum occurs at X. This phase then has an indirect bandgap, but the direct transition at X is only slightly higher in energy. The valence band is quite flat along the $\Gamma-$X line, much like the isotypic Cs_2SnI_6.[24–26]

For $(MA)_2PtI_6$, the valence band is $\sim$70 meV higher at Γ than at F, while the conduction band minimum occurs at F. This phase then has an indirect bandgap, but the direct transition at F is only slightly higher in energy.

For $(FA)_2PtI_6$, the conduction band is $\sim$30 meV lower at D than at Γ. The valence band is $\sim$25 meV higher at Γ than at X, and $\sim$25 meV higher at Γ than at X. Accordingly, the band gap is indirect, but direct transitions at both Γ and D are only slightly higher in energy.

For $(\mathrm{GUA})_2\mathrm{PtI}_6$, the conduction band is nearly degenerate in energy ($<$10 meV difference) at the M, K, and L points, with the energy at M being the lowest by a slight margin. In contrast, all other local maxima of the valence band are 10s of meV lower in energy than the valence band maximum at Γ. Once again, the bandgap is indirect, but direct transitions at K and L are only somewhat higher in energy.

The electronic densities of states calculated for the $A_2\mathrm{PtI}_6$ phases, as well as the correlation between bandgap and unit cell volume, are presented in Figure 4.24. Tracking the position of the localized I s states (not shown, $\sim$12 eV below the VBM) relative to the VBM suggests the VBM drops relative to the vacuum with increasing countercation size (and increasing bandgap). In essence, the band widths are reduced while the band centers remain nearly constant, as expected for phases with somewhat ionic Pt–I bonding and varying degrees of intermolecular I–I contact. For the distorted VHDP ammonium, methylammonium, and formamidinium phases, there is a very strong correlation between bandgap and cell volume (Figure 4.24 inset), while the different anion packing of the guanidinium phase results in a larger bandgap than expected from this trend.

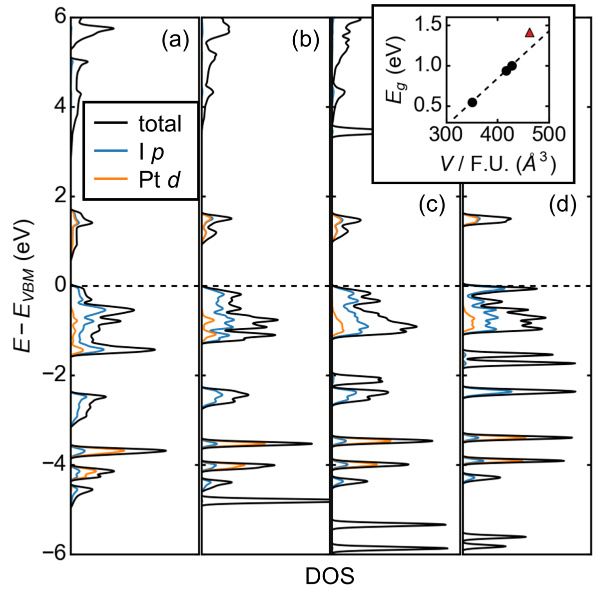

Figure 4.24: Electronic densities of states (GGA-PBE) for A_2PtI_6 phases, including orbital projections of the I p and Pt d states. Energies are referenced to the valence band maximum for each phase. Inset: The calculated bandgap is correlated with cell volume for the A = (NH_4), MA, and FA phases (●), which are increasingly distorted versions of the same anti-fluorite structure type. The transition to a different $[PtI_6]^{2-}$ packing arrangement for A = GA (△) widens the bandgap relative to this trend.

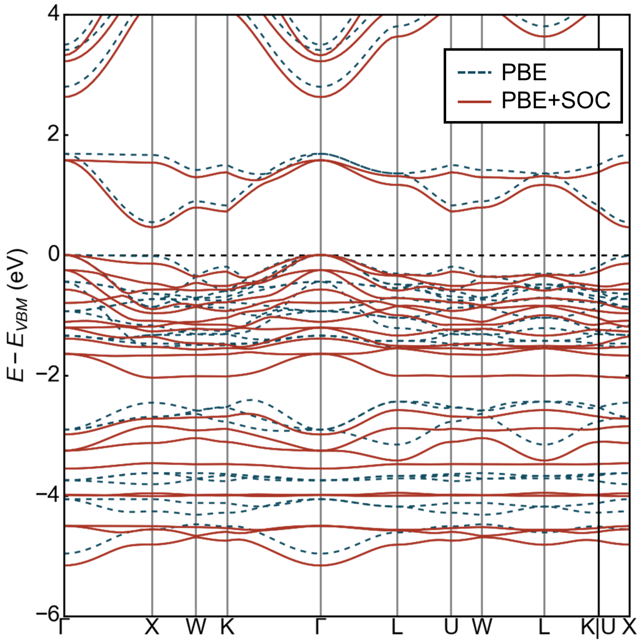

Figure 4.25: Comparison of PBE to PBE+SOC calculations for $(NH_4)_2PtI_6$.

A calculation was performed on $(NH_4)_2PtI_6$ with both PBE and PBE+SOC, which indicated that the effect of spin-orbit coupling is modest (Figure 4.25).

Chapter 5

The capricious nature of iodine catenation in I_2 excess, perovskite-derived hybrid Pt(IV) compounds

In this chapter, we describe how perovskite-derived hybrid platinum iodides with the general formula $A_2\mathrm{Pt}^{\mathrm{IV}}\mathrm{I}_6$ (A = formamidinium FA and guanidinium GUA) accommodate excess I_2 to yield hydrogen-bond-stabilized compounds,

---

[1] Hayden A. Evans, Jessica L. Andrews, Douglas H. Fabini, Molleigh B. Preefer, Guang Wu, Anthony K. Cheetham, Fred Wudl, and Ram Seshadri have contributed to the contents of this chapter.

where the I_2 forms catenates with I^- anions on the PtI_6 octahedra.

Previous publication of this data can be found in *Chemical Communications*, reproduced from the citation below, with permission from The Royal Society of Chemistry.

> Evans, H. A.; Andrews, J. L.; Fabini, D. H.; Preefer, M. B.; Wu, G.; Wudl, F.; Cheetham, A. K.; Seshadri, R. The capricious nature of iodine catenation in I_2 excess, perovskite-derived hybrid Pt(IV) compounds, **2018** *Chem. Comm.*, Advance Article, DOI: 10.1039/C8CC07536K

5.1 Introduction

The bonding of atoms of the same element into a series — the phenomenon of catenation — is commonly associated with certain second and third period main group elements such as boron, carbon, sulfur, and phosphorous. This tendency is governed by multiple factors including mean bond-dissociation energy, sterics, electronegativity, and orbital hybridization.[147] Generally, catenation occurs less frequently as one moves down the periodic table as orbitals grow more diffuse and bonding strength decreases. An exception would be catenated iodides (commonly referred to as polyiodides, although the term oligoiodide is perhaps more appropriate), which are numerous and demonstrate great diversity in length as well as in structure. At this time, the Cambridge Crystallographic Data Center (CCDC) lists approximately 1600 structures containing some form of an I–I–I linkage with three or more I atoms. Examples of solid-state oligoiodide materials include molecular salts where triodide (I_3^-) subunits are charge balanced by counter cations, and connected frameworks where many oligoiodide moieties (I_2, I_3^-, I_5^-, I_7^-, I_9^-, *etc*) link together.[148, 149] Recently, some of us reported the crystallographic structure of a rare iodine homopolymer in a pyrroloperylene-iodide compound, reminiscent of the elusive starch-iodine complex (Chapter 6.[150] The variety of oligoiodide structures results from favorable donor-acceptor interactions, and the many cations, anions, and solvent molecules that appear to impact these interactions in the solid state.

Donor-acceptor properties of iodine find many applications, including for increasing the conductivity of organic metals and conducting polymers,[151] enhancing the efficiency of dye-sensitized solar cells,[152, 153] and improving the photocatalysis of materials for hydrogen evolution.[154, 155] Recent interest in iodide-based perovskite photovoltaic materials[91, 156, 157] has engendered reports of incorporating I_3^- subunits into a hybrid bismuth iodide compound in order to introduce intergap electronic states that red-shifted the band gap.[158] This result is interesting in light of most Bi–I solar energy materials displaying relatively large bandgaps regardless of structure.[65] Materials that contained neutral I_2 molecules linking discrete $[BiI_6]^{3-}$ octahedra have been noted to display direct bandgaps of $\approx$1.3 eV.[28] However, it was stated that covalency between the I_2 and $[BiI_6]^{3-}$ iodides did not appear to be present, and the structure should not be viewed as a $[BiI_6]^{3-}$–I_2–$[BiI_6]^{3-}$ 1D chain. This suggests that simple iodine/iodide proximity, not covalency, was enough to induce favorable properties of these materials in the solid state.

Here we present the findings that the hydrogen-bonded framework perovskite-derived materials, $(FA)_2PtI_6$ and $(GUA)_2PtI_6$ (FA = formamindinium and GUA = guanidinium), which were recently studied as members of an A_2PtI_6 series,[159] can be recrystallized as excess I_2 containing compounds. The new compounds, $(FA)_2PtI_6{\bullet}2I_2$ and $(GUA)_8(PtI_6)_3[PtI_4(I_3)_2]{\bullet}2I_2$, are described herein. In order to understand how size and hydrogen bonding tendencies impact the formation of these oligoiodide materials, a dimethylammonium (DMA) Pt-I compound was also prepared and studied. The solid $(DMA)_3PtI_6(I_3)$ provides valuable insight into how hydrogen bonding is essential to stabilizing this class of halide structures. Interestingly, all three materials, despite their distinct dimensionalities, display similar optical absorption profiles.

5.2 Experimental details

The hydroiodic acid (HI, 57% wt/wt in aqueous solution, Spectrum) used for the following reactions did not contain the reducing stabilizer hypophosphorous acid (H_3PO_2). The free iodine in solution (that forms when hydroiodic acid is exposed to air) is needed for the $(FA)_2PtI_6{\bullet}2I_2$ and $(GUA)_8(PtI_6)_3[PtI_4(I_3)_2]{\bullet}2I_2$ preparations, and is also thought to be responsible for the oxidation of Pt^{2+} to Pt^{4+} during $(DMA)_3PtI_6(I_3)$ preparation.

$(FA)_2PtI_6{\bullet}2I_2$ was prepared by placing 50 mg of $(FA)_2PtI_6$ crystals in a sealed vial with a small amount of HI. The preparation of $(FA)_2PtI_6$ can be found in the Experimental Details section of Chapter 4, as well as our publication on the subject.[159] If replicated, the amount of HI included should be just enough to cover all $(FA)_2PtI_6$ crystals. This mixture was left to recrystallize for at least one month, but can proceed longer if bronze $(FA)_2PtI_6$ crystals are still seen after that time. The originally bronze, metallic-looking $(FA)_2PtI_6$ crystals will become black crystals of $(FA)_2PtI_6{\bullet}2I_2$. We note that we were unable to prepare $(FA)_2PtI_6{\bullet}2I_2$ by exposing $(FA)_2PtI_6$ crystals to either iodine vapor, or an iodine solution (in H_2O or organic solvent). Furthermore, once the crystals of $(FA)_2PtI_6{\bullet}2I_2$ are filtered, do not wash them with solvent, as doing so will destroy the crystals. It was found best to gently dry the product on filter paper, left alone for a few days to dry out.

$(GUA)_8(PtI_6)_3[PtI_4(I_3)_2]\bullet 2I_2$ was prepared following the same procedure for the preparation of $(FA)_2PtI_6\bullet 2I_2$. These crystals will also degrade with most solvents. The preparation of $(GUA)_2PtI_6$ can be found in our previous publication.[159]

$(DMA)_3PtI_6(I_3)$ was prepared by combining 99.30 mg DMAI (0.561 mmol, Sigma Aldrich, 98%) and 50 mg (0.187 mmol) $PtCl_2$ (Strem, 99.9%) in 8.0 g unstablized HI, and heated to dissolve any solid that initially formed. This solution was heated for 15 min. The solution then was slowly cooled to room temperature, where black plate habit crystals of $(DMA)_3PtI_6(I_3)$ form. These crystals were vacuum filtered, washed with diethyl ether, and vacuum-dried overnight.

Single crystal X-ray diffraction data was collected on a Bruker KAPPA APEX II diffractometer equipped with an APEX II CCD detector using a TRIUMPH monochromator with a Mo Kα X-ray source (λ = 0.71073 Å). The crystals were mounted on a cryoloop under Paratone-N oil and kept under nitrogen. Absorption correction of the data was carried out using the multiscan method as implemented in SADABS.[46] Subsequent calculations were carried out using SHELXTL.[47] Structure determination was done using intrinsic methods. All hydrogen atom positions were omitted. Structure solution, refinement, and creation of publication data was performed using SHELXTL. Crystal structures were visualized using the VESTA software suite.[48]

Powder X-ray diffraction was performed on a Panalytical Empyrean Powder Diffractometer (Bragg-Brentano HD module, no monochromator) equipped with a Cu source $\lambda = 1.5418$ Å. Rietveld refinements were performed in the TOPAS software suite.[117]

A Shimadzu UV3600 UV-NIR Spectrometer was used to gather data in diffuse reflectance mode. The poly/oligoiodide compounds tested were suspended in $BaSO_4$ medium (*via* grinding). The reflectance spectra were Kubelka-Munk transformed for relative absorbance spectra.

Thermogravimetric analysis (TGA) on all compounds was conducted using a TA Instruments Discovery instrument. A rate of $25\,cm^3/min$ dry nitrogen purge was employed with a temperature ramp rate of 10°C/min. The maximum temperature of the experiment was 900°C.

Differential scanning calorimetry (DSC) measurements were performed using a TA Q2000 calorimeter. Samples (2 mg to 10 mg each) were hermetically sealed inside TZero aluminum pans. Samples were first cooled to -150°C, then heated at 10 °C/min. This was repeated for three cycles.

Electronic structure calculations for $(FA)_2PtI_6{\bullet}2I_2$ were performed with the

Vienna Ab initio Simulation Package (VASP),[52–55] which implements the Kohn-Sham formulation of density functional theory (DFT) using a plane wave basis set and the projector augmented wave formalism[56, 57]. The generalized gradient approximation was employed using the exchange and correlation functional of Perdew, Burke, and Ernzerhof (GGAPBE).[60] The plane wave basis set cutoff energy (800 eV) and k-point mesh density ($\sim$1500 k-points per reciprocal atom for convergence of the charge density, $\sim$40,000 k-points per reciprocal atom for computing the density of states, all Γ-centered Monkhorst-Pack sampling)[118] were chosen based on convergence of the total energy. Structure relaxation was performed, including van der Waals corrections (DFT-D3 method of Grimme,[119] to a force tolerance of $4\,\mathrm{meV}\,\text{Å}^{1}$. The relaxed structure preserved the space group symmetry observed in experiment. The Brillouin zone path was that of Setyawan and Curtarolo.[121]

5.3 Results and discussion

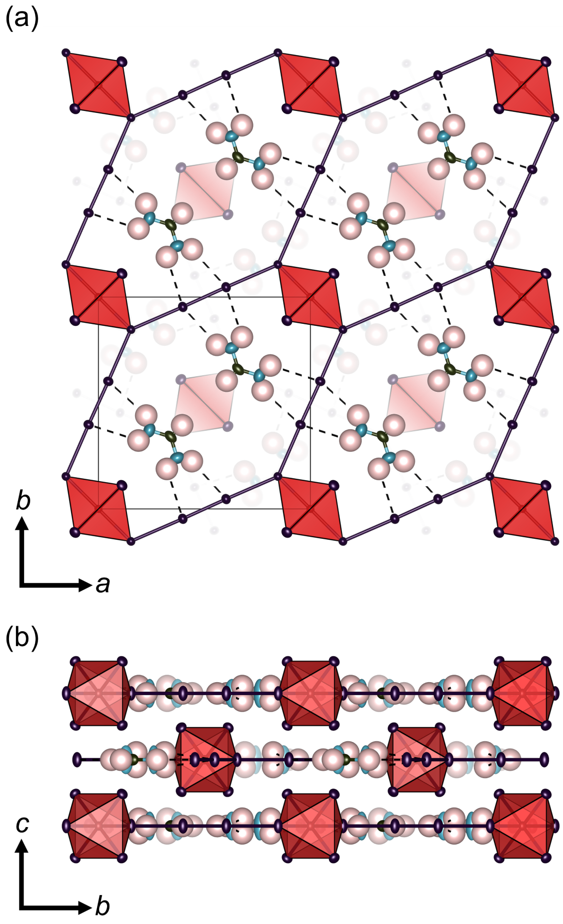

Figure 5.1: The crystal structure of $(FA)_2PtI_6{\bullet}2I_2$ at 100 K with displacement ellipsoids (95% probability). (a) Depiction of the 1D chains forming between the iodide on the $[PtI_6]^{2-}$ octahedra and I_2 molecules. Hydrogen bonding columns that form between the FA cations and the I_2 molecules are displayed with dashed lines. The pertinent bond lengths are: I_2 molecule 2.77 Å; I_2–I^- 3.29 Å; N-H$\cdots I_2$ 3.0 Å. (b) Side view of the 2D sheets that are found parallel to the ab plane.

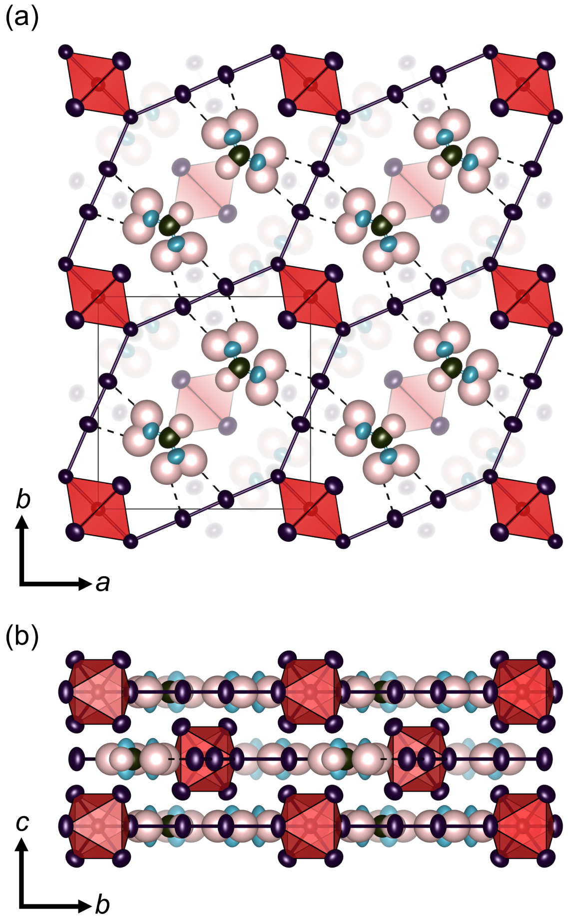

Figure 5.2: The crystal structure of $(FA)_2PtI_6{\bullet}2I_2$ at 260 K with displacement ellipsoids (95% probability). (a) Depiction of the 1D chains forming between the iodide on the $[PtI_6]^{2-}$ octahedra and I_2 molecules. Hydrogen bonding columns that form between the FA cations and the I_2 molecules are displayed with dashed lines. The pertinent bond lengths are: I_2 molecule 2.76 Å; I_2–I^- 3.32 Å; N-H$\cdots I_2$ 3.05 Å. (b) Side view of the 2D sheets that are found parallel to the ab plane.

Table 5.1: Crystallographic information for $(FA)_2PtI_6{\bullet}2I_2$.

Empirical Formula	$[CH(NH_2)_2]PtI_6{\bullet}2I_2$	
Crystal habit, color	block, black	
Crystal system	tetragonal	tetragonal
Space group (#)	$P4_2/mnm$ (136)	$P4_2/mnm$ (136)
Volume (Å^3)	1178.6(4)	1200.3(16)
T (K)	100	270
a (Å)	12.340(2)	12.379(7)
b (Å)	12.340(2)	12.379(7)
c (Å)	7.728(1)	7.833(5)
α (°)	90	90
β (°)	90	90
γ (°)	90	90
Z	2	2
ρ (g mol^{-1})	1554.23	1554.23
Dens. (g cm^{-3})	4.379	4.328
Abs. (mm^{-1})	19.040	18.698
F_{000}	1316	1336
Reflections (unique)	6507 (1005)	3456 (995)
R_{int}	0.0258	0.0574
R_1	0.0217	0.0337
wR_R	0.0412	0.0408
∂F ($e\mathring{A}^{-3}$)	1.117 & -6.062	1.132 & -1.266
GOF	1.102	1.208

The structure of the hybrid platinum polyiodide material, $(FA)_2PtI_6{\bullet}2I_2$, is presented in Figures 5.1 and 5.2, with relevant crystallographic information from the single crystal X-ray diffraction analysis in Table 5.1. Figure 5.1 (a) and 5.2 (a) emphasize the intriguing 1D polyiodide chains that form in $(FA)_2PtI_6{\bullet}2I_2$ between apical iodides of the $[PtI_6]^{2-}$ octahedra and the I_2 molecules, as well as the 1D hydrogen bonding columns that form between the FA cations and the same I_2 molecules. Figure 5.1 (b) and 5.2 (b) depicts the sheet-like structure formed by the I_2–$[PtI_6]^{2-}$ chains and the columns of FA cations and I_2 molecules. Compounds which present I_2 molecules or polyiodide moieties in donor-acceptor interactions with metal halide octahedra, similar to the aforementioned I_2–$[BiI_6]^{3-}$ system, are fairly common,[27, 148, 160, 161] but the infinite 1D I_2–I–I_2 chain that extends through the structure of $(FA)_2PtI_6{\bullet}2I_2$ is to our knowledge the first example reported with such short distances between atoms.[162] By convention, covalent bonds between iodine/iodide atoms should have an interatom distance of no greater than 3.30 Å.[148] At 300 K, the single crystal X-ray diffraction measured distance of the I_2–I^- *bond* in $(FA)_2PtI_6{\bullet}2I_2$ is 3.32 Å, and at 100 K it is 3.30 Å. If we adhere to the 3.30 Å cutoff, only the low temperature structure of $(FA)_2PtI_6{\bullet}2I_2$ qualifies as a polyiodide material, but as we later demonstrate via Raman spectroscopy, this material displays vibrations indicative of a polyiodide material at 300 K. Furthermore, at both 100 K and 300 K, the I_2 intermolecular bond lengths are longer than the known solid-state I_2 bond distance of 2.67 Å (2.75 Å and 2.77 Å, respectively) suggesting that between 300 K and 100 K the donor apical iodides of the $[PtI_6]^{2-}$ octahedra are decreasing the I_2 I–I bond order. This is in agreement with a molecular orbital (MO) description of this compound,[163] which shows that the highest occupied molecular orbital (HOMO) has some degree of antibonding character.

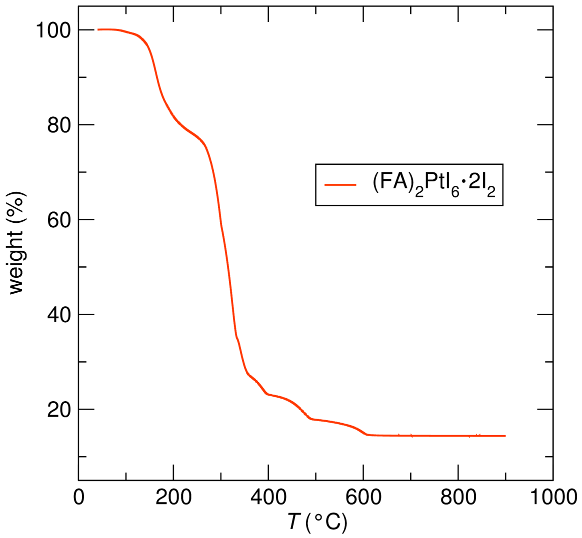

Figure 5.3: TGA data for $(FA)_2PtI_6{\bullet}2I_2$ from room temperature to 900°C.

Additionally, we note the significance of certain characteristics of the FA cations in $(FA)_2PtI_6{\bullet}2I_2$. Firstly, they are ordered, which is unlike the "tumbling" FA and methylammonium cations in $APbI_3$ perovskites.[137, 164–166] Secondly, they hydrogen bond explicitly with the I_2 molecules and not the $[PtI_6]^{2-}$ iodides, as seen in the parent compound, $(FA)_2PtI_6$. If one considers both the FA cation arrangement, and the I_2 molecules location relative to the apical iodides on the $[PtI_6]^{2-}$ octahedra, one can see that these are potential structural signatures of halogen bonding.[167] In halogen bonding, covalently bonded, easily polarizable halogen atoms (like iodine) can form nucleophilic (negative) and electrophilic (positive) sides, with the electrophilic side being denoted as the "σ-hole." We have calculated the electron localization function (ELF) and electrostatic potential for $(FA)_2PtI_6 \bullet 2I_2$, and discuss the results in the last section of this chapter.

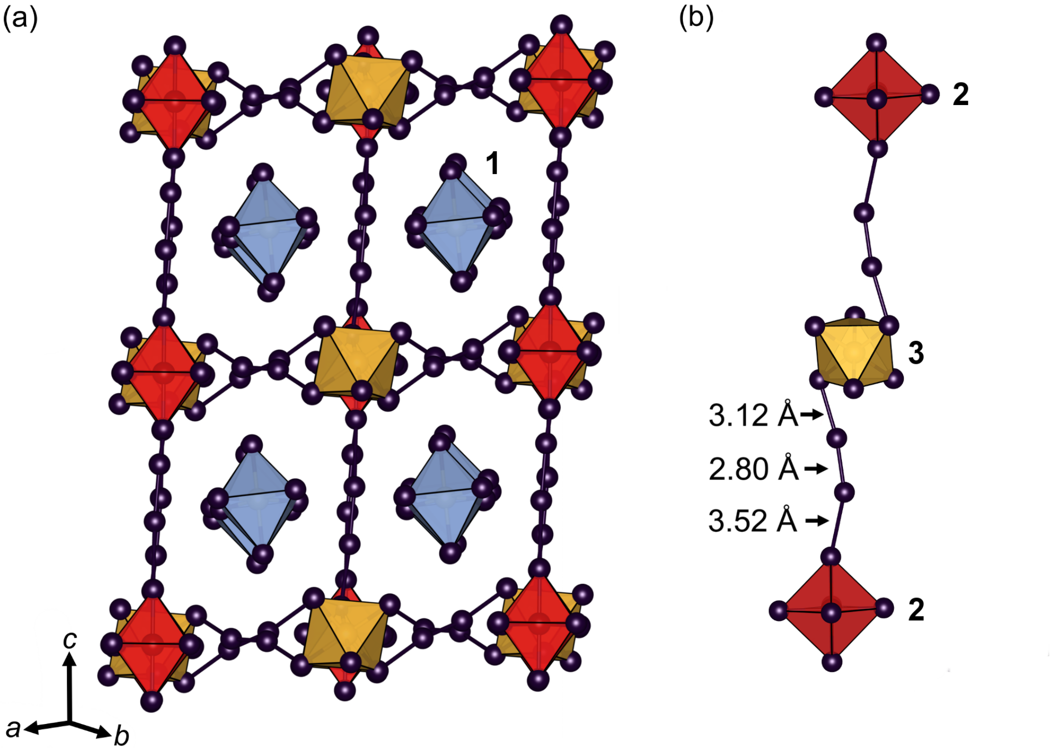

Figure 5.4: The crystal structure of $(GUA)_8(PtI_6)_3[PtI_4(I_3)_2]{\bullet}2I_2$ without organic cations at 100 K. Atom color key; I = purple, N = blue, C = black, H = white.(a) View of the $(GUA)_8(PtI_6)_3[PtI_4(I_3)_2]{\bullet}2I_2$ structure with organic cations omitted for clarity, so as to better display the oligoiodide network. To signify crystallographic independence, the Pt octahedra colors are varied and labeled with bolded numbers **1**-**3** in the $(GUA)_8(PtI_6)_3[PtI_4(I_3)_2]{\bullet}2I_2$ structure. (b) View of the crystallographically observed $[PtI_4(I_3)_2]^{2-}$ moiety **3** that forms secondary bonding chains along the c-axis with $[PtI6]^{2-}$ octahedra **2**.

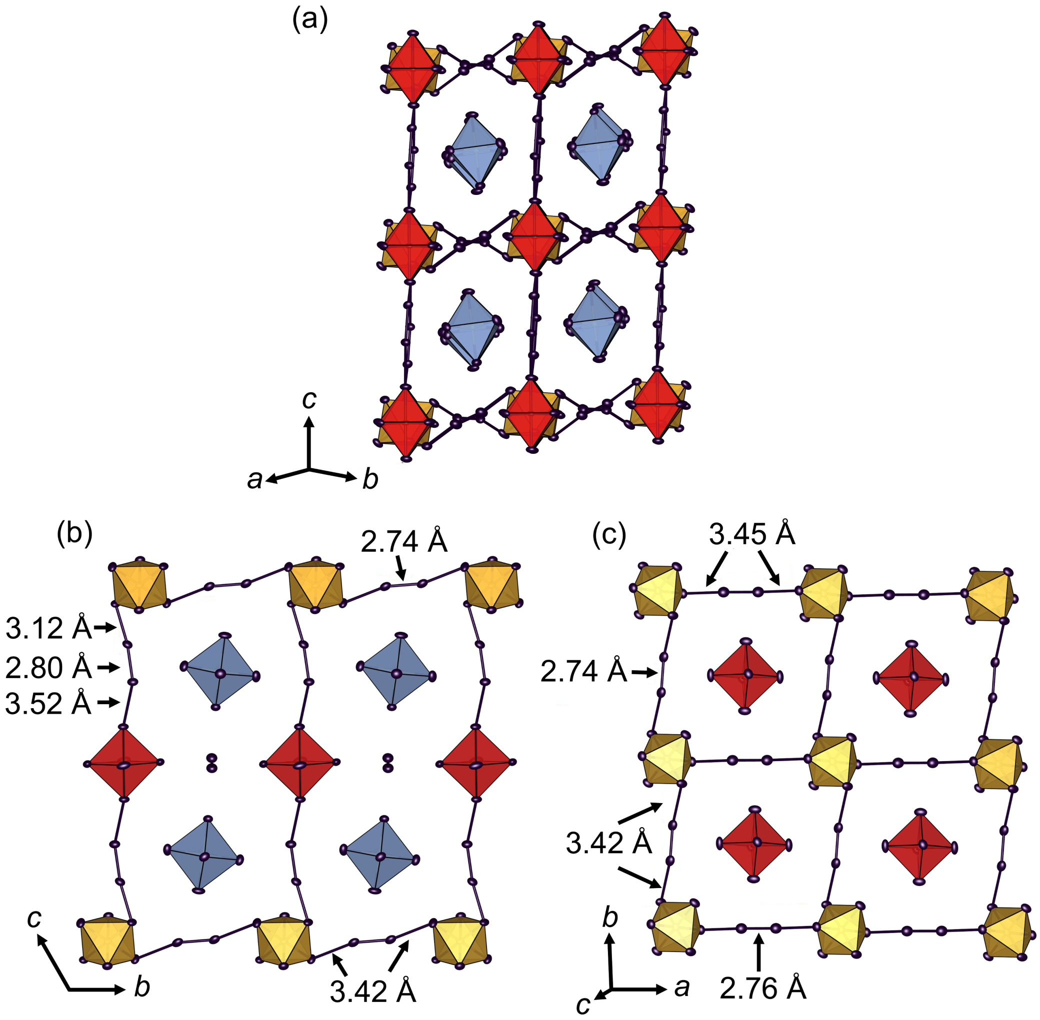

Figure 5.5: Crystal structure of $(GUA)_8(PtI_6)_3[PtI_4(I_3)_2]{\bullet}2I_2$ at 100 K with displacement ellipsoids (95% probability). (a) Depiction of the $(GUA)_8(PtI_6)_3[PtI_4(I_3)_2]{\bullet}2I_2$ structure with organic cations omitted. (b) Top down view of the cb-plane of $(GUA)_2PtI_6{\bullet}I_2$, demonstrating the secondary iodide bonding network that forms between **2** and **3**. The I_3 moieties of **3** run perpendicular to the b-axis, and link with **2**. The I_2 molecules seen in between **1** and **2** in this view are the I_2 molecules that link **3** along the a-axis seen in (c). (c) Top down view of the secondary bonding axis in the ab-plane, which forms between I_2 molecules and the four equatorial I^- iodides of **3**.

Table 5.2: Crystallographic information for $((GUA)_8(PtI_6)_3[PtI_4(I_3)_2]{\bullet}2I_2$, 100 K.

Empirical Formula	$[C(NH_2)_3]_8(PtI_6)_3[PtI_4(I_3)_2]{\bullet}2I_2$
Crystal habit, color	block, black
Crystal system	triclinic
Space group (#)	$P\bar{1}$ (2)
Volume (Å^3)	2176(3)
T (K)	108
a (Å)	12.768(9)
b (Å)	13.016(9)
c (Å)	14.52(1)
α (°)	110.55(2)
β (°)	102.74(2)
γ (°)	93.87(2)
Z	1
ρ (g mol^{-1})	5321.86
Dens. (g cm^{-3})	4.061
Abs. (mm^{-1})	17.793
F_{000}	2272
Reflections (unique)	9573 (4834)
R_{int}	0.1981
R_1	0.0817
wR_R	0.1936
∂F ($e\mathring{A}^{-3}$)	4.382 & −4.836
GOF	0.939

The structure of the hybrid platinum oligoiodide material

$(GUA)_8(PtI_6)_3[PtI_4(I_3)_2]\bullet 2I_2$ is presented in Figure 5.4, with relevant crystallographic data in Table 5.2. Figure 5.4 (a) shows the structure of $(GUA)_8(PtI_6)_3[PtI_4(I_3)_2]\bullet 2I_2$ with organic cations omitted for clarity emphasizing the observed secondary I···I bonding network. Secondary I···I bonds are interactions that are often seen in oligoiodide networks, and occur at distances between the previously mentioned cutoff for I–I covalent bonds, 3.30 Å, and the I···I van der Waals distance, 3.9 Å.[148] In $(GUA)_8(PtI_6)_3[PtI_4(I_3)_2]\bullet 2I_2$ there are three crystallographically independent Pt sites, each with distinct local enviornments. These three Pt octahedral enviornments are denoted in Figure 5.4 (a) and (b) with differing colors as well as bolded numbers (**1**–**3**) which coincide with the .cif file Pt label assignments. **1** refers to the $[PtI_6]^{2-}$ octahedra that have no close I···I secondary bonding associations, **2** to the $[PtI_6]^{2-}$ octahedra that have two close secondary I···I bonding associations with I_3 ligands of the $[PtI_4(I_3)_2]^{2-}$ moieties, and **3**, which refers to the $[PtI_4(I_3)_2]^{2-}$ moieties. The species **3**, in addition to forming secondary I···I bonding associations with **2**, also forms secondary bonds with I_2 molecules in the ab-plane. Figure 5.4 (b) illustrates one such secondary-bonding chain that forms between **3** and **2**, with bond lengths of the I_3 subunit (3.12 Å and 2.80 Å) from species **3** denoted, and is also depicted in Figure 5.5(b). The occurance of **3** is quite interesting, because to our knowledge, no similar Pt or other metal based moietry has been reported to date. As can be seen, the labeled bond lengths are reminiscent of other asymmetric I_3^- anion bonds [2.7(1) Å and 3.2(1)],[168] and, as we demonstrate below, the Raman spectrum displays signatures of the I_3 subunit. Figure 5.5 breaks down the secondary iodide bonding framework into planes in more detail.

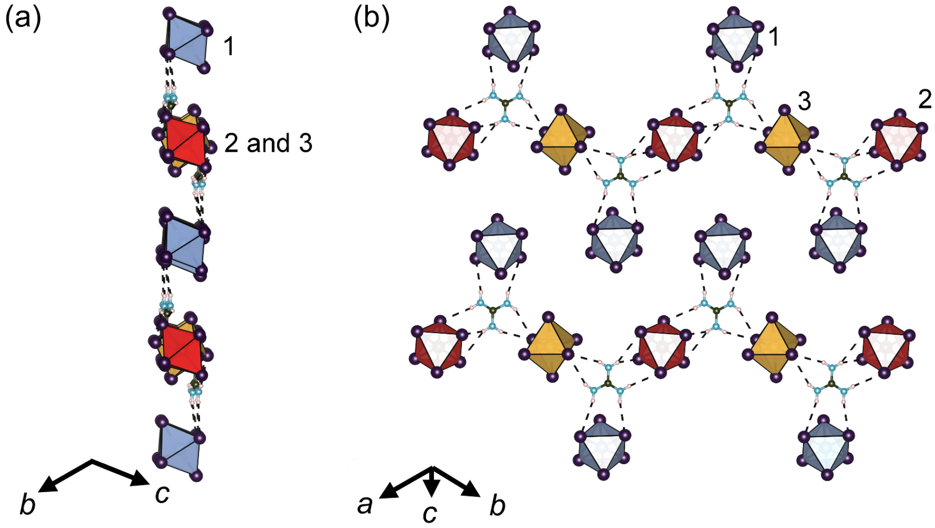

Figure 5.6: View of the hydrogen bonding network that forms between GUA1 and **1**, **2**, and **3**. The hydrogen bonding that occurs between GUA1 and **3** occurs between two of the four equitorial I^-, not any of the I atoms of the I_3 moiety, which is excluded for clarity.

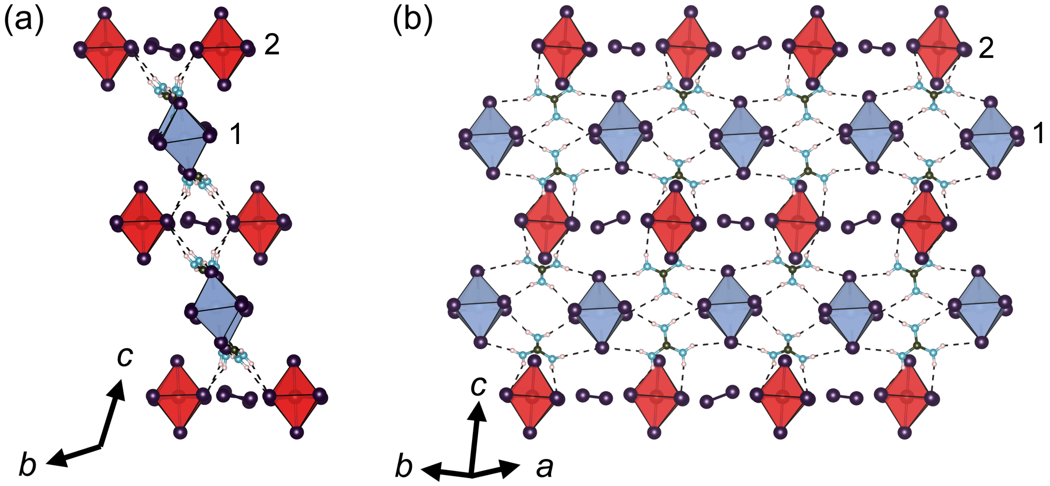

Figure 5.7: View of the hydrogen bonding network that forms between GUA2/GUA4 and the Pt species, **1** and **2**. This network illustrates that even though **1** and **2** are not linked via a secondary iodide bonding network, that they are extensively coupled via the hydrogen bonding network.

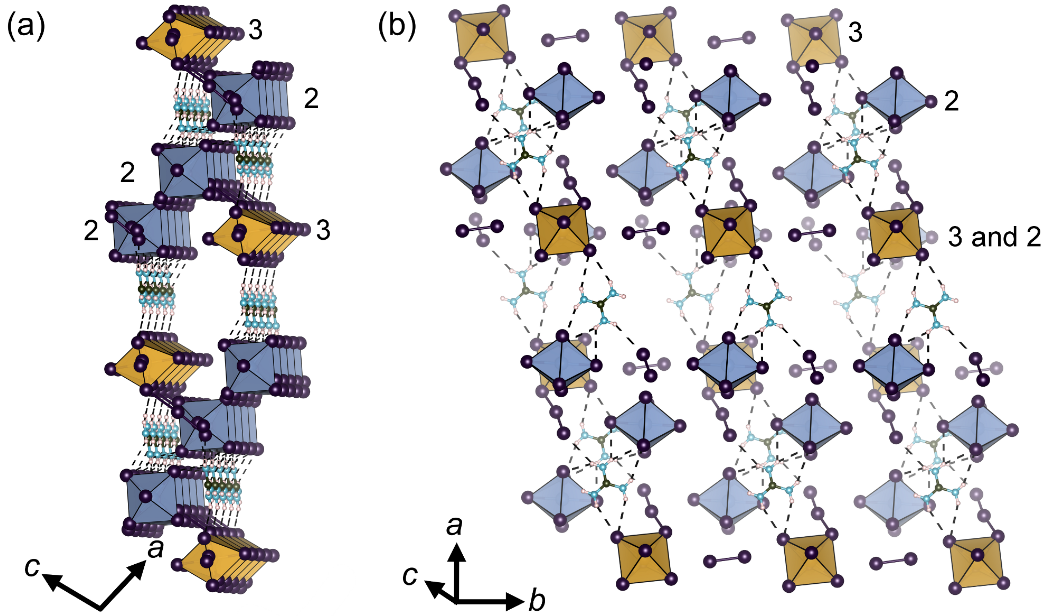

Figure 5.8: View of the hydrogen bonding network that forms between GUA3, and the Pt species, **1** and **3**. GUA3 forms one hydrogen bond with the terminal I atom of the I_3 moiety.

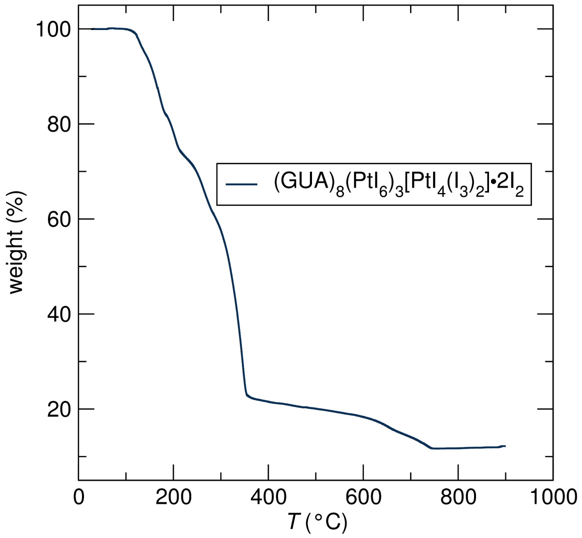

Figure 5.9: TGA data for $(GUA)_8(PtI_6)_3[PtI_4(I_3)_2]{\bullet}2I_2$ from room temperature to 900°C.

Figures 5.6 – 5.8 describe the complex and extensive hydrogen bonding network of the GUA cations in $(GUA)_8(PtI_6)_3[PtI_4(I_3)_2]{\bullet}2I_2$, which hydrogen bond almost exclusively with $[PtI_6]^{2-}$ octahedra iodides. Each of the four crystallographically independent GUA cations connect **1**, **2**, and **3** together, each in a distinct way, but with uncanny similarity to the GUA cations in its parent compound, $(GUA)_2PtI_6$. This suggests that in addition to the secondary iodide network, the hydrogen bonding network is a considerable structural stabilizer. The following figures illustrate the proposed hydrogen bonding network that exists in $(GUA)_8(PtI_6)_3[PtI_4(I_3)_2]{\bullet}2I_2$. Due to the overall small contribution to the SXRD dataset that the N and C atoms provide, it is difficult to say that the reported GUA cation positions are definitive. *However*, the hydrogen bonding network that forms using the anisotropic positions of the N atoms and their respective H atoms, looks uncannily similar to the network seen in the parent compound of $(GUA)_8(PtI_6)_3[PtI_4(I_3)_2]{\bullet}2I_2$, $(GUA)_2PtI_6$. Namely, each of the six hydrogens of the GUA cations point towards nearby I^- on $[PtI_6]^{2-}$ octahedra. In order to deconstruct this complex network of hydrogen bonding, Figures 5.6–5.8 describe the suspected hydrogen bonding network formed by the four crystallographically distinct GUA cations, referred to as GUA1 through GUA4. Interestingly, unlike the hydrogen bonding network that forms in $(FA)_2PtI_6{\bullet}2I_2$, the proposed network exists exclusively with $[PtI_6]^{2-}$, except for the GUA3 cation (Figure 5.8) which bonds with one of the I_3 molecules. The network has been drawn with a $H\cdots I$ maximum of 3.3 Å, so as to account for other favorable, yet weaker, hydrogen bonding positions of the GUA cations. Much like $(FA)_2PtI_6{\bullet}2I_2$, the TGA of $(GUA)_8(PtI_6)_3[PtI_4(I_3)_2]{\bullet}2I_2$ shows stability above 100 °C, suggesting that the secondary iodide network and hydrogen bonding are structurally stabilizing forces (Figures 5.9).

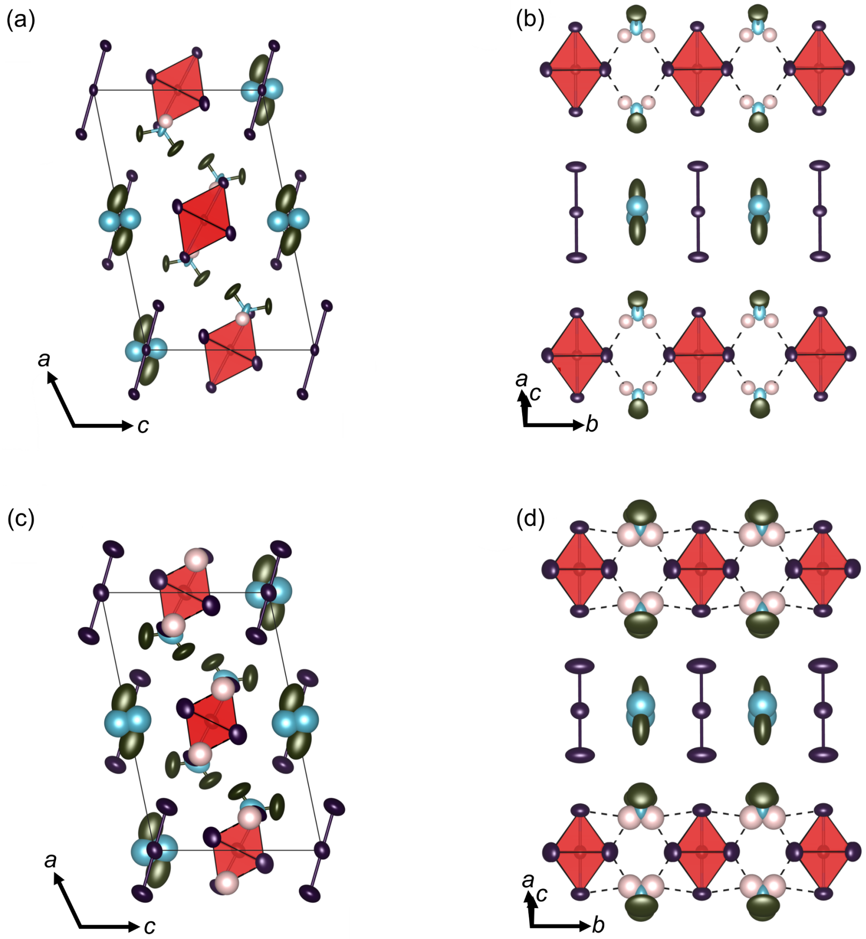

Figure 5.10: Crystal structure of $(\mathrm{DMA})_3\mathrm{PtI}_6(\mathrm{I}_3)$ at 100 K [(a) and (b)] and 264 K [(c) and (d)] with displacement ellipsoids (95% probability). (a) View of $(\mathrm{DMA})_3\mathrm{PtI}_6(\mathrm{I}_3)$ down the b-axis. (b) View of $(\mathrm{DMA})_3\mathrm{PtI}_6(\mathrm{I}_3)$ depicting the hydrogen bonding interactions between DMA cations and $[\mathrm{PtI}_6]^{2-}$ octahedra, as well as the arrangement of I_3^- anions relative to the nearby $[\mathrm{PtI}_6]^{2-}$ octahedra. The distance between apical $[\mathrm{PtI}_6]^{2-}$ iodides and nearby I_3^- is 3.49 Å. (c) View of $(\mathrm{DMA})_3\mathrm{PtI}_6(\mathrm{I}_3)$ down the b-axis. (d) View of $(\mathrm{DMA})_3\mathrm{PtI}_6(\mathrm{I}_3)$ depicting the hydrogen bonding interactions between DMA cations and $[\mathrm{PtI}_6]^{2-}$ octahedra, as well as the arrangement of I_3^- anions relative to the nearby $[\mathrm{PtI}_6]^{2-}$ octahedra. The distance between apical $[\mathrm{PtI}_6]^{2-}$ iodides and nearby I_3^- is 3.56 Å.

Table 5.3: Crystallographic information for (DMA)$_3$PtI$_6$(I$_3$), 100 K and 300 K

Empirical Formula	$[NH_2(CH_3)_2]_3PtI_6(I_3)$	
Crystal habit, color	block, black	
Crystal system	monoclinic	monoclinic
Space group (#)	$C2/m$ (12)	$C2/m$ (12)
Volume (Å^3)	1342.5(1)	1414.3(3)
T (K)	100	264
a (Å)	16.768(9)	17.012(2)
b (Å)	7.666(4)	7.8309(9)
c (Å)	10.656(6)	10.837(2)
α (°)	90	90
β (°)	101.46(2)	101.705(8)
γ (°)	90	90
Z	2	2
ρ (g mol^{-1})	1475.47	1475.47
Dens. (g cm^{-3})	3.650	3.465
Abs. (mm^{-1})	15.570	14.779
F_{000}	1272	1272
Reflections (unique)	3470 (2107)	4293 (2297)
R_{int}	0.0980	0.1329
R_1	0.0634	0.0580
wR_R	0.1348	0.0791
∂F ($e\mathring{A}^{-3}$)	3.384 & -5.871	3.407 & -1.727
GOF	1.062	1.533

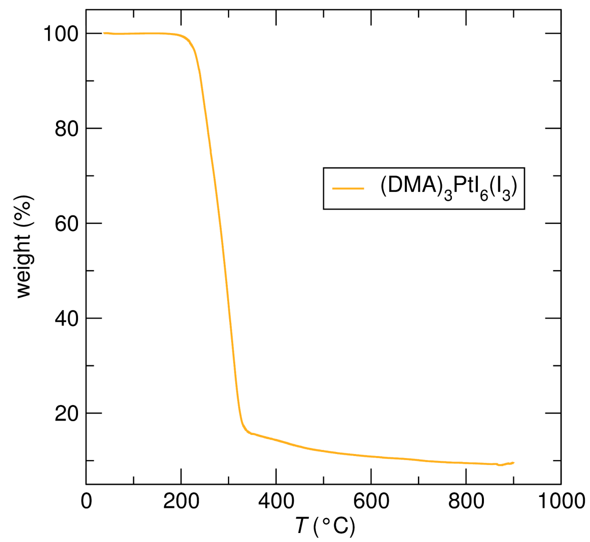

Figure 5.11: TGA data for $(DMA)_3PtI_6(I_3)$ from room temperature to 900°C.

The structures of $(DMA)_3PtI_6(I_3)$ at 100 K and 264 K are presented in Figure 5.4, with relevant crystallographic data in Table 5.3. Figure 5.4 (a) and (c) show the arrangement of $[PtI_6]^{2-}$ octahedra, I_3^- moieties, as well as the two distinct types of DMA cations; one that is ordered and one that is not. Hydrogen atoms are included on the ordered DMA cations to emphasize their role in stabilizing the structure through hydrogen bonding. Figure 5.4 (b) and (d) show this hydrogen bonding, where the N–H$\cdots$I hydrogen bond lengths are at a distance of 2.87 Å and N to I distances are 3.68 Å; these are considered to be medium/strong interactions based on previous neutron diffraction studies.[145] The I_3^- moieties are aligned with the $[PtI_6]^{2-}$ octahedra at a distance of 3.49 Å (secondary I$\cdots$I bonding).[148] Initially, we sought to make a DMA-containing

A_2PtI_6 compound to juxtapose the materials $(FA)_2PtI_6$ and $(GUA)_2PtI_6$. We believed this $(DMA)_2PtI_6$ compound, with a cation roughly the size of FA but with less than half the hydrogen bonding sites, would better inform us as to the impact of hydrogen bonding in these halide materials. It was our intention to recrystallize this hypothetical $(DMA)_2PtI_6$ compound and observe the differences in I_2 inclusion. However, the $(DMA)_2PtI_6$ compound could not be isolated, and only the compound, $(DMA)_3PtI_6(I_3)$, formed. Though not our original intention, this raises a significant question: ”Why did $(DMA)_2PtI_6$ not form?” In the previous chapter (Chapter 4, and our published report,[159] we discussed how the substantial hydrogen bonding capacity of the FA and GUA moieties engaged as structural guides. We believe that the similar size but reduced hydrogen bonding capacity of the DMA cation (compared to the FA cation) serves as a prime example to the significance of hydrogen bonding in these lower dimensional halide materials. Namely, that without a cation that can form numerous attractive $H\cdots I$ interactions, the electrostatic forces between cation and anion are not sufficient to stabilize a A_2PtI_6 molecular salt.

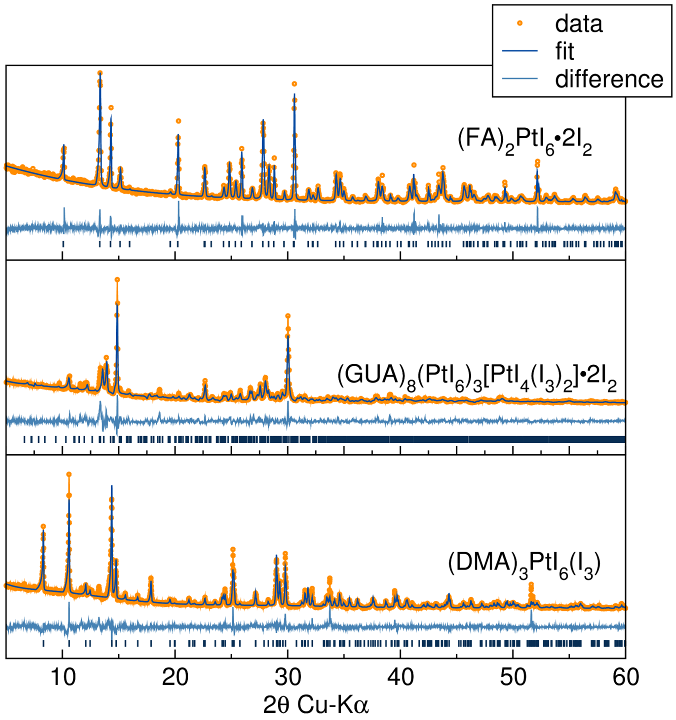

Figure 5.12: Rietveld refinements of the $(FA)_2PtI_6{\bullet}2I_2$, $(GUA)_8(PtI_6)_3[PtI_4(I_3)_2]{\bullet}2I_2$, and $(DMA)_3PtI_6(I_3)$.

Material purity for further characterization was established via Rietveld refinement (without atomic occupancy), with experimental laboratory PXRD data refined against room temperature single crystal diffraction data (Figure 5.12). The refinements indicate that the each bulk sample has unit cell parameters close to single crystal diffraction dimensions (Table 5.4 refined data, Tables 5.1 through 5.3 for single crystal data).

Table 5.4: Refined lattice parameters of $(FA)_2PtI_6{\bullet}2I_2$, $(GUA)_8(PtI_6)_3[PtI_4(I_3)_2]{\bullet}2I_2$, and $(DMA)_3PtI_6(I_3)$.

Forumla	$(FA)_2PtI_6{\bullet}2I_2$	$(GUA)_8(PtI_6)_3[PtI_4(I_3)_2]{\bullet}2I_2$	$(DMA)_3PtI_6(I_3)$
a (Å)	12.402	12.683	17.030
b (Å)	12.402	13.045	7.840
c (Å)	7.865	14.628	10.841
α (°)	90	109.54	90
β (°)	90	102.81	101.75
γ (°)	90	94.11	90

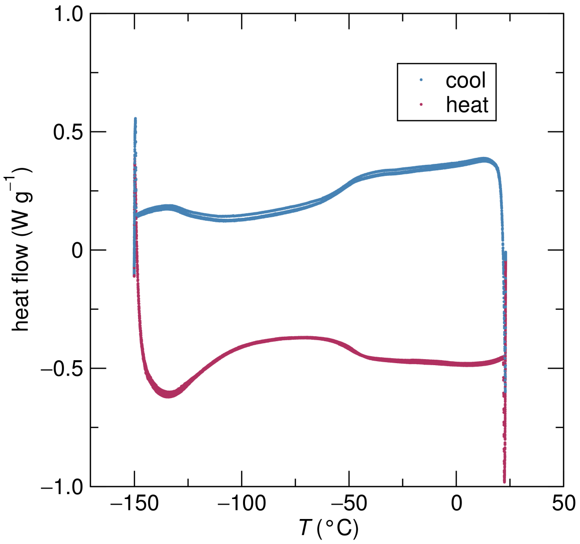

Figure 5.13: DSC data for $(FA)_2PtI_6{\bullet}2I_2$ between $-150\,^{\circ}C$ and $25\,^{\circ}C$.

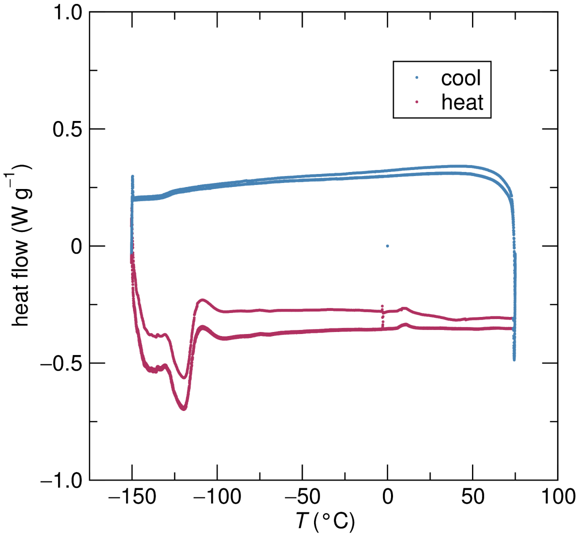

Figure 5.14: DSC data for $(GUA)_8(PtI_6)_3[PtI_4(I_3)_2]\bullet 2I_2$ between −150 °C and 75 °C.

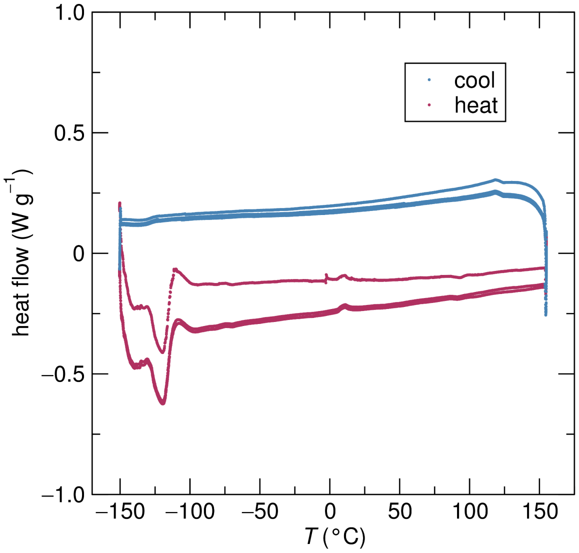

Figure 5.15: DSC data for $(DMA)_3PtI_6(I_3)$ between −150 °C and 150 °C.

Differential scanning calorimetry of $(FA)_2PtI_6\bullet 2I_2$, $(GUA)_8(PtI_6)_3[PtI_4(I_3)_2]\bullet 2I_2$, and $(DMA)_3PtI_6(I_3)$ are presented in Figures 5.13 - 5.15. All materials display no observable first order phase transition.

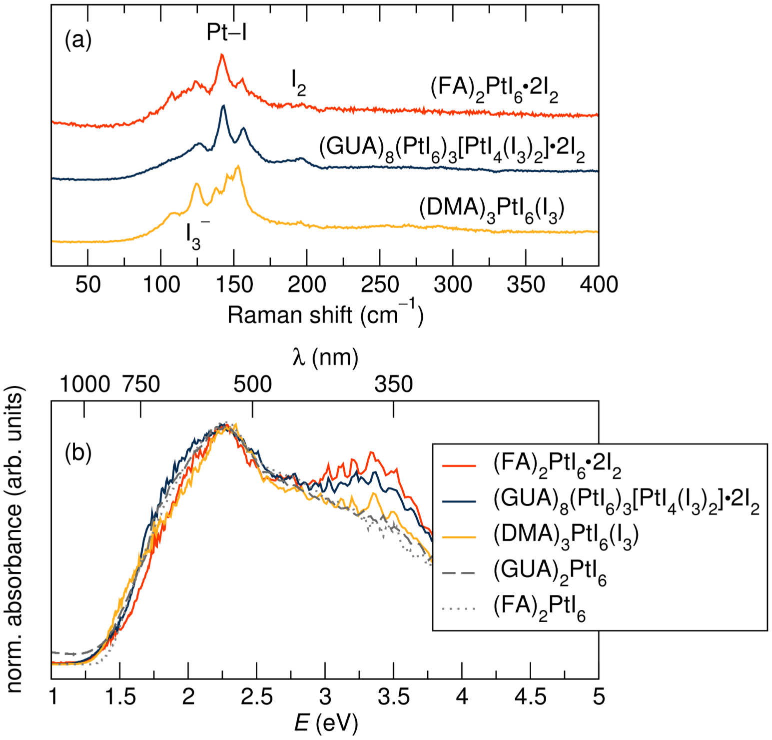

Figure 5.16: (a) Raman spectra of the poly/oligoiodide materials. (b) Normalized optical absorption spectra (following Kubelka-Munk transformation of diffuse reflectance spectra) for the poly/oligoiodide materials. The spectra of the parent compounds $(FA)_2PtI_6$ and $(GUA)_2PtI_6$ are included for comparison.

Raman spectra illustrate the I–I bonding character of these compounds, and are presented in Figure 5.16 (a). Two $[PtI_6]^{2-}$ octahedron Pt–I vibrations of varying strengths can be seen at 141 cm^{-1} and 156 cm^{-1} in all samples tested.[169] The other vibrations of interest are near 125 cm^{-1} and 180cm^{-1}, which are attributed to the vibrations of I_3^- and I_2, respectively.[148] When classifying the polyiodide character of $(FA)_2PtI_6{\bullet}2I_2$, the absence of a strong I_2 vibration near 180 cm^{-1} is quite telling, as this vibration will shift to lower energies if the I_2 molecule is acting as an acceptor. The amount of shift will depend on the strength of the respective donor species.[170] It is likely that for $(FA)_2PtI_6{\bullet}2I_2$, the I_2 vibration has shifted to lower energies near 110 cm^{-1}, which is frequently seen in spectra of extended polyiodides.[148, 150] This suggests that even at room temperature (where the I_2–I^- distance is slightly greater than 3.3 Å) this material is best thought of as a polyiodide. The material $(GUA)_8(PtI_6)_3[PtI_4(I_3)_2]{\bullet}2I_2$, which has both I_2 molecules as well as I_3^- moieties, displays an expected Raman spectrum with vibrations at both 180 cm^{-1} and 125 cm^{-1}. For $(DMA)_3PtI_6(I_3)$, the expected I_3^- vibration near 125 cm^{-1} is present, in addition to a peak near 110 cm^{-1} that is seen in Raman spectra of longer chain oligoiodides,[148] and 140 cm^{-1}, which is seen in Raman spectra for symmetric I_3^- containing compounds.[171] In this respect, both $(GUA)_8(PtI_6)_3[PtI_4(I_3)_2]{\bullet}2I_2$ and $(DMA)_3PtI_6(I_3)$ are best considered oligoiodide networks.

The optical absorption spectra of the three new poly/oligoiodide compounds, as well as their parent compounds, are presented in Figure 5.16 (b). We observe similar optical properties for all materials tested, as was previously observed for the A_2PtI_6 series.[159] For these platinum based compounds, the charge-transfer absorption of the $[PtI_6]^{2-}$ moieties dominates, regardless of structure. However, one clear difference is the increased absorption in the higher energy (2.5 eV – 3.75 eV) of the spectra of $(FA)_2PtI_6{\bullet}2I_2$ and $(GUA)_8(PtI_6)_3[PtI_4(I_3)_2]{\bullet}2I_2$. This increased absorption is caused by the higher-energy states of the I_2 molecules that lie above the platinum d e_g states. The band structure of $(FA)_2PtI_6{\bullet}2I_2$ displays the typical underestimation of band gap when compared with experiment.†

Figure 5.17 (a) displays the electron localization function (ELF) around iodine atoms and ions in $(FA)_2PtI_6{\bullet}2I_2$, projected on the structure, on the plane that contains the infinite polyiodide chains. The lone pair lobes around the I_2 units are arranged axially along I^-–I_2–I^-, suggesting potential covalency in the interaction with the lone pairs on the I^- anions. Significant differences in the shape of the localization between the apical iodides of the $[PtI_6]^{2-}$ octahedra, and the four equatorial iodides not a part of the 1D polyiodide chain, are also seen, suggesting that the apical iodides are indeed involved in some degree of bond formation within this 1D chain. Furthermore, we present the electrostatic potential for $(FA)_2PtI_6{\bullet}2I_2$ in Figure 5.18 showing subtle evidence of σ-holes on the I_2 molecules.† Given the appropriate angle and direction of the I–I$\cdots$I and N–H$\cdots$I bonds and the possible σ-hole, there is potential for halogen bonding stabilizing the observed structure of $(FA)_2PtI_6{\bullet}2I_2$.

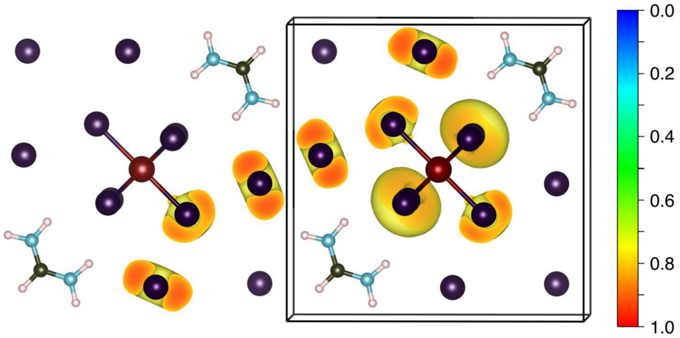

Figure 5.17: Crystal structure of $(FA)_2PtI_6{\bullet}2I_2$ depicted in the plane containing the infinite polyiodide chains. The ELF is displayed for an isosurface value of 0.8, showing the lone pairs around select iodide ions and I_2 moieties.

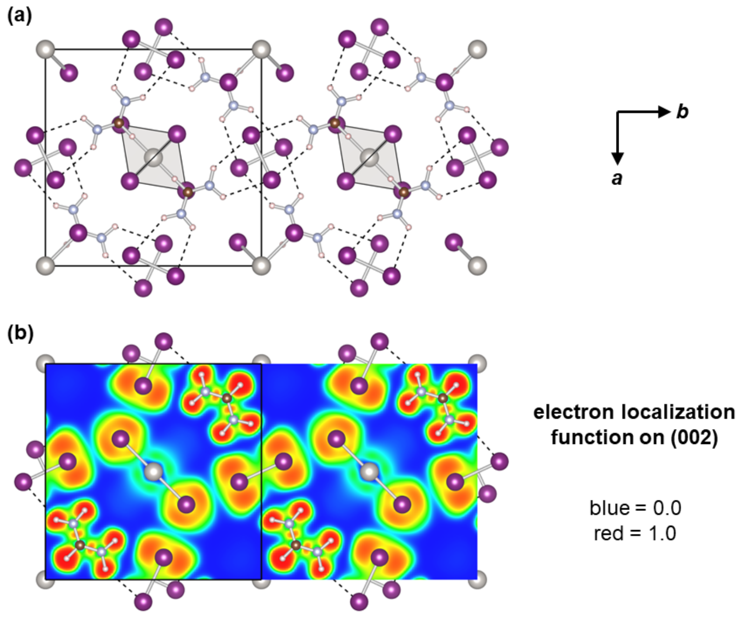

(c) electrostatic potential on (valence) charge density isosurface

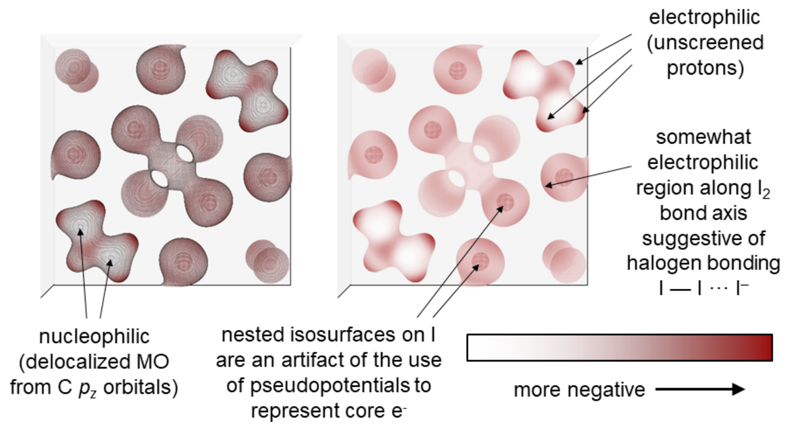

Figure 5.18: (a) The crystal structure of $(FA)_2PtI_6{\bullet}2I_2$, (b) the electron localization function, and (c) the electrostatic potential visualized on isosurfaces of the valence charge density for $(FA)_2PtI_6{\bullet}2I_2$. The color legend indicates the degree of negative electrostatic potential.

In conclusion, we have presented three new hybrid platinum iodide compounds that emphasize the tendency of iodine and iodide to catenate, even when the iodide is part of a complex anion. Hydrogen bonding appears to play a role in stabilizing the observed structures.

Chapter 6

Infinite polyiodide $I_\infty^{\delta-}$ chains in the pyrroloperylene-iodine complex: Insights into the starch-iodine and perylene-iodine complexes

In this chapter, we describe the preparation and X-ray crystallographic characterization of the first crystalline homoatomic iodine polymer chain, $I_\infty^{\delta-}$, which is part of a semiconducting pyrroloperylene-iodine complex. Interestingly, the

---

[1] Sheri Madhu, Vicky V. T. Doan-Nguyen, John G. Labram, Guang Wu, Michael L. Chabinyc, Ram Seshadri, and Fred Wudl have contributed to the contents of this chapter.

structure of iodine within the insoluble, blue starch-iodine complex has long remained elusive, but has been speculated as having infinite chains of I. Close similarities in the low-wavenumber Raman spectra of the pyrroloperylene-iodine and starch-iodine compounds point to such infinite polyiodide chains in the latter as well.

Previous publication of this data can be found in *Angewandte Chemie International Edition*, © 2016 John Wiley & Sons, Inc., reprinted with permission.

> Sheri, M.; Evans, H. A.; Doan-Nguyen, V. T.; Labram, J. G.; Wu, G.; Chabinyc, M. L.; Seshadri, R.; Wudl, F. Infinite polyiodide $I_\infty^{\delta-}$ chains in the pyrroloperylene-iodine complex: Insights into the starch-iodine and perylene-iodine complexes, *Angew. Chem. Int. Ed.* **2016**, *55*, 8032 – 8035.

6.1 Introduction

According to Saenger,[172] the starch-iodine complex was discovered by Colin and de Claubry over two hundred years ago.[173] The complex is better described as amylose-iodine[172] and has continuously, over the years, been considered as a clathrate of polyiodide and carbohydrate. The nature of the polyiodide in this complex still remains to be fully characterized, and many of the references on iodine chain-containing compounds in the literature draw analogies with the elusive starch-iodine structure. For example, Kahr *et al.*[174] established the crystal structure of so-called herapathite: a quinine-iodine complex with iodide trimers. Redel *et al.*[175] have reported a complex copper iodide with chains of up to five iodine atoms. Lin *et al.*[176] have reported bent anionic I_7^- chains stabilized by complex multivalent organic ammonium cations. Schröder and coworkers[177] have reviewed the rich structural chemistry that emerges when macrocylic thioethers are employed to stabilize oligomeric iodine chains. Yin *et al.*[178] have reported a metal-organic framework based on Cu(II) cations and I_5^- and I_7^- chains. Kloo *et al.*[179] have also employed ab-initio techniques to study the structure and stability of short $I_n^{\delta-}$ moieties in the vacuum. These descriptions of iodide chains, as well as numerous others, are better described as oligomeric rather than polymeric chains of iodine, with lengths typically shorter than ten iodine units and usually containing molecular iodine within the chain.[148] Indeed, a seminal resonance Raman spectroscopic study of the starch-iodine complex carried out in 1978 led the authors to infer the presence of predominantly I_5^- species.[180]

A separate and highly relevant structural mystery involving iodine is that of one of the earliest organic electronic conductors, the perylene-iodine charge transfer complex,[181] which to this day not been fully resolved. It is clear that the hydrocarbon is partially oxidized and the iodine shows hints of iodine and triiodide[182] but the latter are disordered in essentially all examined cases.

In this chapter we relate both stories and shed light on the science of these functional organic materials. We have determined the structure of a pyrroloperylene-iodine complex that comprises helical, infinite iodine chains interspersed between π-stacks of pyrroloperylene cations. The electrical conductivity of this compound is found to be close to $10^2\,\mathrm{S\,cm^{-1}}$ at room temperature, and a change in the temperature coefficient of the conductivity at temperatures close to 150 K is suggested as corresponding to a structural transition. Based on similarities between the published low-frequency Raman spectroscopic signatures of starch-iodine complex and the spectrum measured on the pyrroloperylene-iodine compound, it is suggested that the starch-iodine complex must similarly comprise infinite iodine chains.

6.2 Experimental details

The preparation of pyrroloperylene and the pyrroloperylene-iodine complex was performed by Dr. Sheri Madhu.

Perylene and triethyl phosphate were used as obtained from Sigma Aldrich. All other chemicals used for the synthesis were reagent grade. Solvents were dried by routine procedures immediately before use. Column chromatography was performed on silica gel (60 to 120 mesh).

Synthesis of 1-nitroperylene (**2**):[183, 184] To a hot solution of perylene (5.0 g, 19.8 mmol) dissolved in 1,4-dioxane (200 mL) was added a mixture of 5.0 mL of water and 4.5 mL of nitric acid (d = 1.5) dropwise while stirring. The resulting solution was heated at 60°C with vigorous stirring for 30 min, and the initial yellow solution completely turned to brick red color. The reaction mixture was cooled and transferred into 1 L of water. The solid was filtered, dried under vacuum, and purified by column chromatography on silica gel with hexane/toluene (75/25) as eluent to afford 2 as a brick-red crystal. Yield (1.77 g, 30%). 1H NMR (DMSO, 600 MHz): δ=8.56 (dd, 2H), 8.02–7.95 (m, 4H), 7.83 (d, J=8.4 Hz, 1H), 7.77 (dd, 2H), 7.69 (t, J= 7.6 Hz, 1H), 7.59 ppm (t, $J = 8.0$ Hz, ^{1}H). EI-MS, m (%), 297 (M^+, 100%).

Synthesis of pyrroloperylene or 6H-phenanthro [1,10,9,8-c,d,e,f,g] carbazole (**3**):[183, 184] A mixture of 0.50 g (1.7 mmol) of 1-nitroperylene (**2**) and 5 ml of triethyl phosphite was heated at reflux under argon for 2 hr. Upon cooling the reaction mixture to room temperature, the yellow brown amine **3** crystallized and crystals were collected by filtration. Yield (0.38 g, 85%). ^{1}H NMR (DMSO, 600 MHz, δ ppm): 12.20 (s, 1H), 8.74 (d, $J = 8.2$ Hz, 2H), 8.19 (d, J = 8.4 Hz, 2H), 7.99 (dd, 4H), 7.94 (t, $J = 7.4$ Hz, 2H). ^{13}C NMR (DMSO, 150 MHz): δ =

131.1, 130.2, 128.8, 125.5, 125. 1, 124.7, 121.3, 117.4, 116.0 ppm. EI-MS, m (%), 265 (M^+, 100%).

The preparation of the pyrroloperylene-iodide complex from solution by slow cooling was straightforward, and employed a benzene solution containing 15 mg (0.0566 mmol) of pyrroloperylene **3** and 51 mg (0.198 mmol) of iodine, kept at 65°C in a vial with a screw cap. The solution was allowed to cool slowly from 65°C to 30°C over a period of five days in a doubly insulated container. Shiny needles with a dark yellow-green lustre were obtained in the bottom of the vial. The crystals were found to be quite stable at room temperature under STP conditions, but off-gassed iodine at higher temperature (as seen from the thermogravimetric analysis.) The concentration most favorable for the formation of large (>1 mm) single crystals was 10 mg of pyrroloperylene and 35 mg of iodine per 5 mL benzene solution. The dimensions of these crystals varied in length from 1 mm to 5 mm, the width from 100 μm to 200 μm, and thickness from 10 μm to 50 μm.

Single-crystal X-ray diffraction data acquisition was carried out on a Bruker Kappa APEX II CCD diffractometer with graphite-monochromatized (Mo-$K\alpha = 0.71073$ Å) radiation at a temperature of $T = 100(2)$ K. Data were collected with omega scan width of 0.5° at 3 different settings with exposure time of 15 s keeping the sample-to-detector distance fixed at 60 mm. The X-ray data collection was monitored by the APEX2 program.[185] The data were corrected for Lorentz, polarization and absorption effects using SAINT and SADABS. SHELXTL was used for structure solution and full matrix least-squares refinement on F2.[47] All the H-atoms were placed in geometrically idealized position and constrained to ride on their parent atoms. All crystallographic representations were carried out with VESTA.[48]

The solution ^{1}H and ^{13}C NMR spectra were recorded on a Varian Unity Inova 600 MHz spectrometer and referenced to tetramethylsilane.

The mass spectra were recorded on a Micromass QTOF2 system using electrospray ionization.

Electrochemical measurements were performed with a Princeton Applied Research Potentiostat/Galvanostat model 263A. The electrochemical measurements were carried out in CH_2Cl_2 solution containing 0.1 M tetrabutylammonium hexafluorophosphate (NBu_4PF_6) as the supporting electrolyte, with a platinum disc, platinum wire, and silver wire as the working, counter, and pseudo-reference electrodes, respectively. The ferrocene-ferrocenium (Fc/Fc^+) redox couple was used as an internal standard (4.80 eV below the vacuum level).

Differential scanning calorimetry (DSC) measurements were performed using a TA Q2000 calorimeter. Samples (2 mg to 10 mg each) were hermetically sealed inside TZero aluminum pans.

Thermogravimetric analysis (TGA) was conducted using a TA Instruments Discovery instrument. A rate of 25 cm^3/min dry nitrogen purge was employed with a temperature ramp rate of 10°C/min. The maximum temperature of the experiment was 650°C.

UV-Vis absorption was recorded on an Agilent 8453 spectrophotometer. Luminescence was recorded on a Horiba FluoroMax 4 spectrometer with a Quanta-ϕ integrating sphere.

FTIR was recorded on a Thermoscientific Nicolet iS10 FT-IR Spectrometer with an attenuated total reflectance (ATR) setup.

Room temperature polycrystalline electron spin resonance (ESR) measurement was recorded on Bruker EMXplus Spectrometer in the CW X-Band range.

For electrical transport measurements, a single crystal of the pyrroloperylene-iodine complex was deposited onto a vitreous silica substrate with a hypodermic needle. Using a stereo microscope, a small volume of colloidal silver paste (Pelco) was deposited onto the substrate at each end of the crystal, again using a hypodermic needle. The silver paste was allowed to dry at room temperature in air for 1 h before the sample was transferred to a cryogenic probe station. The chamber was evacuated to a pressure of

1×10^{-4} mbar. The current was then measured as a function of voltage applied across the length of the crystal using a Keithley 2400 SourceMeter. The conductance was extracted from the measured current-voltage characteristics using 3-point differentiation and taking an average across all applied voltages (-2 V to $+2$ V). The conductivity was derived from the conductance by approximating the crystal as a cylinder with a length of 1.2 mm and a diameter of 50 μm, as determined by optical microscopy.

Raman spectroscopy was performed using a Horiba Jobin-Yvon Lab ARAMIS instrument equipped with a 785 nm laser and confocal microscope, equipped with a 10× objective lens. The single crystals were measured using a 400 μm aperture, 400 μm slit, and 1200 gratings per mm, with exposure time of 1 s, averaged 20 times.

6.3 Results and discussion

6.3.1 Perylene and pyrroloperylene characterization

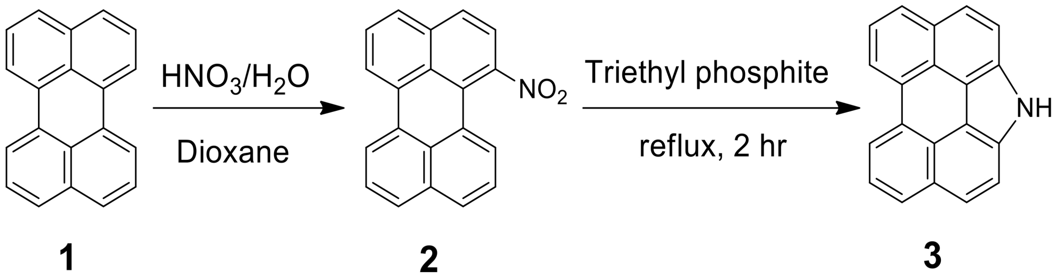

Figure 6.1: Synthetic route for pyrroloperylene **3**.

The synthesis procedure for pyrroloperylene is included in the Experimental Details section of this chapter, and briefly summarized in Figure 6.1.

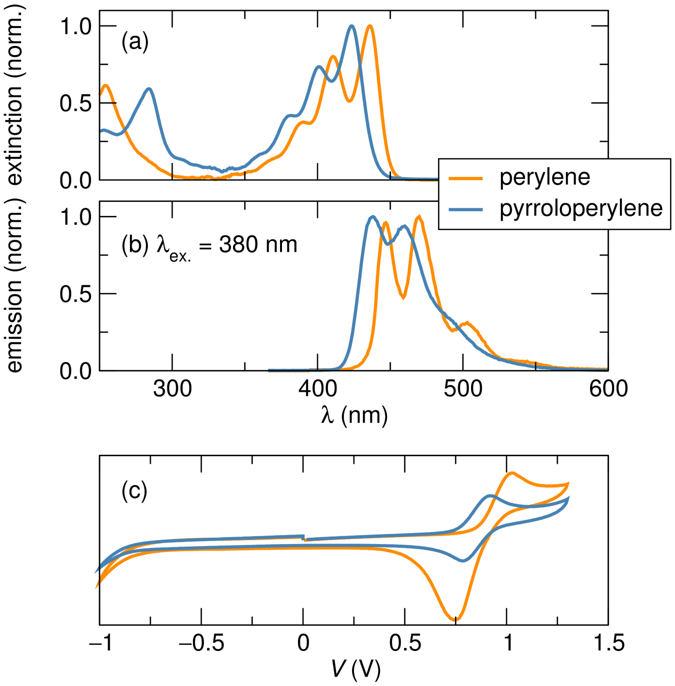

Figure 6.2: (a) Normalized UV-Vis absorption and (b) emission spectra of perylene **1** and pyrroloperylene **3** recorded in CH_2Cl_2 at room temperature. The excitation wavelength in (b) was 380 nm. There is a notable blue shift on going from **1** to **3**. (c) Cyclic voltammogram of perylene **1** and pyrroloperylene **3** recorded in CH_2Cl_2 with 0.1 M NBu_4PF_6, supporting electrolyte, at a scan rate of 50 mV s^{-1}.

The absorption and emission spectra of perylene **1** and pyrroloperylene **3**, recorded in CH_2Cl_2 solution, are shown in Figure 6.2(a) and (b) and the relevant data are presented in Table 6.1. The UV-Vis absorption spectrum showed that pyrroloperylene exhibits a well-defined vibronic π–π^* transition absorp-

Table 6.1: Photophysical data for perylene and pyrroloperylene.

Compound	**perylene**	**pyrroloperylene**
absorption peak (nm)	390, 410, 435	381, 402, 422
absorption onset (nm)	460	440, 469
emission peak (nm)	448, 470, 602	438.0, 459.7 491.0
emission onset (nm)	430	420
HOMO (eV)	−5.3	−5.3
LUMO (eV)	−2.6	−2.3

tion band with the longest wavelength maximum at 422 nm, with two vibronic components on the higher energy side at 381 nm and 402 nm respectively. The absorption and emission bands of pyrroloperylene are hypsochromically shifted relative to the corresponding perylene (Table 6.1). At first sight, this result is surprising, since the 22 π-electron pyrroloperylene should be more conjugated than the two-10 π system perylene, and the absorption and emission should be red-shifted. The explanation clearly is that the two naphthalene units of perylene are sufficiently close together that their optical properties are more complex than can be expected from independent naphthalenes. The relative emission spectra of perylene and pyrroloperylene display a similar blue shift. Pyrroloperylene showed two emission bands at 440 nm and 469 nm, respectively.

Cyclic voltammetry (CV) of perylene and pyrroloperylene at a scan rate of $50\,\mathrm{mV\,s^{-1}}$, recorded in CH_2Cl_2 using tetrabutylammonium hexafluorophosphate (0.1 M) as the supporting electrolyte, with platinum as the working electrode and Ag/Ag^+ wire as the reference electrode, is shown in Figure 6.2(c). Compound **3** shows a one-electron reversible oxidation at ca. 0.6 eV vs. Ag/Ag^+, while perylene exhibits a one-electron oxidation under the same conditions at 1 eV. Neither shows a reduction potential under these conditions, although perylene is known to show a reduction wave at −2.1 eV.[186] The presence of the oxidation wave at 0.6 V indicates that pyrroloperylene is a better reducing agent than perylene and hence should produce more stable radical cation salts. The HOMO values, calculated from CV, using a ferrocene-ferrocenium (Fc/Fc^+) redox couple as internal standard (4.80 eV below the vacuum level), for perylene and pyrroloperylene were, ca. −5.3 eV and −5.1 eV, respectively. The LUMO values of perylene and pyrroloperylene calculated using the optical band gap are −2.6 and −2.3 eV, respectively (Table 6.1).

6.3.2 Characterization of the pyrroloperylene-iodine complex

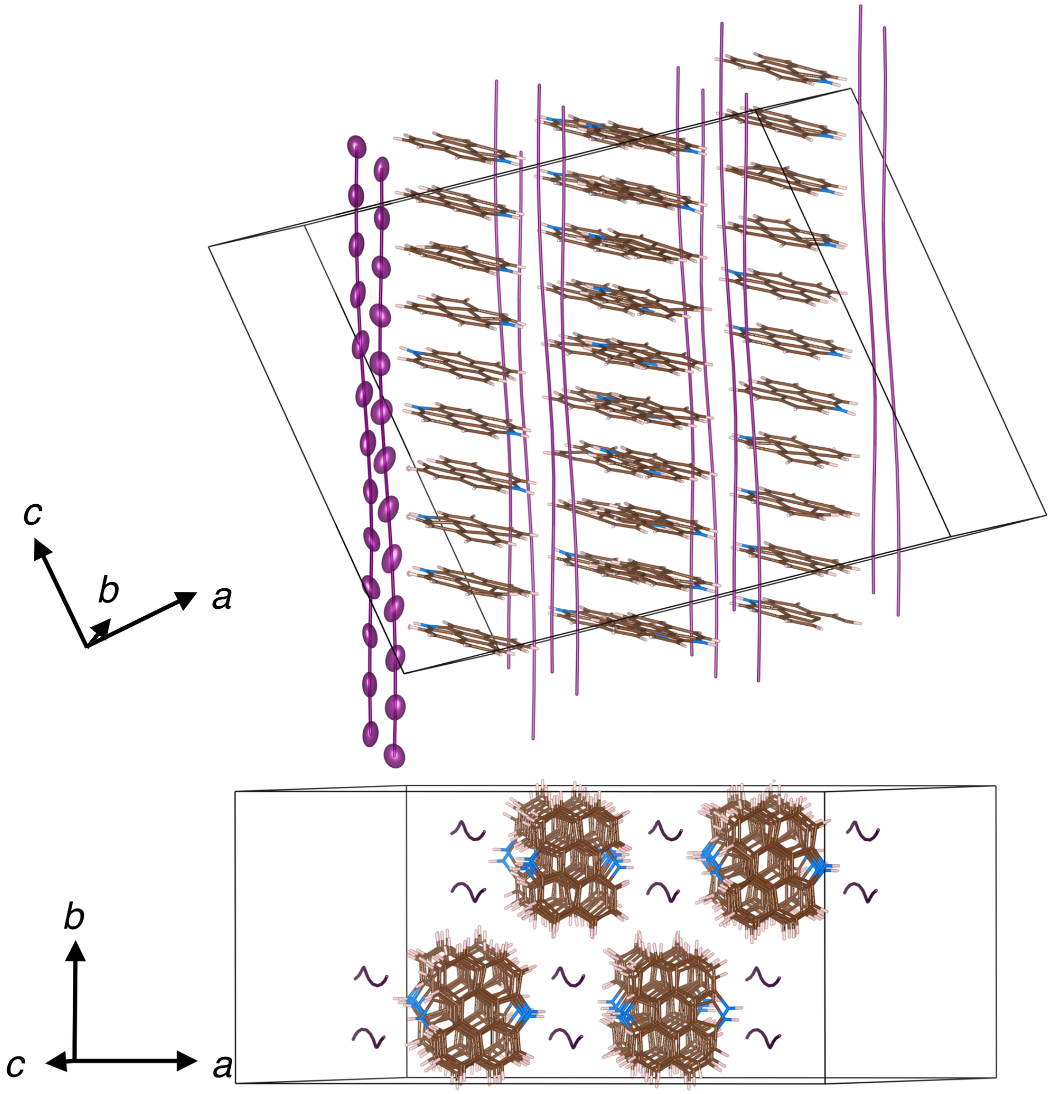

Figure 6.3: Views of the crystal structure of pyrroloperylene-iodine complex at 100 K, showing pyrroloperylene π-stacks separated by racemic pairs of helical chains of $I_{\infty}^{\delta-}$. In the top panel, the 99% probability thermal ellipsoids of I in two of the chains are displayed.

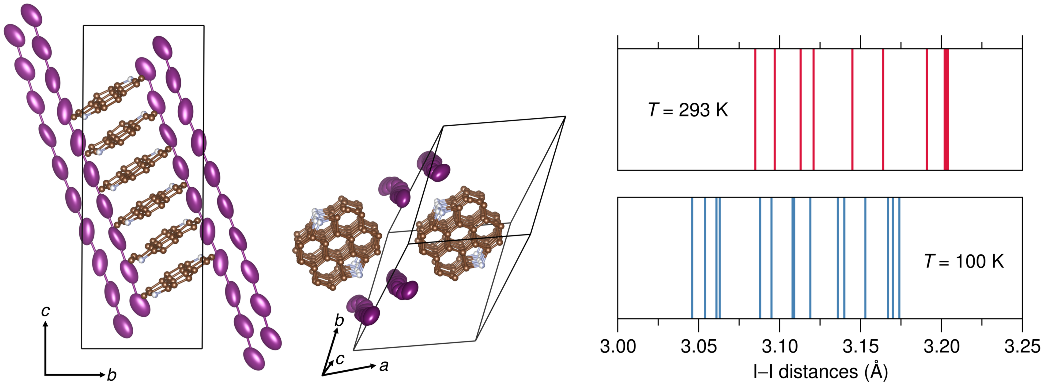

Figure 6.4: Two views of the room-temperature crystal structure of the title compound, showing infinite polyiodide chains (with 10 unique I atoms per chain) interspersed between π-stacked, disordered pyrroloperylene units. The panel on the right displays distributions of I–I distances in the room temperature and 100 K structures of the title compound. Thermal contraction, and the slightly enhanced dispersion in the distances at 100 K are noted.

The crystal structure of pyrroloperylene-iodine complex was solved at 100 K and 300 K, and was refined to a composition of pyrrolloperylene-$I_{2.2}$. The 100 K structure is displayed in Figure 6.3, and the 300 K structure with a histogram comparing iodine-iodine distances at both temperatures is shown in Figure 6.4. The pertinent crystallographic details are listed in Table 6.2.

The structure at 100 K is monoclinic, space group $C2/c$ (No. 15), solved with R_1 = 5.91%. In the crystal structure of the complex, pyrroloperylene exhibits a

Table 6.2: Crystallographic information for the pyrolloperylene-iodine complex, 100 K and 300 K.

Empirical Formula	$C_{130}H_{70.5}I_{14.5}N_{6.5}$	
Crystal habit, color	needle, black-green	
Crystal system	monoclinic	trigonal
Space group (#)	$C2/c$ (15)	$P\bar{1}$ (2)
Volume (Å^3)	1397(1)	3645.8(8)
T (K)	100	300
a (Å)	37.939(7)	11.205(1)
b (Å)	18.507(3)	11.769(2)
c (Å)	29.839(5)	29.992(4)
α (°)	90	86.097(2)
β (°)	101.38(1)	79.655(2)
γ (°)	90	69.571(2)
Z	8	2
ρ (g mol^{-1})	3563.48	3563.48
Dens. (g cm^{-3})	2.305	2.239
Abs. (mm^{-1})	4.430	4.304
F_{000}	13316	2293
Reflections (unique)	66320(20947)	37556(14870)
R_{int}	0.509	0.1271
R_1	0.0591	0.0848
wR_R	0.0893	0.1540
∂F ($e\AA^{-3}$)	1.061 & −1.520	1.428 & −1.896
GOF	0.682	1.180

Table 6.3: Select bond distances in perylene, pyrroloperylene, and the pyrroloperylene-iodine complex.

Compound	bond distance (Å)	
perylene	C1–C2:	1.411
	C4–C9:	1.412
	C8–C11:	1.499
	C10–C19:	1.386
	C17–C18:	1.403
pyrroloperylene	C1–N1:	1.402
	C1–C2:	1.411
	C4–C9:	1.412
	C8–C11:	1.499
	C10–C19:	1.386
	C17–C18:	1.403
pyrroloperylene-iodine complex	C1–N2:	1.405, 1.434
	C1–C2:	1.399
	C4–C9:	1.413
	C8–C11:	1.379
	C10–C19:	1.386
	C17–C18:	1.424

nearly planar molecular conformation with an interplanar distance of 3.47 Å. In the asymmetric unit, one of the pyrroloperylene molecules exhibits disorder of the N atom over two orientations related by the inversion center. The pyrroloperylene stacks are interspersed with polyiodide chains in close proximity, and are parallel to each other. Table 6.3 compares pertinent bond lengths of the organic in the pyrroloperylene-iodine complex, as well as the precursor reagents. The 100 K crystal structure showed the presence of nearly linear polyiodide chains with shallow helicity, and interatomic distances varying from 3.054 Å to 3.174 Å. These I–I distances for the 100 K structure are shown in Figure 6.5. The inter-iodine distances in the chain both in the 100 K and 300 K structure are all greater than 3.00 Å, supporting the conclusion that no neutral I_2 units (interatomic distance: 2.70 Å)[187] are a part of the chains. This implies that all the iodine atoms in the polyiodide chain carry a partial negative charge. So far, with very few exceptions, the geometry of polyiodide chains (I_5, I_7, and I_9) reported in the literature is non-linear,[181] whereas the polyiodide chain found in the pyrroloperylene-iodine complex at 100 K and 300 K is nearly linear.

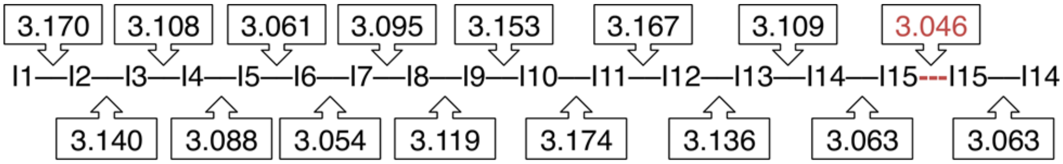

Figure 6.5: Inter-iodine distances in the polyiodide chains determined from the low-temperature (100 K) X-ray crystal structure, in angstroms. The red dashed line and distance of 3.046 Å is the distance between repeats of 14 unique distances between the 15 crystallographically unique iodine atoms in the chains.

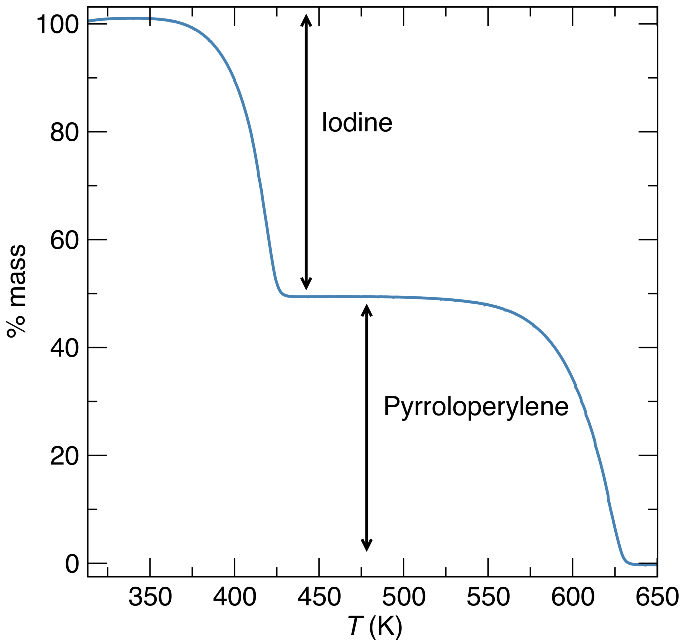

Figure 6.6: TGA of the pyrroloperylene-iodine complex. The samples were run under a 25 ml/min. dry nitrogen purge. The ramp rate was 10 °C/min up to 650°C. The data were acquired using a TA Instruments Discovery TGA system. Weight loss corresponding to volatilization of iodine, followed by complete sublimation of the organic is seen.

Thermogravimetric analysis of the pyrroloperylene-iodine complex is shown in Figure 6.6. The degradation profile shows a two step mass loss, each proportional to 50% of the mass. We believe it is reasonable to assert that iodine is the first component to off-gas from the pyrroloperylene-iodine complex, as iodine is well known to sublimate at room temperature.

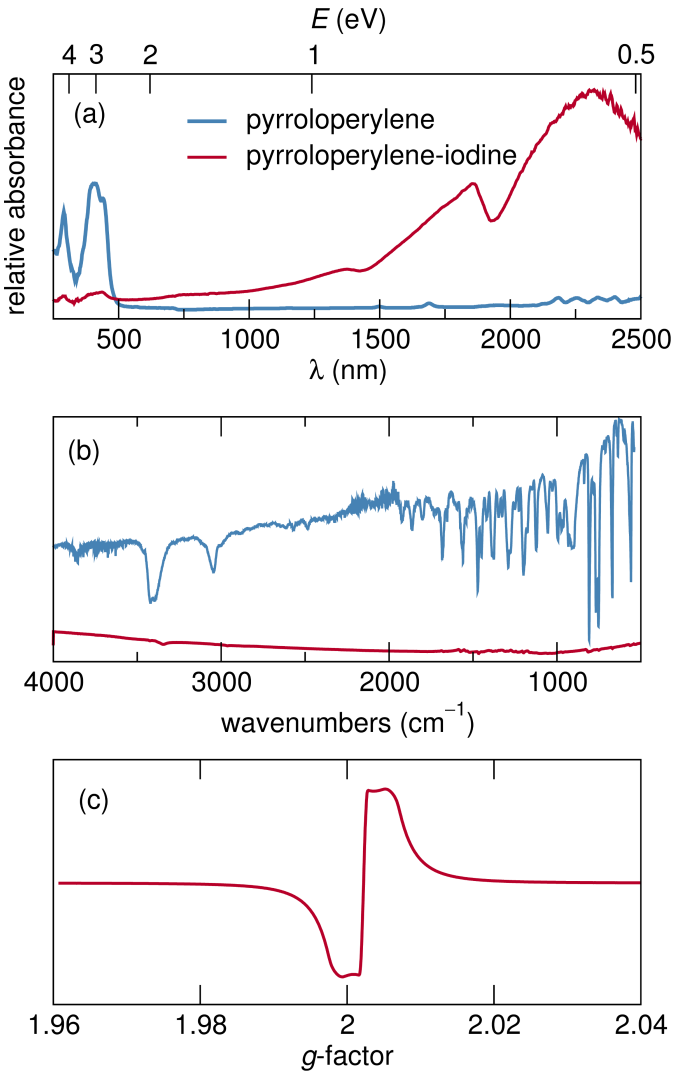

Figure 6.7: Solid state (a) UV-Vis absorption (in $BaSO_4$) and (b) Infrared spectra of the pyrroloperylene and pyrroloperylene-iodine complex. (c) Solid-state ESR spectrum of the pyrroloperylene-iodine complex at room temperature.

The Kubelka-Munk transformation of the diffuse reflectivity of solid pyrroloperylene and the pyrroloperylene-iodine complex, acquired in dispersion in $BaSO_4$ is shown in Figure 6.7(a). The crystals of the pyrroloperylene-iodine complex appear shiny and metallic and with an absorption extending through visible range of the visible region into the near-infrared. This, as well as the feature observed near 1750 nm suggests the presence of free carriers, and is consistent with the electrical transport measurement.[69] Both spectra show identical overlapping bands in the region of 450 nm, which is also seen in the solution spectrum of pyrroloperylene found in the experimental section. Figure 6.7(b) compares the infrared spectra of pyrroloperylene and the pyrroloperylene-iodine complex. The spectrum of the complex is dominated by free charge carriers, starting in the 500 cm^{-1} extending all the way to NIR region. The intramolecular vibrational peaks of pyrroloperylene are very weak and are clearly masked by the free charge carriers in the complex. The presence of these free carriers also influences the line-shape of the room temperature electron spin resonance (ESR) spectrum of the pyrroloperylene-iodine complex, displayed in Figure 6.7(c). The open-shell complex displays an asymmetric signal centered at $g = 2.0022$, with some complex features potentially arising from the powder averaging of a crystalline material.

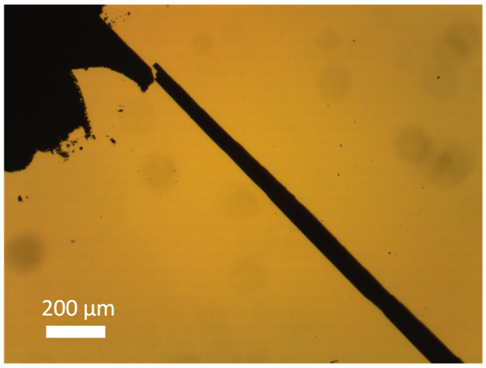

Figure 6.8: Optical microscope image of example pyrroloperylene-iodine single crystal after attempted electrical characterization at cryogenic temperatures (data not shown). The fracture occurred as the temperature was reduced from 300 K to 80 K.

Dr. John Labram examined the electrical properties of four single crystals of the pyrroloperylene-iodine complex. In these experiments, we found some variation in their electrical behavior, attributable to mechanical defects and cracking near the contacts during temperature changes. This is likely to be due to contraction of the crystal, which was suspended between static conformal contacts on a quartz substrate. For this reason, several crystals were slowly reduced to 80 K, a candidate crystal was selected and conductivity measurements were carried out with increasing temperature. Figure 6.8 shows an example of a pyrroloperylene-iodine crystal that fractured during the temperature-dependent measurement process (electrical data not shown). Because of their fragility, we did not attempt four-probe measurements and our electrical data includes effects due to injection at the contacts.

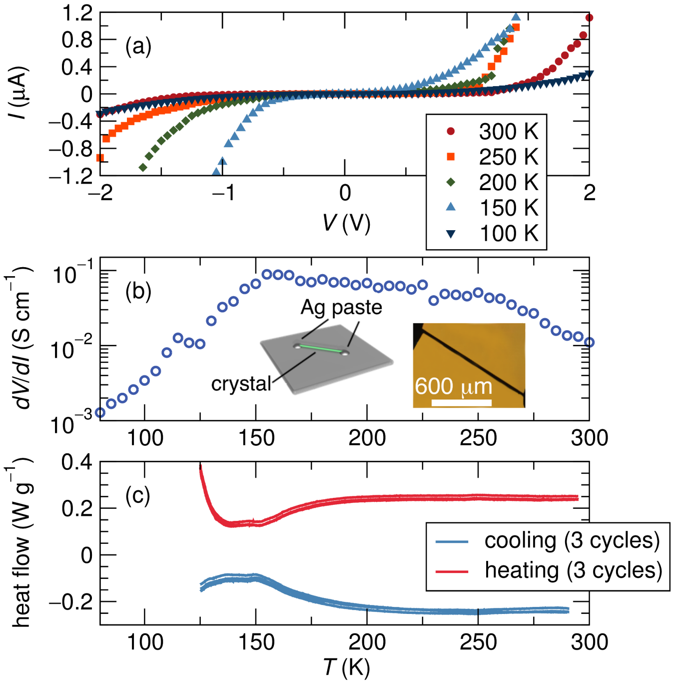

Figure 6.9: (a) Current as a function of voltage applied along the length of a single crystal of pyrroloperylene-iodine complex, measured at various temperatures. (b) Average differential conductivity between −2 V and−1.5 V and between 1.5 V and 2 V, acquired upon forward sweep, as a function of measurement temperature T. The inset displays an optical microscope image of a single crystal on silica. At the edge of the image the silver paste employed to contact the crystal is visible. The crystal was assumed to be cylindrical with a length of 1.2 mm and a diameter of 50 μm. All measurements were carried out under vacuum (10^4 mbar). (c) DSC heating and cooling traces suggesting a highly reproducible incident near 150 K, corresponding to the temperature at which the temperature-coefficient of conductivity changes slope.

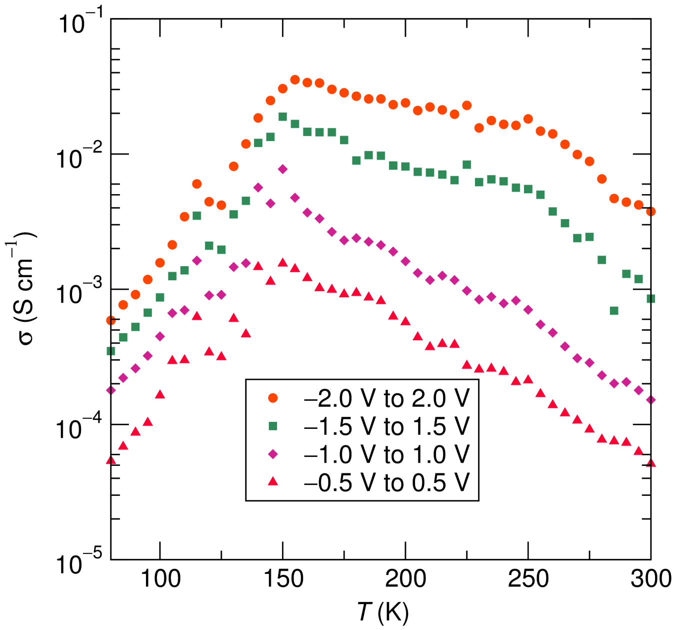

Figure 6.10: Conductivity as a function of temperature obtained by calculating the slope of the I-V traces between the indicated voltages.

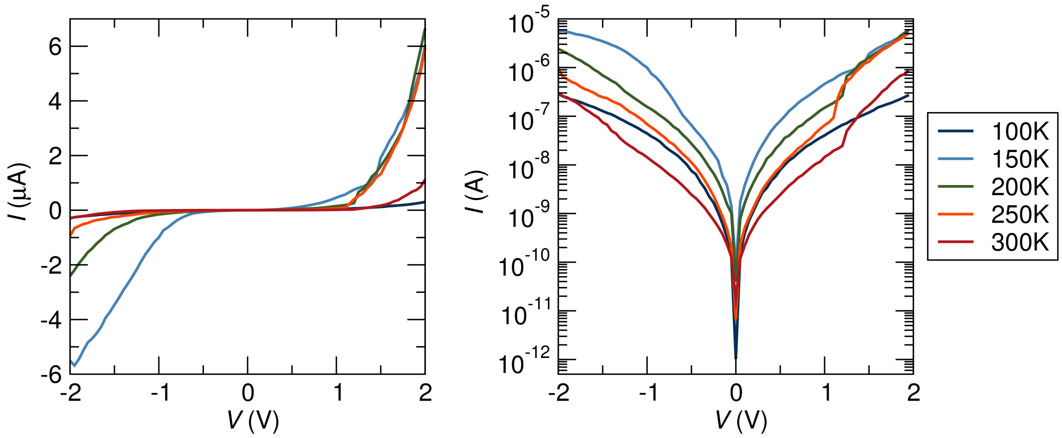

Figure 6.11: Current measured as a function of voltage along the length of the pyrroloperylene-iodine single crystal, at various measurement temperatures, plotted with a linear (left) and logarithmic (right) scale on the y-axis. The crystal was approximately cylindrical in shape and had a diameter and length of approximately 50 μm and 1.2 mm, respectively. Measurements were carried out under vacuum at a pressure of 1×10^{-4} mbar.

A successful measurement of the electrical behavior is shown in Figure 6.9(a) displaying non-linear I-V relationship over the range of applied biases examined. A comparison between other applied biases is shown in Figure 6.10. The differential conductivity (dI/dV) was extracted from the data and shows a ten-fold increase in conductivity from 300 K to $\simeq$150 K across the entire range of applied bias, followed by a significant decrease [Figure 6.9(b)]. There is some asymmetry in the I-V data which we attribute to imperfect contacts (Figure 6.11).

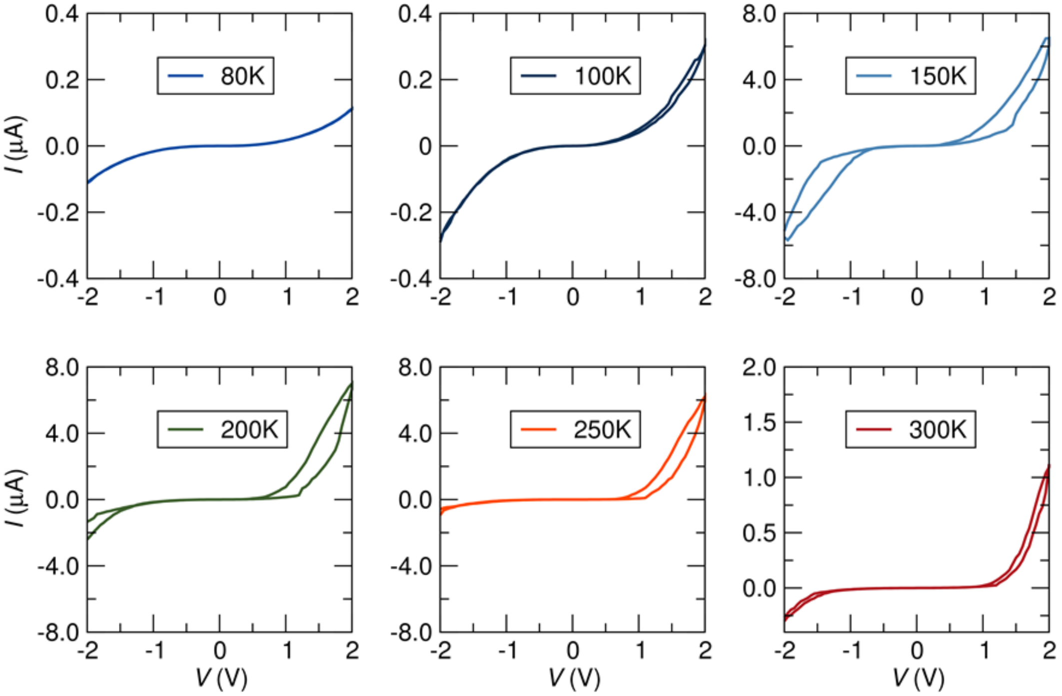

Figure 6.12: Forward and reverse current-voltage characteristics of pyrroloperylene-iodine single crystal measured at various measurement temperatures, along the length of the crystal, showing some hysteresis between the forward and reverse sweeps at higher voltages. The crystal was approximately cylindrical in shape and had a diameter and length of approximately 50 μm and 1.2 mm respectively. Measurements were carried out under vacuum at a pressure of 1×10^{-4} mbar.

We believe that the increase in differential conductivity is a materials property because poorly injecting contacts would be expected to have the opposite temperature dependence (injection would be worse at lower temperature).

Some hysteresis is observed between forward and reverse measurements at higher voltages and is hypothesized to be due to small structural instabilities in the contact interface between the silver paste and the pyrrolopyrelene-iodine crystal, or even perhaps some electromigration. This hysteresis is shown in Figure 6.12.

Overall the data is suggestive of metallic behavior above 150 K. The decrease in differential conductivity near 150 K coincides with a phase transition with no hysteresis observed using differential scanning calorimetry [Figure 6.9(c)] further suggesting that the electrical behavior is representative of the crystal. Because the structure is one-dimensional it is possible that Peierls physics is involved.[188] Differential scanning calorimetry carried out on the complex indeed suggest a reproducible solid-state phase transition at approximately 150 K, as shown in Figure 6.9(c), with no hysteresis. This led us to closely examine the structure of the complex at room temperature, reported in detail in the experimental section, which indeed suggests a slightly less distorted polyiodide chain, consistent with the 150 K incident corresponding to a structural distortion.

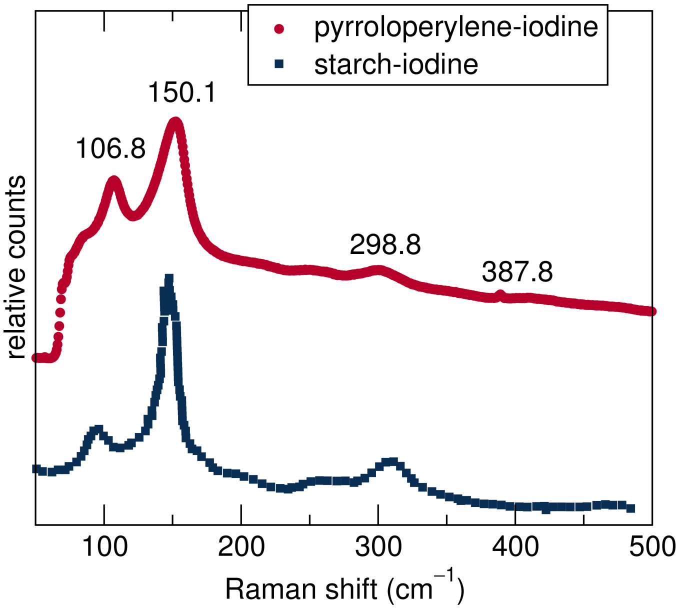

Figure 6.13: Comparative Raman spectra of the pyrroloperylene-iodine and starch iodine complexes. The latter spectrum is a digitized from Teitelbaum *et al.* [180]

Finally, Figure 6.13 displays a Raman spectrum of the pyrroloperylene-iodine complex, in the low-energy regions associated with I-I modes. The strongest vibrational modes are found to be at 106.8 cm^{-1} and 150.1 cm^{-1}. Previous reports on compounds with finite chains of I_5^-, I_7^-, and I_9^- display higher wave number signatures[148, 175, 177, 189, 193] *ie.* varying from 160 cm^{-1} to 180 cm^{-1}, which can also include signatures of I_2 at 215 cm^{-1} in the solid.[195] A summary of previously reported Raman studies on polyiodides can be found in Table 6.4. This supports the assertion of polymeric iodine speculated to be found

Table 6.4: Raman shifts of relevant polymeric iodine chain containing complexes.

Chain length	**Compound**	**shifts (cm^{-1})**	**Reference**
I_3^-	Me_4NI_3	107	[189]
	Et_4NI_3	104	[189]
	Pr_4NI_3	108	[189]
	$(Me_4As)I_3$	108	[190]
	$(n\text{-}Bu)_4NI_3$	108	[191]
	$(D_2I)I_3$	121	[192]
	TlI_3	136	[189]
	$[(EtNH_2)dt]I_3$	167	[177]
I_5^-	Me_4NI_5	153	[189]
	Et_4NI_5	183	[189]
	$(Me_4N)I_5$	113, 147, 158	[193]
I_7^-	$[PPh_4]I_7$	112, 118	[194]
	$[Et_4N]I_7$	152, 182, 134, 108	[193]
	$[(bntMe)_2I]I_7$	175, 157	[192]
I_9^-	$[K(aneO_{52})]I_9$	180, 131, 109	[177]

in starch-iodine, as reported in the spectrum from Teitelbaum et al.[180]

In conclusion, we report the isolation of a pyrroloperylene-iodine complex. The electrical conductivity of this compound is found to be close to $10^2\,\mathrm{S\,cm^{-1}}$ at room temperature, and a change in the temperature coefficient of the conductivity at temperatures close to 150 K is suggested as corresponding to a structural transition. Based on similarities between the published low-frequency Raman spectroscopic signatures of starch-iodine complex and the spectrum measured on the pyrroloperylene-iodine compound, it is suggested that the starch-iodine complex must similarly comprise infinite iodine chains.

Bibliography

[1] Energy Information Administration (US) and Government Publications Office. *International Energy Outlook 2016: With Projections to 2040*. Government Printing Office, 2016.

[2] S. Chu, Y. Cui, and N. Liu. The path towards sustainable energy. *Nat. Mater.*, 16(1):16, 2017.

[3] W. Steffen, J. Rockström, K. Richardson, T. M. Lenton, C. Folke, D. Liverman, C. P. Summerhayes, A. D. Barnosky, S. E. Cornell, and M. Crucifix. Trajectories of the earth system in the anthropocene. *Proc. Natl. Acad. Sci.*, 115(33):8252–8259, 2018.

[4] S. H. Mohr, J. Wang, G. Ellem, J. Ward, and D. Giurco. Projection of world fossil fuels by country. *Fuel*, 141:120–135, 2015.

[5] N. S. Lewis. Research opportunities to advance solar energy utilization. *Science*, 351(6271):aad1920, 2016.

[6] A. Polman, M. Knight, E. C. Garnett, B. Ehrler, and W. C. Sinke. Photovoltaic materials: Present efficiencies and future challenges. *Science*, 352(6283):aad4424, 2016.

[7] H. J. Shockley, W.and Queisser. Detailed balance limit of efficiency of p-n junction solar cells. *J. Appl. Phys.*, 32(3):510–519, 1961.

[8] A. Kojima, K. Teshima, Y. Shirai, and T. Miyasaka. Organometal halide perovskites as visible-light sensitizers for photovoltaic cells. *J. Am. Chem. Soc*, 131(17):6050–6051, 2009.

[9] W. S. Yang, B.-W. Park, E. H. Jung, N. J. Jeon, Y. C. Kim, D. U. Lee, S. S. Shin, J. Seo, E. K. Kim, and J. H. Noh. Iodide management in formamidinium-lead-halide-based perovskite layers for efficient solar cells. *Science*, 356(6345):1376–1379, 2017.

[10] I. C. Smith, E. T. Hoke, D. Solis-Ibarra, M. D. McGehee, and H. I. Karunadasa. A layered hybrid perovskite solar-cell absorber with enhanced moisture stability. *Angew. Chem. Int. Ed.*, 126:11414–11417, 2014.

[11] C. C. Stoumpos, C. M. M. Soe, H. Tsai, W. Nie, J.-C. Blancon, D. H. Cao, F. Liu, B. Traoré, C. Katan, and J. Even. High members of the 2D Ruddlesden-Popper halide perovskites: Synthesis, optical properties, and solar cells of $(CH_3(CH_2)_3NH_3)_2(CH_3NH_3)_4Pb_5I_{16}$. *Chem*, 2(3):427–440, 2017.

[12] K. Du, Q. Tu, X. Zhang, Q. Han, J. Liu, S. Zauscher, and D. B. Mitzi. Two-dimensional lead (II) halide-based hybrid perovskites templated by acene alkylamines: Crystal structures, optical properties, and piezoelectricity. *Inorg. Chem.*, 56(15):9291–9302, 2017.

[13] S. N. Ruddlesden and P. Popper. The compound $Sr_3Ti_2O_7$ and its structure. *Acta Cryst.*, 11(1):54–55, 1958.

[14] J. Even, L. Pedesseau, and C. Katan. Understanding quantum confinement of charge carriers in layered 2D hybrid perovskites. *Chem. Phys. Chem.*, 15(17):3733–3741, 2014.

[15] H. Tsai, W. Nie, J.-C. Blancon, C. C. Stoumpos, R. Asadpour, B. Harutyunyan, A. J. Neukirch, R. Verduzco, J. J. Crochet, and S. Tretiak. High-efficiency two-dimensional Ruddlesden-Popper perovskite solar cells. *Nature*, 536, 2016.

[16] D. B. Mitzi, C. A. Feild, W. T. A. Harrison, and A. M. Guloy. Conducting tin halides with a layered organic-based perovskite structure. *Nature*, 369:467–469, 1994.

[17] D. B. Mitzi, S. Wang, C. A. Feild, C. A. Chess, and A. M. Guloy. Conducting layered organic-inorganic halides containing <110>-oriented perovskite sheets. *Science*, 267:1473–1476, 1995.

[18] D. B. Mitzi, K. Chondroudis, and C. R. Kagan. Design, structure, and optical properties of organic-inorganic perovskites containing an oligothiophene chromophore. *Inorg. Chem.*, 38(4):6246–6256, 1999.

[19] N. R. Venkatesan, J. G. Labram, and M. L. Chabinyc. Charge-carrier dynamics and crystalline texture of layered Ruddlesden-Popper hybrid lead iodide perovskite thin films. *ACS Energy Lett.*, 3(2):380–386, 2018.

[20] D. B. Mitzi, K. Chondroudis, and C. R. Kagan. Organic-inorganic electronics. *IBM J. Res. and Dev.*, 45(1):29–45, 2001.

[21] M. D. Smith, A. Jaffe, E. R. Dohner, A. M. Lindenberg, and H. I. Karunadasa. Structural origins of broadband emission from layered Pb-Br hybrid perovskites. *Chem. Sci.*, 8(6):4497–4504, 2017.

[22] E. R. Dohner, E. T. Hoke, and H. I. Karunadasa. Self-assembly of broadband white-light emitters. *J. Am. Chem. Soc.*, 136(5):1718–1721, 2014.

[23] L. Mao, C. C. Stoumpos, and M. G. Kanatzidis. Two-dimensional hybrid halide perovskites: Principles and promises. *J. Am. Chem. Soc.*, 3:jacs.8b10851, 2018.

[24] B. Lee, C. C. Stoumpos, N. Zhou, F. Hao, C. Malliakas, C.-Y. Yeh, T. J. Marks, M. G. Kanatzidis, and R. P. H. Chang. Air-stable molecular semiconducting iodosalts for solar cell applications: Cs_2SnI_6 as a hole conductor. *J. Am. Chem. Soc.*, 136(43):15379–15385, 2014.

[25] B. Saparov, J.-P. Sun, W. Meng, Z. Xiao, H.-S. Duan, O. Gunawan, D. Shin, I. G. Hill, Y. Yan, and D. B. Mitzi. Thin-film deposition and characterization of a Sn-deficient perovskite derivative Cs_2SnI_6. *Chem. Mater.*, 28(7):2315–2322, 2016.

[26] A. E. Maughan, A. M. Ganose, M. M. Bordelon, E. M. Miller, D. O. Scanlon, and J. R. Neilson. Defect tolerance to intolerance in the vacancy-ordered

double perovskite semiconductors Cs_2SnI_6 and Cs_2TeI_6. *J. Am. Chem. Soc*, 138(27):8453–8464, 2016.

[27] T. A. Shestimerova, N. A. Golubev, N. A. Yelavik, M. A. Bykov, A. V. Grigorieva, Z. Wei, E. V. Dikarev, and A. V. Shevelkov. Role of I_2 molecules and weak interactions in supramolecular assembling of pseudo-three-dimensional hybrid bismuth polyiodides: Synthesis, structure, and optical properties of phenylenediammonium polyiodobismuthate(III). *Cryst. Growth Des.*, 18(4):2572–2578, 2018.

[28] T. A. Shestimerova, N. A. Yelavik, A. V. Mironov, A. N. Kuznetsov, M. A. Bykov, A. V. Grigorieva, V. V. Utochnikova, L. S. Lepnev, and A. V. Shevelkov. From isolated anions to polymer structures through linking with I_2: Synthesis, structure, and properties of two complex bismuth(III) iodine iodides. *Inorg. Chem.*, 57(7):4077–4087, 2018.

[29] F. Wudl, G. M. Smith, and E. J. Hufnagel. Unusually stable organic radical. *J. Chem. Soc. D*, 1453–1454, 1970.

[30] F. Wudl, D. Wobschall, and E. Hufnagel. Electrical conductivity by the bis(1,3-dithiole)-bis(1,3-dithiolium) system. *J. Am. Chem. Soc.*, 94(3):670–672, 1972.

[31] M. R. Bryce. Functionalised tetrathiafulvalenes: New applications as versatile π-electron systems in materials chemistry. *J. Mater. Chem.*, 10(3):589–598, 2000.

[32] N. Martín. Tetrathiafulvalene: The advent of organic metals. *Chem. Commun.*, 49(63):7025–7027, 2013.

[33] G. W. Crabtree, K. D. Carlson, L. N. Hall, P. T. Copps, H. H. Wang, T. J. Emge, M. A. Beno, and J. M. Williams. Superconductivity at ambient pressure in di[bis(ethylenedithio)tetrathiafulvalene]triiodide, $(BEDTTTF)_2I_3$. *Phys. Rev. B*, 30(5):2958–2960, 1984.

[34] T. Devic, M. Evain, Y. Moëlo, E. Canadell, P. Auban-Senzier, M. Fourmigué, and P. Batail. Single crystalline commensurate metallic assemblages of π-slabs and CdI_2-type layers: Synthesis and properties of β-

$(\mathrm{EDT\text{-}TTF\text{-}I_2})_2[\mathrm{Pb}_{5/6}\square_{1/6}\mathrm{I}_2]_3$ and β-$(\mathrm{EDT\text{-}TTF\text{-}I_2})_2[\mathrm{Pb}_{2/3+x}\mathrm{Ag}_{1/3-2x}\square_x\mathrm{I}_2]_3$, x = 0.05. *J. Am. Chem. Soc.*, 125(11):3295–3301, 2003.

[35] T. Devic, E. Canadell, P. Auban-Senzier, and P. Batail. $(\mathrm{EDT\text{-}TTF\text{-}I_2})_2\mathrm{PbI_3{\cdot}H_2O}$: an ambient pressure metal with a β' donor slab topology. *J. Mater. Chem.*, 14(2):135–137, 2004.

[36] K. Kondo, G. Matsubayashi, T. Tanaka, H. Yoshioka, and K. Nakatsu. Preparation and properties of tetrathiafulvalene (ttf) and tetramethyltetraselenafulvalene salts of tin(IV) halide anions and X-ray crystal structure of $[\mathrm{ttf}]_3[\mathrm{SnCl_6}]$. *Dalton Trans.*, (3):379, 1984.

[37] R. Kumai, A. Asamitsu, and Y. Tokura. Magnetic and transport properties of organic radical ion salts containing tetrahalogenoferrate anion. *Synth. Met.*, 85(1):1681–1682, 1997.

[38] T. C. Narayan, T. Miyakai, S. Seki, and M. Dincă. High charge mobility in a tetrathiafulvalene-based microporous metalorganic framework. *J. Am. Chem. Soc.*, 134(31):12932–12935, 2012.

[39] A. A. Talin, A. Centrone, A. C. Ford, M. E. Foster, V. Stavila, P. Haney, R. A. Kinney, V. Szalai, F. El Gabaly, and H. P. Yoon. Tunable electrical conductivity in metal-organic framework thin-film devices. *Science*, 343(6166):66–69, 2014.

[40] S. Tominaka, H. Hamoudi, T. Suga, T. D. Bennett, A. B. Cairns, and A. K. Cheetham. Topochemical conversion of a dense metalorganic framework from a crystalline insulator to an amorphous semiconductor. *Chem. Sci.*, 6(2):1465–1473, 2015.

[41] P. J. Beldon, S. Tominaka, P. Singh, T. S. Dasgupta, E. G. Bithell, and A. K. Cheetham. Layered structures and nanosheets of pyrimidinethiolate coordination polymers. *Chem. Commun.*, 50(30):3955–3957, 2014.

[42] V. Stavila, A. A. Talin, and M. D. Allendorf. MOF-based electronic and opto-electronic devices. *Chem. Soc. Rev.*, 43(16):5994–6010, 2014.

[43] D. H. Cao, C. C. Stoumpos, O. K. Farha, J. T. Hupp, and M. G. Kanatzidis. Two-dimensional homologous perovskites as light absorbing materials for solar cell applications. *J. Am. Chem. Soc.*, 2:7843 – 7850, 2015.

[44] A. E. Maughan, J. A. Kurzman, and J. R. Neilson. Hybrid inorganicorganic materials with an optoelectronically active aromatic cation: $(C_7H_7)_2SnI_6$ and $C_7H_7PbI_3$. *Inorg. Chem.*, 54(1):370–378, 2014.

[45] F. Wudl, M. L. Kaplan, E. M. Engler, and V. V. Patel. 2,2-bi-L,3-dithiolylidene (tetrathiafulvalene, ttf) and its radical cation salts. In *Inorganic Syntheses*, pages 27–34. John Wiley & Sons, Inc., 1979.

[46] G. M. Sheldrick. SADABS, program for scaling and correction of area detector data. *University of Göttingen, Germany*, 33, 1997.

[47] G. M. Sheldrick. SHELXTL v. 6.12, structure determination software suite, 2000.

[48] K. Momma and F. Izumi. An integrated three-dimensional visualization system VESTA using wxWidgets. *Commision Crystallogr. Comput., IUCr Newslett*, (7):106–119, 2006.

[49] A. C. Larson and R. B. Von Dreele. General structure analysis system (GSAS); Report LAUR 86-748; Los Alamos National Laboratory: Los Alamos, NM, 2000. pages 86–748, 2000.

[50] B. H. Toby. EXPGUI, a graphical user interface for GSAS. *J. Appl. Crystallogr.*, 34(2):210–213, 2001.

[51] S. Stoll and A. Schweiger. EasySpin, a comprehensive software package for spectral simulation and analysis in EPR. *J. Magn. Reson.*, 178(1):42–55, 2006.

[52] G. Kresse and J. Hafner. Ab initio molecular dynamics for liquid metals. *Phys. Rev. B*, 47(1):558, 1993.

[53] G. Kresse and J. Hafner. Ab initio molecular-dynamics simulation of the liquid-metalamorphous-semiconductor transition in germanium. *Phys. Rev. B*, 49(20):14251, 1994.

[54] G. Kresse and J. Furthmüller. Efficiency of ab-initio total energy calculations for metals and semiconductors using a plane-wave basis set. *Comput. Mater. Sci.*, 6(1):15–50, 1996.

[55] G. Kresse and J. Furthmüller. Efficient iterative schemes for ab initio total-energy calculations using a plane-wave basis set. *Phys. Rev. B*, 54(16):11169, 1996.

[56] P. E. Blöchl. Projector augmented-wave method. *Phys. Rev. B*, 50(24):17953, 1994.

[57] G. Kresse and D. Joubert. From ultrasoft pseudopotentials to the projector augmented-wave method. *Physical Review B*, 59(3):1758, 1999.

[58] G M Sheldrick. Program for the refinement of crystal structures. *SHELXL97*, 1997.

[59] G. M. Sheldrick. A short history of SHELX. *Acta Cryst. A*, 64(1):112–122, 2008.

[60] J. P. Perdew, K. Burke, and M. Ernzerhof. Generalized gradient approximation made simple. *Phys. Rev. Lett.*, 77(18):3865, 1996.

[61] M. I. Aroyo, D. Orobengoa, G. de la Flor, E. S. Tasci, J. M. Perez-Mato, and H. Wondratschek. Brillouin-zone database on the Bilbao Crystallographic Server. *Acta Cryst. A*, 70(2):126–137, 2014.

[62] J. Heyd, G. E. Scuseria, and M. Ernzerhof. Hybrid functionals based on a screened coulomb potential. *J. Chem. Phys.*, 118(18):8207–8215, 2003.

[63] J. Heyd and G. E. Scuseria. Efficient hybrid density functional calculations in solids: Assessment of the Heyd-Scuseria-Ernzerhof screened coulomb hybrid functional. *J. Chem. Phys*, 121(3):1187–1192, 2004.

[64] J. Brgoch, A. J. Lehner, M. Chabinyc, and R. Seshadri. Ab initio calculations of band gaps and absolute band positions of polymorphs of $RbPbI_3$ and $CsPbI_3$: Implications for main-group halide perovskite photovoltaics. *J. Phys. Chem. C*, 118(48):27721–27727, 2014.

[65] A. J. Lehner, D. H. Fabini, H. A. Evans, C.-A. Hèbert, S. R. Smock, J. Hu, H. Wang, J. W Zwanziger, M. L. Chabinyc, and R. Seshadri. Crystal and electronic structures of complex bismuth iodides $A_3Bi_2I_9$ (A= K, Rb, Cs) Related to perovskite: Aiding the rational design of photovoltaics. *Chem. Mater.*, 27(20):7137–7148, 2015.

[66] R. C. Teitelbaum, S. L. Ruby, and T. J. Marks. A resonance raman/iodine Mössbauer investigation of the starch-iodine structure. Aqueous solution and iodine vapor preparations. *J. Am. Chem. Soc.*, 102(10):3322–3328, 1980.

[67] T. Sugano, K. Yakushi, and H. Kuroda. Polarized absorption spectra of single crystals of tetrathiafulvalenium salts. *Bull. Chem. Soc. Jpn.*, 51(4):1041–1046, 1978.

[68] J. B. Torrance, B. A. Scott, and F. B. Kaufman. Optical properties of charge transfer salts of tetracyanoquinodimethane (TCNQ). *Solid State Commun.*, 17(11):1369–1373, 1975.

[69] J. B. Torrance, B. A. Scott, B. Welber, F. B. Kaufman, and P. E. Seiden. Optical properties of the radical cation tetrathiafulvalenium (TTF+) in its mixed-valence and monovalence halide salts. *Phys. Rev. B*, 19(2):730, 1979.

[70] J.-P. Legros, M. Bousseau, L. Valade, and P. Cassoux. Crystal structure of a non-conductive non-stoichiometric tetrathiafulvalenium salt: $(TTF)_4(BF_4)_2$. *Mol. Cryst. Liq. Cryst.*, 100(1-2):181–192, 1983.

[71] G Wagoner. Spin resonance of charge carriers in graphite. *Phys. Rev.*, 118(3):647, 1960.

[72] B. A. Scott, S. J. La Placa, J. B. Torrance, B. D. Silverman, and B. Welber. The crystal chemistry of organic metals. Composition, structure, and stability in the tetrathiafulvalinium-halide systems. *J. Am. Chem. Soc.*, 99(20):6631–6639, 1977.

[73] T. Mori, K. Kato, Y. Maruyama, H. Inokuchi, H. Mori, I. Hirabayashi, and S. Tanaka. Structural and physical properties of a new organic super-

conductor, $(BEDT\text{-}TTF)_4Pd(CN)_4{\bullet}H_2O$. *Solid State Commun.*, 82(3):177–181, 1992.

[74] U. Geiser, H. H. Wang, S. M. Budz, M. J. Lowry, J. M. Williams, J. Ren, and M. Whangbo. Polymeric anions leading to novel packing motifs in donor-radical salts: Synthesis and crystal and band electronic structure of $(BEDT\text{-}TTF)BiI_4$. (4):1611–1614, 1990.

[75] C. Bellitto, V. Fares, F. Federici, P. Serino, P. Day, and M. Kurmoo. Low-dimensional magnetic behaviour of new radical-ion salts: $(BEDT\text{-}TTF)_2[Au^{III}(i\text{-}mnt)_2]$ and $(BEDT\text{-}TTF)_2[BiBr_4]$. *Synth Met*, 79(1):33–36, 1996.

[76] M. Fujiwara, N. Tajima, T. Imakubo, M. Tamura, and R. Kato. Structural and physical properties of new conducting cation radical salts with Te-based counteranions, tetraiodotellurate(II) and hexaiododitellurate(II). *J. Solid State Chem.*, 168(2):396–407, 2002.

[77] S. S. Park, E. R Hontz, L. Sun, C. H. Hendon, A. Walsh, T. Van Voorhis, and M. Dincă. Cation-dependent intrinsic electrical conductivity in isostructural tetrathiafulvalene-based microporous metalorganic frameworks. *J. Am. Chem. Soc.*, 137(5):1774–1777, 2015.

[78] L. Sun, M. G. Campbell, and M. Dincă. Electrically conductive porous metalorganic frameworks. *Angew. Chem. Int. Ed.*, 55(11):3566–3579, 2016.

[79] M. D. Allendorf, A. Schwartzberg, V. Stavila, and A A. Talin. A roadmap to implementing metalorganic frameworks in electronic devices: Challenges and critical directions. *Chem. Eur. J.*, 17(41):11372–11388, 2011.

[80] X. Huang, P. Sheng, Z. Tu, F. Zhang, J. Wang, H. Geng, Y. Zou, C. Di, Y. Yi, and Y. Sun. A two-dimensional $[\pi]$-d conjugated coordination polymer with extremely high electrical conductivity and ambipolar transport behaviour. *Nat. Commun.*, 6, 2015.

[81] J. Tanaka, M. Tanaka, T. Kawai, T. Takabe, and O. Maki. Electronic spectra and electronic structure of TCNQ complexes. *Bull. Chem. Soc. Jpn.*, 49(9):2358–2373, 1976.

[82] M. A. Butler, F. Wudl, and Z. G. Soos. NMR study of partial charge transfer in N-methylphenazinium-tetracyanoquinodimethane (NMP-TCNQ). *Phys. Rev. B*, 12(11):4708, 1975.

[83] H. A. Evans, A. J. Lehner, J. G. Labram, D. H. Fabini, O. Barreda, S. R. Smock, G. Wu, M. L. Chabinyc, R. Seshadri, and F. Wudl. (TTF)Pb_2I_5: a radical cation-stabilized hybrid lead iodide with synergistic optoelectronic signatures. *Chem. Mater.*, 28(11):3607–3611, 2016.

[84] H. Cui, T. Otsuka, A. Kobayashi, Y. Misaki, and H. Kobayashi. Structural and electrical properties of novel molecular conductors based on extended-TTF donors BDT-TTP and I^- anions. *Bull. Chem. Soc. Jpn.*, 76(1):97–102, 2003.

[85] T. Mori, H. Inokuchi, Y. Misaki, T. Yamabe, H. Mori, and S. Tanaka. Crystal structures of highly conducting iodine complexes of TTM-TTP. *Bull. Chem. Soc. Jpn.*, 67(3):661–667, 1994.

[86] N. Mott. *Metal-insulator transitions*. CRC Press, 1990.

[87] A. J. Epstein, W.-P. Lee, and V. N. Prigodin. Low-dimensional variable range hopping in conducting polymers. *Synth. Met.*, 117(1-3):9–13, 2001.

[88] R. B. Somoano, A. Gupta, V. Hadek, M. Novotny, M. Jones, T. Datta, R. Deck, and A. M. Hermann. Electrical, magnetic, and optical properties of the tetrathiafulvalene (TTF) pseudohalides,$(TTF)_{12}(SCN)_7$ and $(TTF)_{12}(SeCN)_7$. *Phys. Rev. B*, 15(2):595–601, 1977.

[89] M. M. Lee, J. Teuscher, T. Miyasaka, T. N. Murakami, and H. J. Snaith. Efficient hybrid solar cells based on meso-superstructured organometal halide perovskites. *Science*, page 1228604, 2012.

[90] M. Saliba, T. Matsui, J.-Y. Seo, K. Domanski, J.-P. Correa-Baena, M. K. Nazeeruddin, S. M. Zakeeruddin, W. Tress, A. Abate, and A. Hagfeldt. Cesium-containing triple cation perovskite solar cells: Improved stability, reproducibility and high efficiency. *Energy Environ. Sci.*, 9(6):1989–1997, 2016.

[91] D. H. Fabini, J. G. Labram, A. J. Lehner, J. S. Bechtel, H. A. Evans, A. Van der Ven, F. Wudl, M. L. Chabinyc, and R. Seshadri. Main-group halide semiconductors derived from perovskite: Distinguishing chemical, structural, and electronic aspects. *Inorg. Chem.*, 56(1):11–25, 2016.

[92] W. Li, Z. Wang, F. Deschler, S. Gao, R. H. Friend, and A. K. Cheetham. Chemically diverse and multifunctional hybrid organic-inorganic perovskites. *Nat. Rev. Mater.*, 2(3):16099, feb 2017.

[93] B. Saparov and D. B. Mitzi. Organicinorganic perovskites: Structural versatility for functional materials design. *Chem. Rev.*, 116(7):4558–4596, apr 2016.

[94] C. M. M. Soe, C. C. Stoumpos, M. Kepenekian, B. Traoré, H. Tsai, W. Nie, B. Wang, C. Katan, R. Seshadri, and A. D. Mohite. New type of 2D perovskites with alternating cations in the interlayer space, $(C(NH_2)_3)(CH_3NH_3)_nPb_nI_{3n+1}$: Structure, properties, and photovoltaic performance. *J. Am. Chem. Soc.*, 139(45):16297–16309, 2017.

[95] D. J. Kubicki, D. Prochowicz, A. Hofstetter, M. Saski, P. Yadav, D. Bi, N. Pellet, J. Lewiński, S. M. Zakeeruddin, and M. Grätzel. Formation of stable mixed guanidiniummethylammonium phases with exceptionally long carrier lifetimes for high-efficiency lead iodide-based perovskite photovoltaics. *J. Am. Chem. Soc.*, 140(9):3345–3351, 2018.

[96] F. Wei, Z. Deng, S. Sun, F. Zhang, D. M. Evans, G. Kieslich, S. Tominaka, M. A. Carpenter, J. Zhang, and P. D. Bristowe. Synthesis and properties of a lead-free hybrid double perovskite:$(CH_3NH_3)_2AgBiBr_6$. *Chem. Mater.*, 29(3):1089–1094, 2017.

[97] E. T. McClure, M. R. Ball, W. Windl, and P. M. Woodward. Cs_2AgBiX_6 (X = Br, Cl): new visible light absorbing, lead-free halide perovskite semiconductors. *Chem. Mater.*, 28(5):1348–1354, 2016.

[98] A. H. Slavney, T. Hu, A. M. Lindenberg, and H. I. Karunadasa. A bismuth-halide double perovskite with long carrier recombination lifetime for photovoltaic applications. *J. Am. Chem. Soc.*, 138(7):2138–2141, 2016.

[99] S. G. Duyker, J. A. Hill, C. J. Howard, and A. L. Goodwin. Guest-activated forbidden tilts in a molecular perovskite analogue. *J. Am. Chem. Soc.*, 138(35):11121–11123, 2016.

[100] X.-G. Zhao, D. Yang, Y. Sun, T. Li, L. Zhang, L. Yu, and A. Zunger. CuIn halide perovskite solar absorbers. *J. Am. Chem. Soc.*, 139(19):6718–6725, 2017.

[101] R. G. Dickinson. The crystal structures of potassium and ammonium chlorostannates. *J. Am. Chem. Soc.*, 44(2):276–288, 1922.

[102] Robin L Armstrong. Structural properties and lattice dynamics of 5d transition metal antifluorite crystals. *Phys. Rep.*, 57(6):343–396, 1980.

[103] M. Krupski. Rigid sphere model applied to the phase transitions of complex compounds of the type K_2PtCl_6. *Phys. Status Solidi A*, 78(2):751–758, 1983.

[104] K. Prassides, P. Day, and A. K. Cheetham. Anion ordering in mixed valence dicesium hexachloroantimonate (Cs_2SbCl_6) and related salts. *J. Am. Chem. Soc.*, 105(10):3366–3368, 1983.

[105] Y. Kume, R. Ikeda, and D. Nakamura. Structural phase transition in various methylammonium hexahalometallates(IV) as studied by the NQR of halogens. *J. Magn. Reson.*, 33(2):331–344, 1979.

[106] R. Ikeda, Y. Kume, D. Nakamura, Y. Furukawa, and H. Kiriyama. Motion of methylammonium ions in methylammonium hexachloroplatinate (IV) and hexachlorostannate (IV) as studied by proton magnetic resonance. *J. Magn. Reson.*, 24(1):9–20, 1976.

[107] T. Matsuo, M. Ueda, and H. Suga. Calorimetric and spectroscopic studies of the critical phase transition in $(CH_3NH_3)_2[SnCl_6]$. *Chem. Phys. Lett.*, 82(3):577–580, 1981.

[108] T. Matsuo, H.-K. Yan, and H. Suga. Calorimetric study of the phase transition in deuterated methylammonium hexachlorostannate. *J. Phys. Chem. Solids*, 49(1):85–90, 1988.

[109] D. Nakamura. Nuclear quadrupole resonance studies of structural and magnetic phase transitions. *J. Mol. Struct.*, 111:341–356, 1983.

[110] K. Horiuchi, H. Ishida, and D. Nakamura. A temperature dependence study of ^{35}Cl NQR frequencies in dimethylammonium hexachlorostannate (IV), hexachlorotellurate (IV), and hexachloroplatinate (IV). *Bull. Chem. Soc. Jpn.*, 58(9):2590–2594, 1985.

[111] K. B. Dillon, J. Halfpenny, and A. Marshall. A variable-temperature ^{79}Br nuclear quadrupole resonance and X-ray crystallographic investigation of dimethylammonium hexabromostannate(IV),$[NH_2Me_2]_2[SnBr_6]$. *Dalton Trans.*, (6):1091–1094, 1983.

[112] B. V. S. Murthy, K. P. Ramesh, and J. Ramakrishna. NMR study of molecular dynamics and phase transitions in dimethyl ammonium hexabromo selenate $[NH_2(CH_3)_2]_2SeBr_6$. *J. Phys. Chem. Solids*, 61(6):961–968, 2000.

[113] A. E. Maughan, A. M. Ganose, A. M. Candia, J. T. Granger, D. O. Scanlon, and J. R. Neilson. Anharmonicity and octahedral tilting in hybrid vacancy-ordered double perovskites. *Chem. Mater.*, 30(2):472–483, 2017.

[114] R. L. Datta. L.The double platinic and cupric iodides of substituted ammonium bases. *J. Chem. Soc.*, 103:426–432, 1913.

[115] M. Sutton, R. L. Armstrong, B. M. Powell, and W. J. L. Buyers. Neutron diffraction study of the structural changes in the antifluorite crystals Rb_2PtI_6,$(NH_4)_2PtBr_6$, and $(NH_4)_2PtI_6$. *Can. J. Phys.*, 59(3):449–456, 1981.

[116] G. Thiele, C. Mrozek, D. Kammerer, and K. Wittmann. On hexaiodoplatinates (IV) M_2PtI_6 (M = K, Rb, Cs, NH_4, Tl) - preparation, properties, and structural data. *Z. Naturforsch. B Chem. Sci.*, 38(8):905–910, 1983.

[117] A. Coelho. TOPAS and TOPAS-Academic: an optimization program integrating computer algebra and crystallographic objects written in C++. *J. Appl. Crystallogr.*, 51(1):210–218, feb 2018.

[118] H. J. Monkhorst and J. D. Pack. Special points for Brillouin-zone integrations. *Phys. Rev. B*, 13(12):5188, 1976.

[119] S. Grimme, J. Antony, S. Ehrlich, and H. Krieg. A consistent and accurate ab initio parametrization of density functional dispersion correction (DFT-D) for the 94 elements H-Pu. *J. Chem. Phys.*, 132(15):154104, 2010.

[120] H. T. Stokes and D. M. Hatch. FINDSYM: program for identifying the spacegroup symmetry of a crystal. *J. Appl. Crystallogr.*, 38(1):237–238, 2005.

[121] W. Setyawan and S. Curtarolo. High-throughput electronic band structure calculations: Challenges and tools. *Comput. Mater. Sci.*, 49(2):299–312, 2010.

[122] M. Gajdoš, K. Hummer, G. Kresse, J. Furthmüller, and F. Bechstedt. Linear optical properties in the projector-augmented wave methodology. *Phys. Rev. B*, 73(4):45112, 2006.

[123] P. J. Ewing and L. Pauling. II. The crystal structure of potassium chloroplatinate. *Z. Kristallogr. Cryst. Mater.*, 68(1-6):223–230, 1928.

[124] R. J. Williams, D. R. Dillin, and W. O. Milligan. Structure refinement of potassium chloroplatinate by powder and single-crystal methods. *Acta Cryst. B*, 29(7):1369–1372, 1973.

[125] A. M. Glazer. The classification of tilted octahedra in perovskites. *Acta Cryst. B*, 28(11):3384–3392, 1972.

[126] H. A. Evans, E. C. Schueller, S. R. Smock, G. Wu, R. Seshadri, and F. Wudl. Perovskite-related hybrid noble metal iodides: Formamidinium platinum iodide [$(FA)_2Pt^{IV}I_6$] and mixed-valence methylammonium gold iodide [$(MA)_2Au^{I}Au^{III}I_6$]. *Inorganica Chim. Acta*, 468:280–284, nov 2017.

[127] H. Ishida and S. Kashino. Bis(dimethylammonium) hexachlorotellurate(IV). *Acta Cryst. C*, 54(12):1811–1813, 1998.

[128] M. H. Ben Ghozlen, A. Daoud, and J. W. Bats. Dimethylammonium hexachlorostannate(IV). *Acta. Cryst. B*, 37(7):1415–1416, 1981.

[129] H. Ishida, Y. Furukawa, and S. Kashino. Bis(guanidinium) hexachlorostannate(IV). *Acta Cryst.*, 55(12):1995–1997, 1999.

[130] P. Bukovec and R. Hoppe. Zur kenntnis von hexagonalem $K_2[MnF_6]$. *J. Fluorine Chem.*, 23(6):579–587, 1983.

[131] G. Kieslich, S. Sun, and A. K. Cheetham. Solid-state principles applied to organicinorganic perovskites: new tricks for an old dog. *Chemical Science*, 5(12):4712–4715, 2014.

[132] R. D. T. Shannon and C. T. Prewitt. Effective ionic radii in oxides and fluorides. *Acta Cryst. B*, 25(5):925–946, 1969.

[133] R. D. Shannon. Revised effective ionic radii and systematic studies of interatomic distances in halides and chalcogenides. *Acta Cryst A*, 32(5):751–767, 1976.

[134] A. E. Maughan, A. M. Ganose, M. A. Almaker, D. O. Scanlon, and J. R. Neilson. Tolerance factor and cooperative tilting effects in vacancy-ordered double perovskite halides. *Chem. Mater.*, 2018.

[135] O. Muller and R. Roy. *The major ternary structural families*. Springer, 1974.

[136] N. Bloembergen, E. M. Purcell, and R. V. Pound. Relaxation effects in nuclear magnetic resonance absorption. *Phys. Rev.*, 73(7):679–712, apr 1948.

[137] R. E. Wasylishen, O. Knop, and J. B. Macdonald. Cation rotation in methylammonium lead halides. *Solid State Commun.*, 56(7):581–582, 1985.

[138] S. Senthil Kumaran, K. P. Ramesh, and J. Ramakrishna. Proton NMR T_1 studies in methylammonium trichlorO stannate(II)($CH_3NH_3SnCl_3$). *Phase Transit.*, 75(6):597–605, 2002.

[139] T. Besara, P. Jain, N. S. Dalal, P. L. Kuhns, A. P. Reyes, H. W. Kroto, and A. K. Cheetham. Mechanism of the orderdisorder phase transition, and glassy behavior in the metal-organic framework $[(CH_3)_2NH_2]Zn(HCOO)_3$. *Proc. Natl. Acad. Sci.*, 2011.

[140] N. Abhyankar, J. J. Kweon, M. Orio, S. Bertaina, M. Lee, E. S. Choi, R. Fu, and N. S. Dalal. Understanding ferroelectricity in the Pb-free perovskite-like metalorganic framework $[(CH_3)_2NH_2]Zn\ (HCOO)_3$: Dielectric, 2D NMR, and theoretical studies. *J. Phys. Chem. C*, 121(11):6314–6322, 2017.

[141] D. H Fabini, T. A. Siaw, C. C Stoumpos, G. Laurita, D. Olds, K. Page, J. G. Hu, M. G. Kanatzidis, S. Han, and R. Seshadri. Universal dynamics of molecular reorientation in hybrid lead iodide perovskites. *J. Am. Chem. Soc.*, 139(46):16875–16884, 2017.

[142] W. Li, A. Thirumurugan, P. T. Barton, Z. Lin, S. Henke, H. H.-M. Yeung, M. T. Wharmby, E. G. Bithell, C. J. Howard, and A. K. Cheetham. Mechanical tunability via hydrogen bonding in metalorganic frameworks with the perovskite architecture. *J. Am. Chem. Soc.*, 136(22):7801–7804, 2014.

[143] K. L. Svane, A. C. Forse, C. P. Grey, G. Kieslich, A. K. Cheetham, A. Walsh, and K. T. Butler. How strong is the hydrogen bond in hybrid perovskites? *J. Phys. Chem. Lett.*, 8(24):6154–6159, 2017.

[144] Q. Pan, Z.-B. Liu, Y.-Y. Tang, P.-F. Li, R.-W. Ma, R.-Y. Wei, Y. Zhang, Y.-M. You, H.-Y. Ye, and R.-G. Xiong. A three-dimensional molecular perovskite ferroelectric:(3-ammoniopyrrolidinium)$RbBr_3$. *J. Am. Chem. Soc.*, 139(11):3954–3957, 2017.

[145] T. Steiner. Hydrogen-bond distances to halide ions in organic and organometallic crystal structures: Up-to-date database study. *Acta Cryst. B*, 54(4):456–463, 1998.

[146] L. Yu, R. S. Kokenyesi, D. A. Keszler, and A. Zunger. Inverse design of high absorption thin-film photovoltaic materials. *Adv. Energy Mater.*, 3(1):43–48, 2013.

[147] D. M. P. Mingos. *Essential trends in inorganic chemistry*. Oxford University Press Oxford, 1998.

[148] P. H. Svensson and L. Kloo. Synthesis, structure, and bonding in polyiodide and metal iodide-iodine systems. *Chem. Rev.*, 103(5):1649–1684, 2003.

[149] S. A. Adonin, M. N. Sokolov, and V. P. Fedin. Polyhalide-bonded metal complexes: Structural diversity in an eclectic class of compounds. *Coord. Chem. Rev.*, 367:1–17, 2018.

[150] S. Madhu, H. A. Evans, V. V. T. Doan-Nguyen, J. G. Labram, G. Wu, M. L. Chabinyc, R. Seshadri, and F. Wudl. Infinite polyiodide chains in the pyrroloperylene-iodine complex: insights into the starch-iodine and perylene-iodine complexes. *Angew. Chem. Int. Ed.*, 55(28):8032–8035, 2016.

[151] A. J. Heeger, S. Kivelson, J. R. Schrieffer, and W.-P. Su. Solitons in conducting polymers. *Rev. Mod. Phys.*, 60(3):781, 1988.

[152] A. Hagfeldt and M. Grätzel. Molecular photovoltaics. *Acc. Chem. Res.*, 33(5):269–277, 2000.

[153] B. Li, L. Wang, B. Kang, P. Wang, and Y. Qiu. Review of recent progress in solid-state dye-sensitized solar cells. *Sol. Energy Mater Sol. Cells*, 90(5):549–573, 2006.

[154] Elizabeth A Gibson. Dye-sensitized photocathodes for H_2 evolution. *Chem. Soc. Rev.*, 46(20):6194–6209, 2017.

[155] G. Zhang, M. Zhang, X. Ye, X. Qiu, S. Lin, and X. Wang. Iodine modified carbon nitride semiconductors as visible light photocatalysts for hydrogen evolution. *Adv. Mater.*, 26(5):805–809, 2014.

[156] Y. Zhao and K. Zhu. Organic-inorganic hybrid lead halide perovskites for optoelectronic and electronic applications. *Chem. Soc. Rev.*, 45(3):655–689, 2016.

[157] B. Saparov and D. B. Mitzi. Organicinorganic perovskites: Structural versatility for functional materials design. *Chem. Rev.*, 116(7):4558–4596, 2016.

[158] W. Zhang, X. Liu, L. Li, Z. Sun, S. Han, Z. Wu, and J. Luo. Triiodide-induced band-edge reconstruction of a lead-free perovskite-derivative hybrid for strong light absorption. *Chem. Mater.*, 30:4081–4088, 2018.

[159] H. A. Evans, D. H. Fabini, J. L. Andrews, M. Koerner, M. B. Preefer, G. Wu, F. Wudl, A. K. Cheetham, and R. Seshadri. Hydrogen bonding controls the structural evolution in perovskite-related hybrid platinum (IV) iodides. *Inorg. Chem.*, 57:10375–10382, 2018.

[160] A. N. Usoltsev, S. A. Adonin, P. A. Abramov, A. S. Novikov, V. R. Shayapov, P. E. Plyusnin, I. V. Korolkov, M. N. Sokolov, and V. P. Fedin. 1D and 2D polybromotellurates(IV): Structural studies and thermal stability. *Eur. J. Inorg. Chem.*, 2018(27):3264–3269, 2018.

[161] M. Berkei, J. F. Bickley, B. T. Heaton, and A. Steiner. Polymeric anionic networks using dibromine as a crosslinker; the preparation and crystal structure of $[(C_4H_9)_4N]_2[Pt_2Br_{10}]\cdot(Br_2)_7$ and $[(C_4H_9)_4N]_2[PtBr_4Cl_2]\cdot(Br_2)_6$. *Chem Commun.*, (18):2180–2181, 2002.

[162] D. Schneider, A. Schier, and H. Schmidbaur. Governing the oxidative addition of iodine to gold(I) complexes by ligand tuning. *Dalton Transactions*, (13):1995–2005, 2004.

[163] K. F. Purcell and J. C. Kotz. *An introduction to inorganic chemistry*. Holt Rinehart & Winston, 1980.

[164] A. Poglitsch and D. Weber. Dynamic disorder in methylammoniumtrihalogenoplumbates (II) observed by millimeter-wave spectroscopy. *J. Chem. Phys.*, 87(11):6373–6378, 1987.

[165] M. T. Weller, O. J. Weber, J. M. Frost, and A. Walsh. Cubic perovskite structure of black formamidinium lead iodide, α-$[HC(NH_2)_2]PbI_3$, at 298 K. *J. Phys. Chem. Lett.*, 6(16):3209–3212, 2015.

[166] D. H. Fabini, C. C. Stoumpos, G. Laurita, A. Kaltzoglou, A. G. Kontos, P. Falaras, M. G. Kanatzidis, and R. Seshadri. Reentrant structural and optical properties and large positive thermal expansion in perovskite formamidinium lead iodide. *Angew. Chem. Int. Ed.*, 55(49):15392–15396, 2016.

[167] G. Cavallo, P. Metrangolo, R. Milani, T. Pilati, A. Priimagi, G. Resnati, and G. Terraneo. The halogen bond. *Chem. Rev.*, 116(4):2478–2601, 2016.

[168] K. N. Robertson, T. S. Cameron, and O. Knop. Polyhalide anions in crystals. Part 2. I_3 asymmetry and NH… I bonding: triiodides of the $Me_2NH_2^+$, Ph_2I^+, tropanium, N,N,N,N-Me_4-1,2-ethanediammonium, N,N,N,N-Me_4-1,3-propanediammonium, N-Me-piperazinium(2+), and N,N-Me_2-piperazinium(2+) cations, and Me_2NH_2I. *Can. J. Chem.*, 74(8):1572–1591, 1996.

[169] H. Hamaguchi. Polarized resonance Raman spectra of hexahalide complexes of transition metals: The effect of electronic degeneracy on the polarization of vibrational Raman scattering. *J. Chem. Phys.*, 69(2):569–578, 1978.

[170] P. Deplano, F. A. Devillanova, J. R. Ferraro, F. Isaia, V. Lippolis, and M. L. Mercuri. On the use of Raman spectroscopy in the characterization of iodine in charge-transfer complexes. *Appl. Spectrosc.*, 46(11):1625–1629, 1992.

[171] P. H. Svensson and L. Kloo. A vibrational spectroscopic, structural and quantum chemical study of the triiodide ion. *Dalton Trans.*, (14):2449–2455, 2000.

[172] W. Saenger. The structure of the blue starch-iodine complex. *Sci. Nat.*, 71(1):31–36, 1984.

[173] J. J. Colin and H. G. de Claubry. On the reactions of iodine with vegetable and animal materials. *Ann. Chim.*, 90:87–100, 1814.

[174] B. Kahr, J. Freudenthal, S. Phillips, and W. Kaminsky. Herapathite. *Science*, 324(5933):1407, 2009.

[175] E. Redel, C. Röhr, and C. Janiak. An inorganic starch-iodine model: The inorganic-organic hybrid compound $\{(C_4H_12N_2)_2[Cu^I I_4](I_2)\}_n$. *Chem. Commun.*, (16):2103–2105, 2009.

[176] J. Lin, J. Martí-Rujas, P. Metrangolo, T. Pilati, S. Radice, G. Resnati, and G. Terraneo. Solution and solid state synthesis of the discrete polyiodide I_7^{3-} under modular cation templation. *Cryst. Growth Des.*, 12(11):5757–5762, 2012.

[177] A. J. Blake, W.-S. Li, V. Lippolis, M. Schröder, F. A. Devillanova, R. O. Gould, S. Parsons, and C. Radek. Template self-assembly of polyiodide networks. *Chem. Soc. Rev.*, 27(3):195–206, 1998.

[178] Z. Yin, Q.-X. Wang, and M.-H. Zeng. Iodine release and recovery, influence of polyiodide anions on electrical conductivity and nonlinear optical activity in an interdigitated and interpenetrated bipillared-bilayer metalorganic framework. *J. Am. Chem. Soc.*, 134(10):4857–4863, 2012.

[179] L. Kloo, J. Rosdahl, and P. H. Svensson. On the intra- and intermolecular bonding in polyiodides. *Eur. J. Inorg. Chem.*, 2002(5):1203–1209, 2002.

[180] R. C. Teitelbaum, S. L. Ruby, and T. J. Marks. On the structure of starch-iodine. *J. Am. Chem. Soc*, 100(10):3215–3217, 1978.

[181] J. Kommandeur and F. R. Hall. Electronic conduction in complexes of aromatic hydrocarbons with iodine. *J. Chem. Phys*, 34(1):129–133, 1961.

[182] R. C. Teitelbaum, S. L. Ruby, and T. J. Marks. Charge transfer and partial oxidation in the conductive hydrocarbon-iodine complex "2perylene•$3I_2$". *J. Am. Chem. Soc.*, 101(25):7568–7573, 1979.

[183] J. I. G. Cadogan, M. Cameron-Wood, R. K. Mackie, and R. J. G. Searle. 896. The reactivity of organophosphorus compounds. Part XIX. Reduction of nitro-compounds by triethyl phosphite: a convenient new route to carbazoles, indoles, indazoles, triazoles, and related compounds. *J. Chem. Soc.*, pages 4831–4837, 1965.

[184] J. J. Looker. Mononitration of perylene. Preparation and structure proof of the 1 and 3 isomers. *J. Org. Chem.*, 37(21):3379–3381, 1972.

[185] Apex I I SMART. Data collection software, version 2.1. *Bruker AXS Inc.: Madison, WI*, 2005.

[186] A. P. Davis and A. J. Fry. Experimental and computed absolute redox potentials of polycyclic aromatic hydrocarbons are highly linearly correlated over a wide range of structures and potentials. *J. Phys. Chem. A*, 114(46):12299–12304, 2010.

[187] J. M. Reddy, K. Knox, and M. B. Robin. Crystal structure of $HI_3 \cdot 2C_6H_5CONH_2$: a model of the starchiodine complex. *J. Chem. Phys.*, 40(4):1082–1089, 1964.

[188] P. W. Anderson, P. A. Lee, and M. Saitoh. Remarks on giant conductivity in TTF-TCNQ. *Solid State Commun.*, 13(5):595–598, 1973.

[189] F. W. Parrett and N. J. Taylor. Spectroscopic studies on some polyhalide ions. *J. Inorg. Nucl. Chem.*, 32(7):2458–2461, 1970.

[190] U. Behrens, H. J. Breunig, M. Denker, and K. H. Ebert. Iodine chains in $(Me_4Sb)_3I_8$ and discrete triiodide ions in Me_4AsI_3. *Angew. Chem. Int. Ed.*, 33(9):987–989, 1994.

[191] M. Mizuno, J. Tanaka, and I. Harada. Electronic spectra and structures of polyiodide chain complexes. *J. Phys. Chem.*, 85(13):1789–1794, 1981.

[192] F. Demartin, P. Deplano, F. A. Devillanova, F. Isaia, V. Lippolis, and G. Verani. Conductivity, FT-Raman spectra, and X-ray crystal structures of two novel $[D_2I]I_n$ (n = 3 and D = N-methylbenzothiazole-2(3H)-selone; n = 7 and D = N-methylbenzothiazole-2(3H)-thione) iodonium salts. First example of $I-.3I_2$ heptaiodide. *Inorg. Chem.*, 32(17):3694–3699, 1993.

[193] E. M. Nour, L. H. Chen, and J. Laane. Far-infrared and Raman spectroscopic studies of polyiodides. *J. Phys. Chem.*, 90(13):2841–2846, 1986.

[194] R. Poli, J. C. Gordon, R. K. Khanna, and P. E. Fanwick. The first discrete structure for the heptaiodide ion. *Inorg. Chem.*, 31(14):3165–3167, 1992.

[195] A. G. Maki and R. Forneris. Infrared and spectra of some trihalide ions: ICl_2^-, IBr_2^-, I_3^-, I_2Br, and BrICl. *Spectrochimica Acta Part A: Molecular Spectroscopy*, 23(4):867–880, 1967.